

Springer Theses

Recognizing Outstanding Ph.D. Research

René Costard

Ultrafast Dynamics of Phospholipid- Water Interfaces

Studied by Nonlinear
Time-Resolved Vibrational
Spectroscopy

 Springer

Springer Theses

Recognizing Outstanding Ph.D. Research

Aims and Scope

The series “Springer Theses” brings together a selection of the very best Ph.D. theses from around the world and across the physical sciences. Nominated and endorsed by two recognized specialists, each published volume has been selected for its scientific excellence and the high impact of its contents for the pertinent field of research. For greater accessibility to non-specialists, the published versions include an extended introduction, as well as a foreword by the student’s supervisor explaining the special relevance of the work for the field. As a whole, the series will provide a valuable resource both for newcomers to the research fields described, and for other scientists seeking detailed background information on special questions. Finally, it provides an accredited documentation of the valuable contributions made by today’s younger generation of scientists.

Theses are accepted into the series by invited nomination only and must fulfill all of the following criteria

- They must be written in good English.
- The topic should fall within the confines of Chemistry, Physics, Earth Sciences, Engineering and related interdisciplinary fields such as Materials, Nanoscience, Chemical Engineering, Complex Systems and Biophysics.
- The work reported in the thesis must represent a significant scientific advance.
- If the thesis includes previously published material, permission to reproduce this must be gained from the respective copyright holder.
- They must have been examined and passed during the 12 months prior to nomination.
- Each thesis should include a foreword by the supervisor outlining the significance of its content.
- The theses should have a clearly defined structure including an introduction accessible to scientists not expert in that particular field.

More information about this series at <http://www.springer.com/series/8790>

René Costard

Ultrafast Dynamics of Phospholipid-Water Interfaces

Studied by Nonlinear Time-Resolved
Vibrational Spectroscopy

Doctoral Thesis accepted by
Max-Born-Institut, Berlin, Germany

 Springer

Author
Dr. René Costard
Max-Born-Institut
Berlin
Germany

Supervisor
Prof. Thomas Elsässer
Max-Born-Institut
Berlin
Germany

ISSN 2190-5053

Springer Theses

ISBN 978-3-319-22065-9

DOI 10.1007/978-3-319-22066-6

ISSN 2190-5061 (electronic)

ISBN 978-3-319-22066-6 (eBook)

Library of Congress Control Number: 2015944752

Springer Cham Heidelberg New York Dordrecht London

© Springer International Publishing Switzerland 2015

This work is subject to copyright. All rights are reserved by the Publisher, whether the whole or part of the material is concerned, specifically the rights of translation, reprinting, reuse of illustrations, recitation, broadcasting, reproduction on microfilms or in any other physical way, and transmission or information storage and retrieval, electronic adaptation, computer software, or by similar or dissimilar methodology now known or hereafter developed.

The use of general descriptive names, registered names, trademarks, service marks, etc. in this publication does not imply, even in the absence of a specific statement, that such names are exempt from the relevant protective laws and regulations and therefore free for general use.

The publisher, the authors and the editors are safe to assume that the advice and information in this book are believed to be true and accurate at the date of publication. Neither the publisher nor the authors or the editors give a warranty, express or implied, with respect to the material contained herein or for any errors or omissions that may have been made.

Printed on acid-free paper

Springer International Publishing AG Switzerland is part of Springer Science+Business Media
(www.springer.com)

Supervisor's Foreword

Phospholipid molecules, the building blocks of cell membranes, consist of a hydrophilic headgroup and hydrophobic fatty acid chains of hydrocarbons. The ionic headgroup contains a phosphate unit and interacts strongly with water molecules, in particular through phosphate–water hydrogen bonds. The ionic groups generate strong electric fields in the plane of the membrane, leading to a spatial orientation of water molecules. While the structure and basic physical properties of phospholipids in thermal equilibrium are well understood, their dynamics in the time domain of molecular motions and related structural fluctuations represent topics of current research. Key issues are the fluctuating structure of the interfacial water layer, the influence of fluctuating electric fields on molecular dynamics and hydrogen bonding, and processes of energy exchange and dissipation in the hydrated system. The relevant timescales are in the femto- to picosecond range and, thus, methods of ultrafast spectroscopy hold a strong potential for unraveling the basic processes.

In his thesis, Rene Costard studied structural and vibrational dynamics of phospholipids with some of the most advanced methods of femtosecond infrared spectroscopy. His work extended the spectral range of two-dimensional infrared spectroscopy towards fingerprint vibrations of low frequency. As a model system, he investigated reverse micelles of 1,2-dioleoyl-*sn*-glycero-3-phosphocholine (DOPC) which were filled with a water nanopool of variable size and embedded in a nonpolar liquid. Interactions between phospholipids and water were mapped via the ultrafast dynamics of vibrational excitations of either the phosphate groups or water molecules. Vibrational dynamics of the phosphate groups which are addressed here for the first time, are particularly sensitive to interfacial dynamics and, thus, spatially selective. In contrast, water vibrations provide information that is spatially averaged over the water pool.

Rene's work has given detailed new insight at the molecular level. Two-dimensional spectra of phosphate vibrations give evidence of structural disorder of the phospholipid surface, manifested in a distribution of vibrational frequencies. This disorder remains essentially unchanged on a timescale of the order of 10 ps,

both at a very low water level and under conditions of full hydration with up to six water molecules interacting with the phosphate groups. The phosphate–water hydrogen bonds remain intact during this time interval. The hydrated phospholipid structure undergoes limited fluctuations on a 300 fs timescale which originate from statistical motions of both the phospholipid and the interfacial water molecules.

Phospholipid–water interactions play a central role for energy dissipation in the system. The water pool can accommodate large amounts of excess energy stemming from the decay of vibrational and/or electronic excitations of the phospholipid. Redistribution and delocalization of excess energy over water molecules occur on a characteristic timescale of a few picoseconds and establish a heated ground state of the liquid. Rene has shown that a small shell of only three water molecules around a phosphate group is sufficient for implementing this basic and highly efficient mechanism of energy management.

Other key results show that the lifetime of both OH stretching and bending vibrations of water molecules depend on the size of the water pool. The OH stretching vibrations decays via the anharmonically coupled OH bending mode, whereas the OH bending mode relaxes directly into librational water motions. The OH bending lifetime depends sensitively on the energy mismatch with librational overtones.

In conclusion, Rene's thesis combines novel experimental techniques with a sophisticated research strategy to generate new insight into the dynamic properties of phospholipids. The conclusions drawn from the experimental results are supported by detailed theoretical calculations and simulations. This work paves the way for future studies of more complex biomolecular systems in an aqueous environment, the medium of life.

Berlin
February 2015

Prof. Thomas Elsässer

Abstract

Charged phosphate groups are the major hydration sites of biomolecules such as phospholipids and DNA. Hydration shells play a key role in the formation and stabilization of cell membranes and the DNA double helix structure. Here, we introduce phospholipid reverse micelles with variable water content (between one and sixteen water molecules per phospholipid) as a model system to study elementary phosphate–water interactions. The fastest processes at phosphate–water interfaces, e.g. hydrogen-bond dynamics and vibrational energy transfer occur on a femto- to picosecond timescale. Since molecular vibrations are sensitive local probes of the structure and dynamics, the use of femtosecond vibrational spectroscopy, in particular two-dimensional infrared spectroscopy (2D IR) and pump-probe spectroscopy in a broad spectral range, allow for the observation of microscopic phosphate–water interactions in real time. We present the first two-dimensional infrared spectra of phosphate stretching vibrations that represent true interfacial probes independent of the hydration level. Such spectra reveal that the fastest structural fluctuations of phospholipid headgroups occur on a 300-fs timescale, whereas phosphate–water hydrogen bonds are preserved for >10 ps. Vibrational dynamics of intramolecular water vibrations, i.e., the OH stretching and bending modes show that small water pools around the phosphate groups form when three or more water molecules per phospholipid are present. Such water pools act as efficient heat sinks of excess energy deposited in intramolecular vibrations of water or the phosphate groups.

Contents

1	Introduction	1
1.1	Hydration Structure of Phospholipids	3
1.2	Outline	5
	References	6
2	Vibrational Spectroscopy	9
2.1	Molecular Vibrations	9
2.1.1	Vibrational Structure of Polyatomic Molecules	10
2.1.2	Vibrational Lineshapes	13
2.1.3	Vibrational Relaxation	16
2.1.4	Molecular Vibrations as Local Probes in Hydrogen-Bonded Systems	17
2.2	Theoretical Description of Nonlinear Spectroscopy	19
2.2.1	Density Matrix Approach for Calculating Nonlinear Response Functions	20
2.3	Experimental	33
2.3.1	Generation and Characterization of Short Tuneable Mid-Infrared Pulses	33
2.3.2	Passively Phase-Stabilized Heterodyne-Detected Photon Echo	37
2.3.3	Two-Color Pump-Probe Setup	40
2.3.4	Phospholipid Reverse Micelles	42
	References	45
3	Ultrafast Vibrational Dynamics of Phospholipid Hydration Sites	49
3.1	2D IR: Head-Group Fluctuations and Vibrational Couplings	50
3.2	Energy Relaxation: Heat Sink Function of Small Water Pools	58
3.3	Hydration-Insensitivity of Carbonyl Dynamics	64
	References	66

4 Ultrafast Vibrational Dynamics of Phospholipid Hydration Shells	67
4.1 OH Stretching Dynamics: Energy Redistribution into Small Water Pools	69
4.1.1 Vibrational Relaxation to the Bending Mode	74
4.1.2 2D Lineshapes as Probes for Energy Redistribution	77
4.1.3 Small Water Pools as Heat Sinks for Intramolecular Vibrations	79
4.2 OH Bending Dynamics: Energy Relaxation into Intermolecular Modes	81
4.3 Hot Ground States as Local Thermometers, Energy Flow Out of Reverse Micelles	89
References	91
5 Conclusions	95
Appendix A: Experimental Pulse Parameters	99
Curriculum Vitae	101

Chapter 1

Introduction

Cells are the machines of life for all living organisms from the smallest bacteria to large animals or plants [1]. Semipermeable cell membranes separate the cytoplasm from the extracellular space. Their basic structure consists of a bilayer of lipids (cf. Fig. 1.1) complemented by membrane proteins that account for selective transport of ions and molecules in and out of the cell as well as for cell signaling.

The most abundant types of lipids in cell membranes are phospholipids, in particular phosphoglycerides that consist of a glycerol backbone linked to two fatty acids and a phosphate group by ester bonds (Fig. 1.2). The phosphate group is esterified with an alcohol that determines the nature of the head groups, the main types in mammalian membranes being phosphatidylcholines, phosphatidylethanolamines and phosphatidylserines (cf. Fig. 1.2c–e). All types of head groups are zwitterionic making them polar so that they can form hydrogen bonds with water [3, 4]. In contrast, the hydrocarbon chains of fatty acids are nonpolar. Thus, their composition defines the structure of a phospholipid's hydrophobic tails. Often, one of the chains is saturated and the other one has an unsaturated C-C bond causing a kink in that chain. One example is the mixed-chain phospholipid 1-palmitoyl-2-oleoyl-sn-glycero-3-phosphocholine (POPC) in Fig. 1.2c.

The amphiphilic character of phospholipids is of major importance for the spontaneous self-assembly into lipid bilayers in aqueous solutions. Hydrophobic effects cause the lipids to align in a way that the hydrocarbon chains form the interior of the bilayer that exposes the hydrophilic head groups to the aqueous environment. Water in the vicinity of such interfaces experiences an environment significantly different from the tetrahedral configuration in the bulk phase [5, 6]. Water molecules are aligned in the electrostatic potential of the lipid head groups and form hydrogen bonds with the phosphate and carbonyl groups. Due to this confinement, the motional freedom of water at lipid interfaces is reduced (the hydration structure of phospholipids is briefly reviewed in Sect. 1.1).

Water is not only essential for the formation of cell membranes but also determines the structure and function of other biomolecules such as proteins and DNA and is therefore a crucial component in cell biology [7, 8]. For example, it has been suggested that the interaction of water and proteins plays an important role in

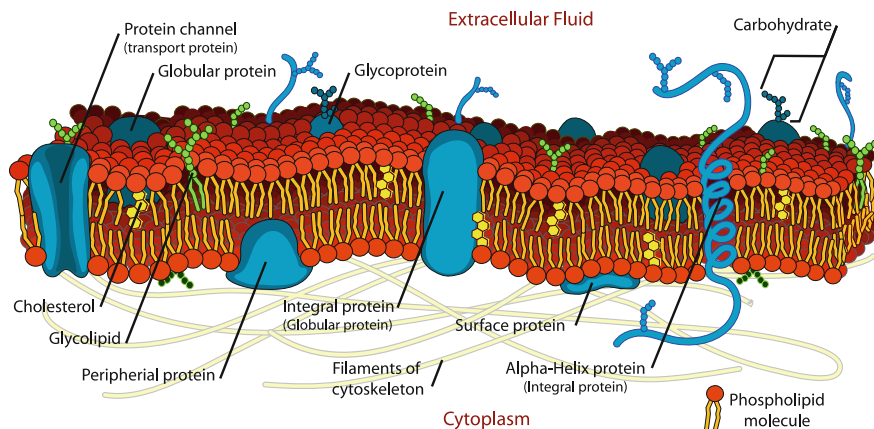


Fig. 1.1 Schematic of a lipid bilayer cell membrane. Modified from [2]

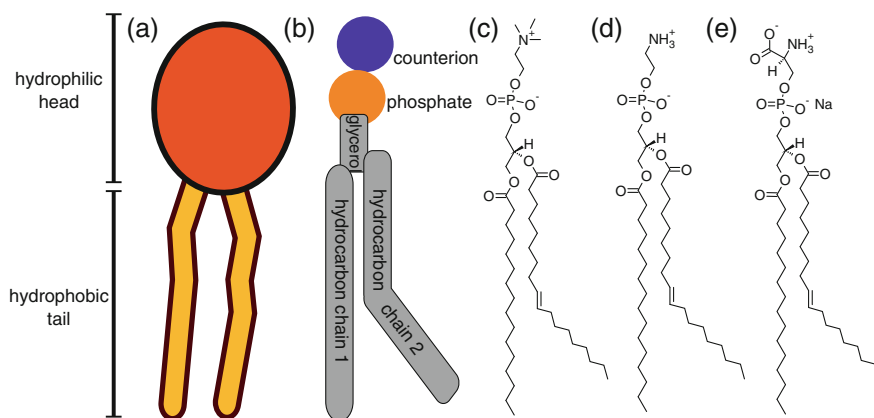


Fig. 1.2 Structure of a phosphoglyceride molecule. **a** Cartoon representing the hydrophilic head and hydrophobic tails as in Fig. 1.1. **b** Schematic of phosphoglyceride indicating its constituents. **c–e** Molecular structure of three phospholipids with different head groups as representatives for phosphatidylcholines, phosphatidylethanolamines and phosphatidylserines

protein folding and binding [9, 10]. X-ray diffraction studies have shown that the DNA double-helix conformation changes from the biologically important B-form to the A-form upon dehydration [11]. As for phospholipids, phosphate groups are major hydration sites of DNA [12, 13]. The characteristics of phosphate-water interactions therefore determine the properties of the hydration shells of a diverse class of biomolecules.

In this context it is of great relevance to obtain information about the distance from the interface up to which water properties differ from the bulk phase, i.e., to define a thickness of the hydration shell. In an extreme case, water is confined in small spherical phospholipid self-assemblies called vesicles. Organized molecular

transport in the cell with the help of such particles has attracted substantial research effort culminating in the award of the *2013 Nobel Prize in Physiology or Medicine* [14]. The concept of hydration shells may even break down in vesicles calling for future investigations of the behavior of confined water.

Important biological processes like the function of proteins in proton and ion transport, or most generally the outcome of chemical reactions in the vicinity of polar interfaces depend in a decisive way on the structure and dynamics of the interface and its hydration shell. Molecular vibrations of functional groups being hydrated as well as those of the hydrating water are sensitive local probes for electrostatic interactions and hydrogen bonding. Additionally, molecular vibrations serve as acceptors of excess energy, e.g., created by the absorption of a UV photon or an exothermic reaction, thereby accounting for the thermalization of heated biomolecular systems. Bond making and breaking, structural fluctuations, and vibrational energy redistribution in the condensed phase, in particular in hydrogen bonded systems, occur on a femto- to picosecond time scale [15–24]. Therefore, time-resolved vibrational spectroscopy is a powerful tool to capture the dynamics at water-phosphate interfaces connected to the fastest molecular processes in real time.

This thesis represents the first comprehensive investigation of such processes occurring in both the head groups and the hydration shell of phospholipid reverse micelles which are spherical phospholipid aggregates that separate nanoscopic water pools from a nonpolar environment. In order to interpret the results that will be presented later, we shall briefly review the microscopic structure of phospholipid hydration. Details about the reverse-micelle system are presented in Sect. 2.3.4.

1.1 Hydration Structure of Phospholipids

The structure of phospholipids and their hydration shell have been studied extensively by a wide variety of experimental methods, among them x-ray [25–30] and neutron diffraction [31–35], nuclear magnetic resonance (NMR) [33, 34, 36, 37], and infrared spectroscopy [38, 39].

Early diffraction measurements on single crystalline phospholipids find head-group orientations almost parallel to the bilayer surface with an 70° angle between the phosphate-nitrogen (P-N) vector and the bilayer normal [26]. Salt bridges with lengths of approximately 0.27 nm connecting the phosphorus and nitrogen of neighboring phosphatidylethenamines are formed. For phosphatidylcholines similar inter- and intramolecular P-N distances of ≈ 0.45 nm point to strong electrostatic interactions between neighboring head groups. The two first water molecules of hydration link phosphate and choline groups and organize the phosphate groups into ribbons. If more water is added, a preferential interaction with other water molecules rather than with the lipid head groups is found. The hydrocarbon chain angle with respect to the bilayer depends on the chain structure and is adjusted to establish close packing. Since the two hydrocarbon chains are attached to different positions in the glycerol backbone, both chains are axially displaced by 3 methylene (CH_2) units.

The biologically relevant lipid-bilayer membranes are characterized by a higher degree of disorder and fluidity so that they can be viewed as a two-dimensional fluid [40]. That is, phospholipids are free to diffuse in the plane of the bilayer with a diffusion constant in the range of 10^{-7} – 10^{-8} $\text{cm}^2/\text{s}^{-1}$ [41–43] whereas phospholipid flip-flops, i.e., hopping between the two leaflets of the bilayer, are much more unlikely and happen on a time scale of minutes to hours [44].

The measured average angle of the P-N vector with the bilayer normal is in the range between 50° and 70° [27, 31, 37], while the hydrocarbon chains are disordered [32, 45]. Addition of water leads to an increase of the area per lipid from ≈ 0.6 to 0.7 nm^2 when the ratio of water to lipid molecules is changed from 5 to 11 [28, 30]. Charge pairs with intermolecular interactions of phosphate and choline groups of neighboring phospholipids were found in vesicles [36]. Water penetrates lipid membranes up to the ester carbonyl groups and forms hydrogen bonds with the phosphate and carbonyl groups [38, 46].

Hydration structures of non-aggregated phospholipids are well characterized [35]. Phosphate and carbonyl groups act as acceptors for strong hydrogen bonds with water whereas no hydrogen bonds with water are formed by the choline group. The strong head-group dipole leads to an orientation of water molecules with the hydrogens pointing away from the choline and therefore maximizing their interaction with surrounding water. On the other hand, the water hydrogens point toward the phosphate oxygens which allows them to form phosphate-water hydrogen bonds. About 2.5 hydrogen bonds are formed at each phosphate and carbonyl oxygen; the number of hydrogen bonds for the latter decreases to about 1 when carbonyls are located close to the hydrophobic part of a membrane.

Time-resolved measurements of phospholipid self-assemblies on the picosecond time scale of hydrogen bond dynamics in water are rare. Indirect NMR measurements of lipid-water interactions give rotational correlation times of water on the order of 50 ps [33] as well as correlation times of water-lipid and lipid-lipid interactions on the order of 100 ps and a few nanoseconds, respectively [34].

These experimental findings are complemented by molecular dynamics (MD) simulations to gain additional microscopic insight into lipid-water interactions [47–55]. The calculations confirm basic structural features of bilayers like the P-N angle tilt and the head-group area. Additionally, a detailed picture the hydration structure is obtained, where phosphates form 4–6 hydrogen bonds and the carbonyls form one hydrogen bond with water [48, 50, 53]. Those hydrogen bonds are stronger than the ones between two water molecules. Hydrogen bonding to the nitrogen of phosphatidylcholines is prevented by the shielding methyl groups, resulting in a clathrate-like water structure around the choline group. Simulations provide insight into electric potentials created by the polar head groups. Water molecules are arranged in a way that their dipoles oppose the lipid potential and make a significant contribution to the overall membrane potential [52, 54]. Substantial intra- and intermolecular head-group interactions lead to so-called charge pairs connecting phosphate and carbonyl groups with the choline group directly or with the help of water bridges [50]. Detailed time-resolved trajectories provide information about water and head-group dynamics. Typically, residence times of water at specific hydrations sites of the phos-

pholipid as well as hydrogen bond correlation and orientational relaxation times are extracted [48, 52, 55]. A multiexponential behavior is found with the fastest components of about 1 ps and slower components extending to tens and hundreds of picoseconds. Water bridges and charge pairs live approximately 100 ps with temporary break times on the order of a few picoseconds [51].

The amphiphilicity of phospholipid molecules allows them to self-assemble into a range of different structures [56]. In aqueous solutions they form bilayers, vesicles and micelles where the hydrophilic head groups interact with water and neighboring head groups in the way outlined above. In contrast, the hydrophobic tail groups of different phospholipids interact preferentially with themselves thereby causing the process of self-assembly [57]. A contrary effect occurs for lipids dissolved in nonpolar solvents favoring an interaction with the hydrocarbon chains. Depending on the solvent used and the structure and concentration of the lipid, reverse micelles, i.e., spherical or spheroidal aggregates with the hydrophilic heads pointing to the interior, can form (cf. Fig. 2.14, p. 43) [58]. The addition of water to this system leads to a formation of water pools inside the reverse micelles so that phosphate-water interactions can be studied under well-defined conditions.

It was suggested that phospholipid reverse micelles transiently exist in membrane bilayers, e.g., during the joining of two bilayers [59, 60]. Their internal structure is similar to vesicles leading to the anticipation that the properties of water in the two different aggregates are comparable. As such, reverse micelles represent important model systems for the chemistry and physics of cell membranes and vesicles. Furthermore, reverse micelles made of other surfactants such as dioctyl sodium sulfosuccinate (AOT, cf. Fig. 2.14) have grown into a major tool for synthesis in material science and biotechnology [61, 62]. Guest molecules like proteins, nucleic acids and enzymes may be incorporated into the water pool of reverse micelles so that parameters of chemical reactions such as hydration and spatial confinement can be varied. Additionally, the different polarity of the solvent and intramicellar medium (water or other polar solvents) allows for chemical reactions of reactants of different solubility. A detailed description of the preparation and structure of the reverse micelles that were used as a phospholipid model system for this thesis is given in Sect. 2.3.4.

1.2 Outline

The thesis is structured as follows. The first part of Chap. 2 introduces a theoretical description of molecular vibrations and time-integrated as well as time-resolved vibrational spectroscopy. Experimental techniques are introduced in the second part of Chap. 2. Chapter 3 covers the dynamics of phosphate and carbonyl vibrations and investigates the influence of phospholipid head-group hydration on structural dynamics and energy relaxation. In a similar way, structural dynamics and the energy relaxation pathway of intramolecular water vibrations of the phospholipid hydration shell are examined as a function of the hydration-shell size in Chap. 4. A summary and conclusions are presented in Chap. 5.

References

1. B. Alberts, A. Johnson, J. Lewis, M. Raff, K. Roberts, P. Walter, *Molecular Biology of the Cell*, 5th edn. (Garland Science, Taylor and Francis Group, Boca Raton, 2008)
2. http://commons.wikimedia.org/wiki/File:Cell_membrane_detailed_diagram_en.svg. August (2013)
3. L. Pauling, *The Nature of the Chemical Bond and the Structure of Molecules and Crystals*, 3rd edn. (Cornell University Press, New York, 1960)
4. G.C. Pimentel, A.L. McClellan, *The Hydrogen Bond* (W. H. Freeman & Company, San Francisco, 1960)
5. J. Milhaud, New insights into water-phospholipid model membrane interactions. *Biochim. Biophys. Acta Biomembr.* **1663**, 19–51 (2004)
6. M.L. Berkowitz, D.L. Bostick, S. Pandit, Aqueous solutions next to phospholipid membrane surfaces: insights from simulations. *Chem. Rev.* **106**, 1527–1539 (2006)
7. M. Chaplin, Do we underestimate the importance of water in cell biology? *Nat. Rev. Mol. Cell Biol.* **7**, 861–866 (2006)
8. P. Ball, Water as an active constituent in cell biology. *Chem. Rev.* **108**, 74–108 (2008)
9. A. Nicholls, K.A. Sharp, B. Honig, Protein folding and association: insights from the interfacial and thermodynamic properties of hydrocarbons. *Proteins: Struct. Funct. Bioinform.* **11**, 281–296 (1991)
10. M.S. Cheung, A.E. Garcia, J.N. Onuchic, Protein folding mediated by solvation: water expulsion and formation of the hydrophobic core occur after the structural collapse. *Proc. Natl. Acad. Sci. USA* **99**, 685–690 (2002)
11. W. Saenger, W.N. Hunter, O. Kennard, DNA conformation is determined by economics in the hydration of phosphate groups. *Nature* **324**, 385–388 (1986)
12. M. Falk, K.A. Hartman, R.C. Lord, Hydration of deoxyribonucleic acid. I. A gravimetric study. *J. Am. Chem. Soc.* **84**, 3843–3846 (1962)
13. M. Falk, K.A. Hartman, R.C. Lord, Hydration of deoxyribonucleic acid. II. An infrared study. *J. Am. Chem. Soc.* **85**, 387–391 (1963)
14. The 2013 Nobel Prize in Physiology or Medicine—Press Release, Nobelprize.org. Nobel Media AB (2013). http://www.nobelprize.org/nobel_prizes/medicine/laureates/2013/press.html
15. A.H. Zewail. *Femtochemistry: Atomic-scale Dynamics of the Chemical Bond Using Ultrafast Lasers*. Nobel Lecture (1999)
16. T. Elsaesser, H.J. Bakker (eds.), *Ultrafast Hydrogen Bonding Dynamics and Proton Transfer Processes in the Condensed Phase* (Springer, New York, 2002)
17. M.D. Fayer (ed.), *Ultrafast Infrared Vibrational Spectroscopy* (Routledge Chapman & Hall, New York, 2013)
18. A. Laubereau, W. Kaiser, Picosecond spectroscopy of molecular dynamics in liquids. *Annu. Rev. Phys. Chem.* **26**, 83–99 (1975)
19. T. Elsaesser, W. Kaiser, Vibrational and vibronic relaxation of large polyatomic molecules in liquids. *Annu. Rev. Phys. Chem.* **42**, 83–107 (1991)
20. J.C. Owrtzsky, D. Raftery, R.M. Hochstrasser, Vibrational relaxation dynamics in solutions. *Annu. Rev. Phys. Chem.* **45**, 519–555 (1994)
21. E.T.J. Nibbering, T. Elsaesser, Ultrafast vibrational dynamics of hydrogen bonds in the condensed phase. *Chem. Rev.* **104**, 1887–1914 (2004)
22. H.J. Bakker, J.L. Skinner, Vibrational spectroscopy as a probe of structure and dynamics in liquid water. *Chem. Rev.* **110**, 1498–1517 (2010)
23. M.D. Fayer, N.E. Levinger, Analysis of water in confined geometries and at interfaces. *Annu. Rev. Anal. Chem.* **3**, 89–107 (2010)
24. A. Ghosh, R.M. Hochstrasser, A peptide’s perspective of water dynamics. *Chem. Phys.* **390**, 1–13 (2011)
25. M. Sundaralingam, Discussion paper: Molecular structures and conformations of the phospholipids and sphingomyelins. *Ann. N. Y. Acad. Sci.* **195**, 324–355 (1972)

26. H. Hauser, I. Pascher, R.H. Pearson, S. Sundell, Preferred conformation and molecular packing of phosphatidylethanolamine and phosphatidylcholine. *Biochim. Biophys. Acta Rev. Biomembr.* **650**, 21–51 (1981)
27. R.H. Pearson, I. Pascher, The molecular structure of lecithin dihydrate. *Nature* **281**, 499–501 (1979)
28. M.C. Wiener, S.H. White, Structure of a fluid dioleoylphosphatidylcholine bilayer determined by joint refinement of x-ray and neutron diffraction data. III. Complete structure. *Biophys. J.* **61**, 434–447 (1992)
29. K. Gawrisch, D. Ruston, J. Zimmerberg, V.A. Parsegian, R.P. Rand, N. Fuller, Membrane dipole potentials, hydration forces, and the ordering of water at membrane surfaces. *Biophys. J.* **61**, 1213–1223 (1992)
30. S. Tristram-Nagle, H.I. Petrache, J.F. Nagle, Structure and interactions of fully hydrated dioleoylphosphatidylcholine bilayers. *Biophys. J.* **75**, 917–925 (1998)
31. D.L. Worcester, N.P. Franks, Structural analysis of hydrated egg lecithin and cholesterol bilayers II. Neutron diffraction. *J. Mol. Biol.* **100**, 359–378 (1976)
32. G. Büldt, H.U. Gally, A. Seelig, J. Seelig, Neutron-diffraction studies on selectively deuterated phospholipid bilayers. *Nature* **271**, 182–184 (1978)
33. S. König, E. Sackmann, D. Richter, R. Zorn, C. Carlile, T.M. Bayerl, Molecular dynamics of water in oriented DPPC multilayers studied by quasielastic neutron scattering and deuterium-nuclear magnetic resonance relaxation. *J. Chem. Phys.* **100**, 3307–3316 (1994)
34. K. Gawrisch, H.C. Gaede, M. Mihailescu, S.H. White, Hydration of POPC bilayers studied by ¹H-PFG-MAS-NOESY and neutron diffraction. *Eur. Biophys. J.* **36**, 281–291 (2007)
35. F. Foglia, M.J. Lawrence, C.D. Lorenz, S.E. McLain, On the hydration of the phosphocholine headgroup in aqueous solution. *J. Chem. Phys.* **133**, 145103 (2010)
36. P.L. Yeagle, W.C. Hutton, C.-H. Huang, R.B. Martin, Phospholipid headgroup conformations; intermolecular interactions and cholesterol effects. *Biochemistry* **16**, 4344–4349 (1977)
37. J. Seelig, ³¹P nuclear magnetic resonance and the head group structure of phospholipids in membranes. *Biochim. Biophys. Acta Rev. Biomembr.* **515**, 105–140 (1978)
38. P.T.T. Wong, H.H. Mantsch, High-pressure infrared spectroscopic evidence of water binding sites in 1,2-diacyl phospholipids. *Chem. Phys. Lipids* **46**, 213–224 (1988)
39. X. Chen, W. Hua, Z. Huang, H.C. Allen, Interfacial water structure associated with phospholipid membranes studied by phase-sensitive vibrational sum frequency generation spectroscopy. *J. Am. Chem. Soc.* **132**, 11336–11342 (2010)
40. S.J. Singer, G.L. Nicolson, The fluid mosaic model of the structure of cell membranes. *Science* **175**, 720–731 (1972)
41. A.-L. Kuo, C.G. Wade, Lipid lateral diffusion by pulsed nuclear magnetic resonance. *Biochemistry* **18**, 2300–2308 (1979)
42. W.L.C. Vaz, R.M. Clegg, D. Hallmann, Translational diffusion of lipids in liquid crystalline phase phosphatidylcholine multibilayers. A comparison of experiment with theory. *Biochemistry* **24**, 781–786 (1985)
43. W. Pfeiffer, T. Henkel, E. Sackmann, W. Knoll, D. Richter, Local dynamics of lipid bilayers studied by incoherent quasi-elastic neutron scattering. *Europhys. Lett.* **8**, 201–206 (1989)
44. M. Seigneuret, P.F. Devaux, ATP-dependent asymmetric distribution of spinlabeled phospholipids in the erythrocyte membrane: relation to shape changes. *Proc. Natl. Acad. Sci. USA* **81**, 3751–3755 (1984)
45. A. Seelig, J. Seelig, Dynamic structure of fatty acyl chains in a phospholipid bilayer measured by deuterium magnetic resonance. *Biochemistry* **13**, 4839–4845 (1974)
46. F. Borle, J. Seelig, Hydration of *Escherichia coli* lipids: Deuterium T1 relaxation time studies of phosphatidylglycerol, phosphatidylethanolamine and phosphatidylcholine. *Biochim. Biophys. Acta Biomembr.* **735**, 131–136 (1983)
47. R.M. Venable, Y. Zhang, B.J. Hardy, R.W. Pastor, Molecular dynamics simulations of a lipid bilayer and of hexadecane: an investigation of membrane fluidity. *Science* **262**, 223–226 (1993)
48. H.E. Alper, D. Bassolino-Klimas, T.R. Stouch, The limiting behavior of water hydrating a phospholipid monolayer: a computer simulation study. *J. Chem. Phys.* **99**, 5547–5559 (1993)

49. K. Tu, D.J. Tobias, M.L. Klein, Constant pressure and temperature molecular dynamics simulation of a fully hydrated liquid crystal phase dipalmitoylphosphatidylcholine bilayer. *Biophys. J.* **69**, 2558–2562 (1995)
50. M. Pasenkiewicz-Gierula, Y. Takaoka, H. Miyagawa, K. Kitamura, A. Kusumi, Hydrogen bonding of water to phosphatidylcholine in the membrane as studied by a molecular dynamics simulation: Location, geometry, and lipid-lipid bridging via hydrogen-bonded water. *J. Phys. Chem. A* **101**, 3677–3691 (1997)
51. M. Pasenkiewicz-Gierula, Y. Takaoka, H. Miyagawa, K. Kitamura, A. Kusumi, Charge pairing of headgroups in phosphatidylcholine membranes: a molecular dynamics simulation study. *Biophys. J.* **76**, 1228–1240 (1999)
52. W. Shinoda, M. Shimizu, S. Okazaki, Molecular dynamics study on electrostatic properties of a lipid bilayer: polarization, electrostatic potential, and the effects on structure and dynamics of water near the interface. *J. Phys. Chem. B* **102**, 6647–6654 (1998)
53. L. Saiz, M.L. Klein, Structural properties of a highly polyunsaturated lipid bilayer from molecular dynamics simulations. *Biophys. J.* **81**, 204–216 (2001)
54. L. Saiz, M.L. Klein, Electrostatic interactions in a neutral model phospholipid bilayer by molecular dynamics simulations. *J. Chem. Phys.* **116**, 3052–3057 (2002)
55. S.Y. Bhide, M.L. Berkowitz, Structure and dynamics of water at the interface with phospholipid bilayers. *J. Chem. Phys.* **123**, 224702 (2005)
56. W.M. Gelbart, A. Ben-Shaul, D. Roux (eds.), *Micelles, Membranes, Microemulsions, and Monolayers* (Springer, New York, 1994)
57. J.C. Shelley, M.Y. Shelley, R.C. Reeder, S. Bandyopadhyay, M.L. Klein, A coarse grain model for phospholipid simulations. *J. Phys. Chem. B* **105**, 4464–4470 (2001)
58. P. Walde, A.M. Giuliani, C.A. Boicelli, P.L. Luisi, Phospholipid-based reverse micelles. *Chem. Phys. Lipids* **53**, 265–288 (1990)
59. P.R. Cullis, M.J. Hope, C.P.S. Tilcock, Lipid polymorphism and the roles of lipids in membranes. *Chem. Phys. Lipids* **40**, 127–144 (1986)
60. B. de Kruijff, P.R. Cullis, A.J. Verkleij, Non-bilayer lipid structures in model and biological membranes. *Trends Biochem. Sci.* **5**, 79–81 (1980)
61. P.L. Luisi, M. Giomini, M.P. Pileni, B.H. Robinson, Reverse micelles as hosts for proteins and small molecules. *Biochim. Biophys. Acta Rev. Biomembr.* **947**, 209–246 (1988)
62. M.P. Pileni, Reverse micelles as microreactors. *J. Phys. Chem.* **97**, 6961–6973 (1993)

Chapter 2

Vibrational Spectroscopy

2.1 Molecular Vibrations

A description of a quantum-mechanical system requires the knowledge of its Hamiltonian H . The solution of the time-independent Schrödinger equation gives the eigenstates and energies of a molecule whereas the time evolution, e.g., arising from interactions with a fluctuating solvent or a light field, is determined by the time-dependent Schrödinger equation. Consider as a starting point the following Hamiltonian of a molecule:

$$H = -\frac{\hbar^2}{2m_e} \sum_i \nabla_e^2 - \sum_i \frac{\hbar^2}{2m_{n,i}} \nabla_n^2 + V_{ee} + V_{nn} + V_{ne} \quad (2.1)$$

The first two terms on the right-hand side represent the kinetic energies with the sum running over all electrons and nuclei with the masses m_e and $m_{n,i}$, respectively. The Laplace operators $\nabla_{e,n}^2$ act either on the electronic (e) or nuclear (n) coordinates. V_{ee} and V_{nn} are due to the electrons' and nuclei's Coulomb repulsion whereas the term V_{ne} describes the Coulomb attraction between electrons and nuclei. We only include terms for an isolated molecule. In the liquid phase, additional terms due to solute-solvent interactions contribute to the Hamiltonian.

In the Born-Oppenheimer approximation [1], a separation between the electronic and nuclear wavefunctions due to their distinctly different masses and time scales of motion leads to a situation where the electronic states define potential energy surfaces for the nuclei. Figure 2.1 schematically shows the vibrational potential $V(q)$ as a function of the vibrational coordinate q , e.g., the distance of two atoms in a molecule. Around the equilibrium distance q_0 , the potential might be approximated as harmonic. However, large nuclear separations will eventually lead to bond dissociation and at short separations the repulsion terms in Eq. 2.1 dominate, effectively causing the potential to be anharmonic. Intra- and intermolecular vibrational couplings are additional sources for anharmonicities of polyatomic molecules in the condensed phase. As a consequence, the energy levels are not equally spaced and the diagonal anharmonicity $\Delta = E_{01} - E_{12}$ is a sensitive probe for the local structure and interactions of a molecule. Here, $E_{01} = E_1 - E_0$ and $E_{12} = E_2 - E_1$ represent

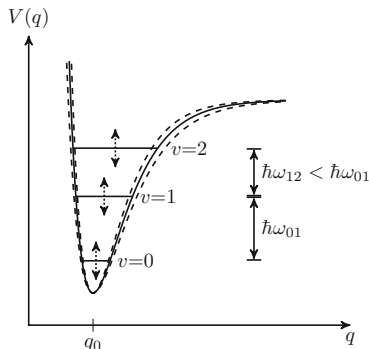


Fig. 2.1 Anharmonic oscillator potential. The anharmonicity causes the transition frequency ω_{01} for the $v = 0$ to 1 transition to be bigger than the one for the $v = 1$ to 2 transition (ω_{12}). Fluctuating forces exerted by the bath cause a time-dependent potential (*dashed lines*) resulting in fluctuating transition frequencies

the energy differences for transitions from the ground to the first excited state ($v = 0$ to 1) and from the first to the second excited state ($v = 1$ to 2), respectively. Instead of energies, this thesis we will often use transition frequencies $\omega_{01,12} = E_{01,12}/\hbar$ that are commonly measured in wavenumbers $\nu = \omega/(2\pi c)$ (with c being the speed of light) in infrared spectroscopy.

Infrared spectra are closely related to the vibrational potential $V(q)$. Numerous textbooks cover a large variety of aspects related to the structure and interaction of complex molecules and their connection to vibrational absorption spectra. A few of them will be reviewed in the next section that is mainly based on [2–4].

2.1.1 Vibrational Structure of Polyatomic Molecules

A molecule consisting of N atoms has $3N$ degrees of freedom, 6 of which describe the translation of the center of mass and the molecular rotation; i.e., there are $3N - 6$ vibrational degrees of freedom described by the coordinates $\vec{q} = (q_1, \dots, q_m)$ with $m = 3N - 6$. If the nuclear displacements from their equilibrium positions are small, the vibrational potential $V(\vec{q})$ can be approximated with a Taylor expansion:

$$V(\vec{q}) = V(\vec{q}_0) + \sum_{i=1}^m \left. \frac{\partial V}{\partial q_i} \right|_{\vec{q}_0} q_i + \frac{1}{2} \sum_{i,j=1}^m \left. \frac{\partial^2 V}{\partial q_i \partial q_j} \right|_{\vec{q}_0} q_i q_j + \frac{1}{6} \sum_{i,j,k=1}^m \left. \frac{\partial^3 V}{\partial q_i \partial q_j \partial q_k} \right|_{\vec{q}_0} q_i q_j q_k + \dots \quad (2.2)$$

$$\approx \frac{1}{2} \sum_{i,j=1}^m V_{ij}(\vec{q}_0) q_i q_j + \dots \quad (2.3)$$

$V(\vec{q}_0)$ is the (constant) potential at the equilibrium position that can be defined as zero. $\partial V/\partial q_i|_{\vec{q}_0}$ is the force acting on the i th coordinate that vanishes at the equilibrium position so that the quadratic term is the leading one in the Taylor expansion. By neglecting higher-order terms in Eq. 2.3, the harmonic approximation is applied. A diagonalization of the quadratic Hamiltonian is achieved by a coordinate transformation to normal modes [5]. As a result, the well-known energy structure of quantum-mechanical harmonic oscillators [6] is obtained

$$E(v_1, \dots, v_m) = \sum_{i=1}^m \hbar\omega_i \left(v_i + \frac{1}{2} \right) \quad (2.4)$$

with the frequency ω_i and vibrational quantum number v_i of the i th normal mode. The corresponding wavefunction is a product of wavefunctions of m independent oscillators.

As pointed out before, realistic vibrational potentials of molecules in solution are anharmonic, i.e., higher-order terms in Eq. 2.3 cannot be neglected. Consequently, the vibrational energies are not simple sums of individual oscillators but may be approximated

$$E(v_1, \dots, v_m) \approx \sum_{i=1}^m \hbar\omega_i \left(v_i + \frac{1}{2} \right) + \sum_{i=1}^m \sum_{k \geq i}^m x_{ik} \left(v_i + \frac{1}{2} \right) \left(v_k + \frac{1}{2} \right) + \dots \quad (2.5)$$

where the factors x_{ik} represent the anharmonicity constants. Similarly, the total vibrational wavefunction depends on the anharmonicities and is no longer a product of single harmonic oscillator wavefunctions.

Note that the vibrational energy levels are not equidistant when anharmonicities are included. If the off-diagonal anharmonicities x_{ik} with $i \neq k$ vanish, we find for the transition energy difference of the i th mode $\Delta_i = E_{01i} - E_{12i} = -2x_{ii}$. The diagonal anharmonicities x_{ii} are typically negative leading to a red-shifted excited state absorption (cf. Fig. 2.7). Likewise, non-vanishing off-diagonal anharmonicities lead to changes of the transition frequency of oscillator i according to the value of x_{ik} and the population of oscillator k . While diagonal anharmonicities of vibrations are of major importance in time-resolved vibrational spectroscopy when an excited state population exists, the subsequent relaxation and population of low-frequency bath modes often cause long-lived heating signals due to the off-diagonal anharmonicities.

An important consequence following from the introduction of mixed terms $q_i q_j$ with $i \neq j$ in Eq. 2.3 is that originally degenerate levels will split in energy. Consider two eigenstates $|\varphi_{1,2}\rangle$ with energies $E_1^0 \approx E_2^0$ of the uncoupled Hamiltonian H_0 that is purely quadratic in the coordinate q_i . The degeneracy is lifted by searching for new eigenstates $|\tilde{\varphi}_{\pm}\rangle$ of the Hamiltonian $H = H_0 + H'$ including coupling terms H' . The corresponding new energies E_{\pm} follow from the secular determinant:

$$\begin{vmatrix} E_1^0 - E_{\pm} & H'_{12} \\ H'_{21} & E_2^0 - E_{\pm} \end{vmatrix} = 0 \quad (2.6)$$

Here H'_{12} and $H'_{21} = H'_{12}^*$ are the matrix elements of the coupling Hamiltonian between the old $|\varphi_{1,2}\rangle$ -states. The solution to Eq. 2.6 is

$$E_{\pm} = \bar{E}^0 \pm \frac{1}{2} \sqrt{4 |H'_{12}|^2 + \delta^2} \quad (2.7)$$

with $\bar{E}^0 = (E_1^0 + E_2^0)/2$ and $\delta = E_2^0 - E_1^0$ being the average and difference of E_1^0 and E_2^0 , respectively. In the weak-coupling limit ($|H'_{12}| \ll \delta$), the eigenstates and energies are only slightly altered so that energy difference $E_+ - E_- \approx \delta$. Obviously, splitting of (nearly) degenerate levels occurs in the strong-coupling limit ($|H'_{12}| \gg \delta$). Hence, the degeneracy is removed ($E_+ - E_- \approx 2|H'_{12}|$) and the new eigenstates are superpositions of $|\varphi_{1,2}\rangle$ whose degree of mixing increases with the coupling matrix element $|H'_{12}|^2$.

Consider, e.g., the two local OH stretching modes of a water molecule resulting from independent oscillations of the two hydrogens. For two oscillators without coupling these vibrations would be degenerate. That is, the two eigenstates $|\varphi_1\rangle = |10\rangle$ and $|\varphi_2\rangle = |01\rangle$ have the same eigenfrequency. Using the annihilation and creation operators $a_{1,2}$ and $a_{1,2}^\dagger$ acting only on the corresponding wavefunction it follows that $q_1 q_2 \propto (a_1 + a_1^\dagger)(a_2 + a_2^\dagger)$. Only the term $a_1^\dagger a_2$ survives in calculating $H'_{12} = \langle \varphi_1 | q_1 q_2 | \varphi_2 \rangle$ demonstrating that the mixed terms in Eq. 2.3 indeed lead to a splitting of energy levels. For the water molecule the new eigenstates are the normal symmetric and antisymmetric stretching modes with the wavefunctions $|\varphi_{S,AS}\rangle = 1/\sqrt{2} (|01\rangle \pm |10\rangle)$ (cf. Sect. 2.1.4).

Degeneracies also occur when a combination or overtone of a vibration has a similar frequency as another high-frequency vibration. This phenomenon of a so-called accidental degeneracy was first observed by Fermi for vibrations of CO_2 molecules [7]. It is therefore often referred to as *Fermi resonance*. In bulk water, the OH bending overtone ($v = 2$) is close in energy to the broad stretching band. The corresponding coupling matrix element is $\langle 20 | H' | 01 \rangle$. Apparently, at least third-order terms of the potential have to be considered, e.g., $q_1^2 q_2$ produces (amongst others) the combination $a_1^{\dagger 2} a_2$ that results in a non-vanishing matrix element. Generally, Fermi resonances and the accompanying level mixing lead to enhancements of the oscillator strength of overtones which also serve as energy acceptors for vibrational excitations of the high-frequency mode. It will be shown in this work that the bending mode plays an important role for OH stretching excitations of phospholipid hydration shells.

There are different methods to access vibrational frequencies of molecules in the electronic ground state, e.g., infrared absorption, Raman scattering [8] and inelastic neutron scattering [9]. In this thesis we will focus on the first technique which is based on the interaction of molecular dipoles with an infrared electric light field. According to Fermi's Golden rule, the probability of a transition from an initial state $|\varphi_i\rangle$ to a final state $|\varphi_f\rangle$ caused by the dipole interaction is determined by the dipole

matrix element $|\mu_{if}|^2 = |\langle \varphi_i | \mu | \varphi_f \rangle|^2$. A Taylor expansion of the dipole moment μ with respect to the coordinate of a molecular vibration q around the equilibrium position q_0

$$\mu(q) = \mu(q_0) + \left. \frac{\partial \mu}{\partial q} \right|_{q_0} q + \dots \quad (2.8)$$

shows that transitions between orthogonal states only occur if there is a change of the dipole $\partial \mu / \partial q|_{q_0}$ since $\mu(q_0)$ is a constant that represents the equilibrium dipole moment.

Dipole-allowed transitions give rise to infrared absorption lines [10]

$$A(\omega) \propto \int_{-\infty}^{\infty} e^{-i\omega t} \langle \mu(t) \mu(0) \rangle dt \quad (2.9)$$

at characteristic vibrational frequencies ω . That is, the infrared absorption is determined by the Fourier transform of the ensemble-averaged dipole time correlation function (the ensemble average is denoted by $\langle \rangle$). Ensemble-averaging is necessary in condensed-phase systems due to the variety of molecular conformations arising from the interaction with their environment. A statistical description of such systems is obtained with a density matrix formulation. Using the density matrix ρ , the ensemble average of an observable A follows from the evaluation of the trace:

$$\langle A \rangle = Tr[A\rho] \quad (2.10)$$

In liquid-phase vibrational spectroscopy, the surrounding solvent can often be treated as a heat bath. At finite temperature, thermal fluctuations of the bath cause fluctuating forces on vibrational coordinates. Therefore, such fluctuations directly contribute to the infrared lineshapes through the time correlation function in Eq. 2.9. The theoretical framework of lineshape analysis was initially formulated for the interpretation of NMR spectra [11–13] and later adopted for vibrational spectroscopy [14]. In the following, the main concepts that are necessary to extract time-resolved information from infrared spectra are briefly summarized.

2.1.2 Vibrational Lineshapes

It is assumed that the interaction between a molecule's vibrational mode and the bath is weak and that the bath is in thermal equilibrium (Markovian approximation). The Hamiltonian reads:

$$H = H_0 + H_B + H_{int} \quad (2.11)$$

Here, H_0 , H_B and H_{int} describe the vibrational degrees of freedom under consideration, the bath modes and the interaction between the vibrations and the bath, respectively. The eigenstates of H_B are inter- and intramolecular modes of the solvent or low-frequency modes of the solute itself. Typical interactions between the system and the bath arise from hydrogen bonding or other dipole-dipole interactions as well as long-range Coulomb forces. Due to the fluctuating forces originating from thermal fluctuations of the bath, the vibrational potential energy surface will change in time leading to a time-dependent transition frequency $\omega_{01}(t) \equiv \omega(t)$ (cf. Fig. 2.1) with:

$$\omega(t) = \omega_0 + \delta\omega(t) \quad (2.12)$$

Here $\delta\omega(t)$ is the time-dependent deviation from the time-averaged frequency ω_0 . The time scale of fluctuations directly reflects structural dynamics which are ultimately to be measured by time-resolved vibrational spectroscopy. Based on Eq. 2.12, one calculates the variance of frequency fluctuations $\Delta\omega$ and the correlation time τ_C :

$$\Delta\omega = \sqrt{\langle \delta\omega^2 \rangle} \quad (2.13)$$

$$\tau_C = \frac{1}{\langle \delta\omega^2 \rangle} \int_0^\infty \langle \delta\omega(t)\delta\omega(0) \rangle dt \quad (2.14)$$

Using these definitions, one defines the fast-modulation limit ($\Delta\omega\tau_C \ll 1$) in which the correlation between transition frequencies is quickly lost whereas the transition frequencies maintain their correlation in the slow-modulation limit ($\Delta\omega\tau_C \gg 1$). In essence, τ_C quantifies the decay of the *frequency fluctuation correlation function* (FFCF):

$$C(t) = \langle \delta\omega(t)\delta\omega(0) \rangle \quad (2.15)$$

The FFCF correlates frequency fluctuations at two different instants in time, thereby measuring how long the memory of a molecule's vibrational frequency is preserved. Frequency distributions due to heterogeneous molecular conformations are taken into account by applying the ensemble average so that the FFCF is a fundamental quantity to characterize time-dependent transition frequencies in condensed-phase systems.

The random modulation of a transition frequency $\omega(t)$ may be expressed by the equation of motion for the corresponding dipole moment

$$\dot{\mu}(t) = -i\omega(t)\mu(t) \quad (2.16)$$

with the formal solution:

$$\begin{aligned}\mu(t) &= \mu(0) \exp\left(-i \int_0^t \omega(t') dt'\right) \\ &= \mu(0) e^{-i\omega_0 t} \underbrace{\exp\left(-i \int_0^t \delta\omega(t') dt'\right)}_{\phi(t)}\end{aligned}\quad (2.17)$$

Substitution of Eq. 2.17 into 2.9 shows that the absorption profile centered at ω_0 is determined by the time-dependence of the relaxation function $\phi(t)$. The ensemble average $\langle\phi(t)\rangle$ describes the loss of coherence of initially coherent oscillators due to their fluctuating transition frequencies. Using a cumulant expansion one can show that [12]

$$\langle\phi(t)\rangle \approx \exp(-g(t)) \quad (2.18)$$

$$g(t) = \frac{1}{2} \int_0^t \int_0^t dt' dt'' \langle\delta\omega(t') \delta\omega(t'')\rangle \quad (2.19)$$

Equation 2.18 is exact for Gaussian frequency fluctuations. The equations above connect microscopic information in the form of the FFCF to experimentally observable infrared lineshapes. For stationary processes $\langle\delta\omega(t') \delta\omega(t'')\rangle$ is a function of the time difference $\tau = t'' - t'$ and the lineshape function $g(t)$ becomes:

$$g(t) = \int_0^t d\tau (t - \tau) \langle\delta\omega(\tau) \delta\omega(0)\rangle \quad (2.20)$$

In the Markovian limit, the FFCF may be approximated by an exponential decay so that:

$$\begin{aligned}g(t) &= (\Delta\omega)^2 \int_0^t d\tau (t - \tau) e^{-\tau/\tau_C} \\ &= (\Delta\omega)^2 \tau_C^2 (e^{-t/\tau_C} + t/\tau_C - 1)\end{aligned}\quad (2.21)$$

For slow frequency modulations, the exponential can be expanded in a Taylor series so that the leading term of the lineshape function is $g(t) \approx 1/2 (\Delta\omega)^2 t^2$. Consequently, a Gaussian infrared absorption profile of $\Delta\omega$ width will be observed directly reflecting the frequency spread of a static distribution of oscillators. The corresponding line broadening is therefore called *inhomogeneous* broadening. Fast frequency modulations lead to a linear lineshape function of $g(t) = (\Delta\omega)^2 \tau_C t$. As a result, the infrared absorption profile is a Lorentzian displaying a *homogeneous* linewidth $\Delta\omega_{hom}$ that is the inverse of the pure dephasing time T_2^* :

$$\Delta\omega_{hom} = \frac{2}{T_2^*} \quad (2.22)$$

$$T_2^* = \frac{1}{(\Delta\omega)^2 \tau_C} \quad (2.23)$$

Obviously, the linewidth decreases with decreasing correlation times τ_C . Due to the fast frequency modulations, only the average frequency is observed by the absorption spectra. This phenomenon is known as *motional narrowing* [12, 15].

In the liquid phase, a wide variety of inter- and intramolecular interactions occur simultaneously, e.g., the hydrogen-bond geometries of water are modulated on a fast sub-100 fs time scale whereas the hydrogen-bond lifetimes are in the range of 1–2 ps. If the frequency fluctuation correlation function is written as a superposition of a very fast and a very slow process, the infrared absorption profile has a Voigt shape. Often, a clear separation of time scales and a classification of infinitely fast and slow frequency modulations as discussed above is not possible. Accordingly, infrared lineshapes are insufficient to monitor the processes leading to frequency fluctuations on ultrafast time scales. Femtosecond infrared pulses allow for taking snap shots of instantaneous frequency distributions, providing the opportunity to follow the change of vibrational frequencies—a process called *spectral diffusion*. It will be shown in Sect. 2.2.1.2 how multidimensional, nonlinear time-resolved vibrational spectroscopies trace frequency fluctuations in real time, making them ideal tools to probe molecular dynamics.

2.1.3 Vibrational Relaxation

In time-resolved vibrational spectroscopy infrared pulses transiently generate non-equilibrium populations of vibrationally excited states. Energy relaxation to the weakly coupled bath modes brings the system back to thermal equilibrium. Often, a distinction is drawn between intra- and intermolecular relaxation pathways. While the former pathways involve other intramolecular vibrations or rotations and translations of the excited molecules, the latter pathways facilitate energy transfer to surrounding molecules. The associated vibrational lifetimes determine, for instance, the rate of chemical reactions and the relative amount of energy accepted by the solute and the solvent.

The rate of vibrational relaxation can be estimated with the help of Fermi's Golden Rule if the system-bath interaction represents a small perturbation (e.g., of a high frequency vibration with a transition frequency $\gg kT/\hbar \approx 200 \text{ cm}^{-1}$ at room temperature) [16, 17]. If we consider a vibrational degree of freedom that relaxes from $|i\rangle$ to $|j\rangle$ with $E_i - E_j = \hbar\omega_{ij} > 0$ (e.g., from the first excited state to the ground state) and denote the bath states with Greek letters ($|\alpha\rangle, |\beta\rangle, \dots$) the transition rate W_{ij} is given by:

$$W_{ij} = \frac{2\pi}{\hbar} \sum_{\alpha,\beta} \rho_\alpha |V_{i\alpha,j\beta}|^2 \delta(E_i - E_j + E_\alpha - E_\beta) \quad (2.24)$$

$V_{i\alpha,j\beta}$ is the coupling matrix element between the initial $|i\alpha\rangle$ and final $|j\beta\rangle$ states of the whole system and ρ_α denotes the initial distribution of bath states which is a Boltzmann distribution for a bath in thermal equilibrium: $\rho_\alpha \propto \exp(-E_\alpha/(kT))$. The delta-function ensures energy conservation, i.e., excess energy of the initially excited vibration must be accepted by the bath modes. Using the Fourier representation of the delta-function the relaxation rate becomes:

$$W_{ij}(\omega_{ij}) = \frac{1}{\hbar^2} \int_{-\infty}^{\infty} dt e^{-i\omega_{ij}t} \langle V_{ij}(t) V_{ji}(0) \rangle_B \quad (2.25)$$

Here, the time evolution of $V_{ij}(t) = \exp(iH_B t/\hbar) V_{ij} \exp(-iH_B t/\hbar)$ is determined by the bath Hamiltonian and $\langle \rangle_B$ stands for the average over the bath degrees of freedom. Equation 2.25 illustrates that besides a strong system-bath coupling V_{ij} the Fourier-amplitude of the fluctuations at the transition frequency contributes significantly to the relaxation rates.

If the bath is in thermal equilibrium, (downhill) energy relaxation should be the most probable process with $W_{ji} = \exp(-\hbar\omega_{ij}/(kT)) W_{ij}$ (cf. Eq. 2.24) leading to an irreversible vibrational population decay. This detailed-balance condition is not fulfilled by Eq. 2.25 but regained by writing the correlation function in terms of a symmetrized anticommutator $[V_{ij}(t), V_{ji}(0)]_+$ [18]:

$$W_{ij}(\omega_{ij}) = \frac{2}{\hbar^2 \left(1 + \exp\left(-\frac{\hbar\omega_{ij}}{kT}\right)\right)} \int_{-\infty}^{\infty} dt e^{-i\omega_{ij}t} \left\langle \frac{1}{2} [V_{ij}(t), V_{ji}(0)]_+ \right\rangle_B \quad (2.26)$$

It should be mentioned that here the relaxation rates are calculated from quantum-mechanical expectation values. However, theoretical correlation functions are mostly obtained from (semi-)classical molecular dynamics simulations which usually overestimate vibrational lifetimes [19, 20]. In order to improve the agreement between theory and experiment, additional quantum correction factors must be added to Eq. 2.26.

2.1.4 Molecular Vibrations as Local Probes in Hydrogen-Bonded Systems

Broadband steady state (linear) vibrational absorption spectra are routinely measured by Fourier transform infrared (FT IR) spectroscopy without relying on dispersive optics. Figure 2.2 is a collection of such spectra demonstrating the sensitivity of molecular vibrations to inter- and intramolecular interactions. The absorption of air in the range between 1000 and 4000 cm^{-1} is dominated by the two water stretching modes around 3750 cm^{-1} , the water bending mode around 1600 cm^{-1} and the anti-symmetric CO_2 stretching mode at 2400 cm^{-1} . Broad bands with individual narrow peaks exhibiting $\approx 1 \text{ cm}^{-1}$ linewidths are caused by the Franck-Condon progression

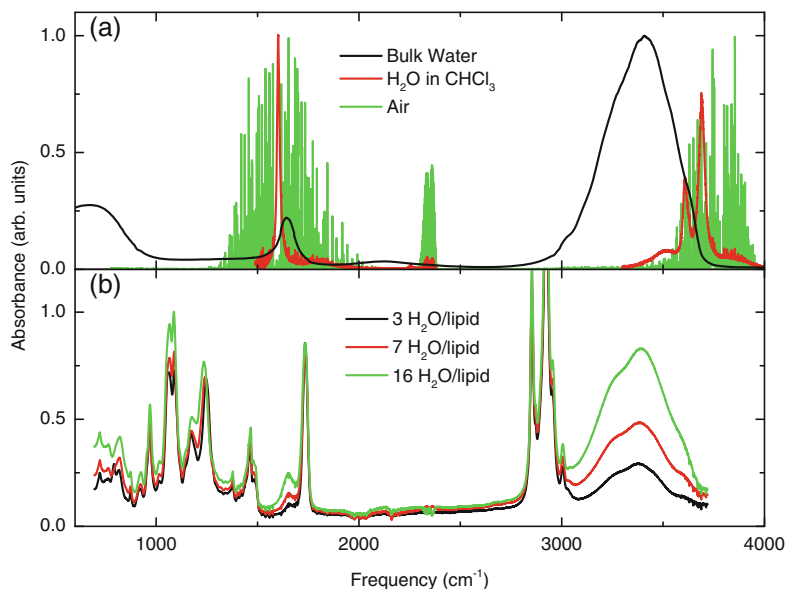


Fig. 2.2 Linear spectra of different water-containing systems. **a** FT IR spectra of bulk water forming intermolecular hydrogen bonds, water monomers in CHCl_3 solution and air demonstrating the spectral shifts of OH stretching and bending vibrations upon formation of hydrogen bonds that is accompanied by spectral broadening and changes of the transition dipole moments. **b** FT IR attenuated total reflectance spectrum of phospholipid films at different hydration levels. OH stretching and bending vibrations are clearly recognized by rising features as the water content is increased. Additional vibrational bands are the lipid marker modes

of rotational modes [21]. Rotational effects are much less pronounced for water monomers in a nonpolar solution. However, additional line broadening, e.g., due to the fluctuating solvent and decreased vibrational lifetime leads to the observation of increased linewidths compared to the individual gas phase peaks. The formation of a highly fluctuating hydrogen-bond network with a heterogeneous distribution of hydrogen-bond lengths and geometries in bulk water gives rise to broad infrared absorption spectra. Intermolecular hydrogen bonds modify the intramolecular potential energy surface in a way that the force constant of the stretching vibrations is decreased whereas it increases for the bending vibration. As a result, there is a redshift of OH stretching frequencies and blueshift of OH bending frequencies compared to the monomers. Such shifts are generally found in hydrogen-bonded systems with a magnitude that correlates with the hydrogen-bond length [22]. Typically, the redshift of OH stretching spectra is accompanied by an increase of the transition dipole moment [23]. Rotations of water molecules in the bulk phase are hindered due to the finite lifetime of hydrogen bonds. Therefore, librations around the three molecular axes represent the intermolecular vibrations with the highest frequencies (centered around 700 cm^{-1}).

Due to the variety of functional groups in a phospholipid molecule, the infrared absorption spectrum is rich of characteristic marker modes corresponding to different positions in the molecule. Figure 2.2b shows the FT IR attenuated total reflectance spectrum of phospholipid film made from 1,2-dioleoyl-sn-glycero-3-phosphocholine (DOPC)—the same molecule that we use for the preparation of reverse micelles (cf. Sect. 2.3.4). Some of the vibrations in the fingerprint range are the choline (975 cm^{-1}), phosphate (1090 and 1250 cm^{-1}) and carbonyl stretching (1735 cm^{-1}) vibrations whose dynamics will be discussed in Chap. 3. With increasing hydration levels the infrared absorption of water vibrations grows in and provides a probe of phospholipid hydration-shell dynamics as discussed in Chap. 4.

2.2 Theoretical Description of Nonlinear Spectroscopy

Throughout this thesis we will describe light pulses as classical electromagnetic waves with electric fields $\vec{E}(\vec{r}, t)$ that propagate in space and time and satisfy the wave equation

$$\left(\nabla^2 - \frac{1}{c^2} \frac{\partial^2}{\partial t^2}\right) \vec{E}(\vec{r}, t) = \mu_0 \frac{\partial^2}{\partial t^2} \vec{P}(\vec{r}, t). \quad (2.27)$$

Here μ_0 is the vacuum permeability and $\vec{P}(\vec{r}, t)$ is the polarization as a function of space and time. In Eq. 2.27 the polarization acts as a source for the electric field. Spectroscopy is the study of material properties by measuring the modulation of a light field due to light-matter interactions that create a polarization which in turn causes a new signal field $E_{sig}(\vec{r}, t)$ to be emitted:

$$E_{sig}(\vec{r}, t) \propto i P(\vec{r}, t) \quad (2.28)$$

Calculating $\vec{P}(\vec{r}, t)$ is thus a primary goal for theoretical descriptions of spectroscopy. The macroscopic polarization of a medium is directly connected to its microscopic dipole moments $\vec{\mu}$ by

$$\vec{P}(\vec{r}, t) \propto \langle \vec{\mu}(t) \rangle \quad (2.29)$$

with $\langle \rangle$ representing the ensemble average over all dipole moments. Changes in the expectation value $\langle \mu \rangle$ lead to a characteristic time-dependence of $\vec{P}(\vec{r}, t)$. The goal of mid-infrared spectroscopy in particular is to measure the emitted electric fields to gather microscopic information about the structure and dynamics of condensed phase molecular systems which are directly reflected by molecular vibrations.

In order to calculate the polarization in Eq. 2.29, a quantum statistical description of an ensemble of molecular dipoles interacting with an electric field is required. Often, a density matrix formalism combined with a perturbative expansion in terms

of electric fields is used to treat the light-matter interaction on a semiclassical level. A comprehensive formulation of this theory of nonlinear optical spectroscopy was developed by Mukamel [24]. Aspects of two-dimensional spectroscopy are covered by other textbooks [4, 25]. In the following, basic concepts of nonlinear spectroscopy based on the references mentioned above will be introduced.

2.2.1 Density Matrix Approach for Calculating Nonlinear Response Functions

Condensed-phase systems as investigated in this thesis consist of statistical ensembles. The density matrix ρ helps in describing such systems, e.g., the polarization as expectation value of the dipole operator $\vec{\mu}$ is obtained by evaluating the trace:

$$\vec{P}(t) = Tr [\vec{\mu}\rho(t)] \equiv \langle \vec{\mu}\rho(t) \rangle \quad (2.30)$$

The time evolution of a quantum system is determined by its Hamiltonian H , e.g., the interaction of a molecular dipole with an external electric field is described by

$$H(t) = H_0 + H_1(t) \quad (2.31)$$

$$H_1(t) = -\vec{\mu} \cdot \vec{E}(t) \quad (2.32)$$

where H_0 is the (time-independent) Hamiltonian of the unperturbed system and $H_1(t)$ accounts for the external perturbation due to the interaction of the molecular dipole operator $\vec{\mu}$ with an external electric field $\vec{E}(t)$. We assume that the solution of the time-independent Schrödinger equation for H_0 and therefore the density matrix before the interaction is known. The time evolution of the density matrix follows from the Liouville-von Neumann equation

$$\frac{d}{dt}\rho(t) = -\frac{i}{\hbar} [H, \rho(t)] \quad (2.33)$$

from which the polarization (Eq. 2.30) can be calculated. Consider a two-level system with the energy levels E_0 and E_1 that define the transition energy $E_{01} = E_1 - E_0 = \hbar\omega_{01}$. Then we get the following equations of motion for the matrix elements of ρ

$$\dot{\rho}_{00} = -i/\hbar (H_{1,01}\rho_{10} - \rho_{01}H_{1,10}) + \rho_{11}/T_1 \quad (2.34)$$

$$\dot{\rho}_{11} = -i/\hbar (H_{1,10}\rho_{01} - \rho_{10}H_{1,01}) - \rho_{11}/T_1 \quad (2.35)$$

$$\dot{\rho}_{01} = +i\omega_{01}\rho_{01} + i/\hbar H_{1,01}(\rho_{00} - \rho_{11}) - \rho_{01}/T_2 = \dot{\rho}_{10}^* \quad (2.36)$$

representing one form of the optical Bloch equations [26]. Here the last terms are phenomenologically added decay terms. That is, a non-equilibrium population inversion ($\rho_{11} - \rho_{00}$) described by the diagonal elements will decay to its equilibrium

value with the T_1 lifetime of the excited state if external perturbations are absent. Coherences described by the off-diagonal elements ρ_{ij} ($i \neq j$) oscillate at the transition frequency $\pm\omega_{01}$ and decay with the characteristic dephasing time T_2 . Since population relaxation destroys the phase relationship between coherent oscillators, it contributes to the dephasing time:

$$\frac{1}{T_2} = \frac{1}{T_2^*} + \frac{1}{2T_1} \quad (2.37)$$

Here, T_2^* is the pure dephasing time caused, e.g., by fluctuations of the solvent (cf. Eq. 2.17). So far we have neglected the influence of the perturbation Hamiltonian H_1 , which is insufficient to understand light-matter interactions as the basis for all types of spectroscopy.

In order to treat the effect of a time-dependent external perturbation, it is helpful to switch from the Schrödinger to the interaction picture. Operators in the interaction pictures (denoted by an index I) are defined as

$$A_I(t) = e^{+i/\hbar H_0(t-t_0)} A(t) e^{-i/\hbar H_0(t-t_0)} \quad (2.38)$$

and the Liouville-von Neumann equation reads:

$$\frac{d}{dt} \rho_I(t) = -\frac{i}{\hbar} [H_{1I}(t), \rho_I(t)] \quad (2.39)$$

The advantage of switching to the interaction picture is that now the time evolution is solely determined by the interaction Hamiltonian H_1 . Equation 2.39 is solved by formal integration and iterative solution:

$$\rho_I(t) = \rho_I(t_0) - \frac{i}{\hbar} \int_{t_0}^t d\tau [H_{1I}(\tau), \rho_I(t)] \quad (2.40)$$

$$\rho_I(t) = \rho_I(t_0) + \sum_{n=0}^{\infty} \rho_I^{(n)}(t) \quad (2.41)$$

$$\rho_I^{(n)}(t) = \left(-\frac{i}{\hbar}\right)^n \int_{t_0}^t d\tau_n \int_{t_0}^{\tau_n} d\tau_{n-1} \dots \int_{t_0}^{\tau_2} d\tau_1 [H_{1I}(\tau_n), [H_{1I}(\tau_{n-1}), [\dots, [H_{1I}(\tau_1), \rho_I(t_0)] \dots]]] \quad (2.42)$$

Inserting Eq. 2.32 into 2.42 and sending $t_0 \rightarrow -\infty$ the n th-order polarization

$P^{(n)}(t) = \langle \mu_I(t) \rho_I^{(n)}(t) \rangle$ becomes:

$$P^{(n)}(t) \propto -\left(-\frac{i}{\hbar}\right)^n \int_{-\infty}^t d\tau_n \int_{-\infty}^{\tau_n} d\tau_{n-1} \dots \int_{-\infty}^{\tau_2} d\tau_1 E(\tau_n) \cdot E(\tau_{n-1}) \dots E(\tau_1) \langle \mu(t) [\mu(\tau_n), [\mu(\tau_{n-1}), [\dots, [\mu(\tau_1), \rho(-\infty)] \dots]]] \rangle \quad (2.43)$$

Here we discarded the subscript I and the interaction picture is indicated by the time-dependence of $\mu(t)$. Changing the integration variables to time intervals ($\tau_1 = 0$, $t_1 = \tau_2 - \tau_1$, $t_2 = \tau_3 - \tau_2$, \dots , $t_n = t - \tau_n$), one obtains the n th-order nonlinear polarization as a convolution of n electric fields with the n th-order response function $R^{(n)}(t_n, t_{n-1}, \dots, t_1)$:

$$P^{(n)}(t) \propto \int_0^\infty dt_n \int_0^\infty dt_{n-1} \dots \int_0^\infty dt_1 E(t - t_n) E(t - t_n - t_{n-1}) \dots E(t - t_n - t_{n-1} - \dots - t_1) R^{(n)}(t_n, t_{n-1}, \dots, t_1) \quad (2.44)$$

where

$$R^{(n)}(t_n, t_{n-1}, \dots, t_1) = - \left(-\frac{i}{\hbar} \right)^n \langle \mu(t_n + t_{n-1} + \dots + t_1) [\mu(t_n), [\mu(t_{n-1}), [\dots, [\mu(t_1), \rho(-\infty)] \dots]]] \rangle \quad (2.45)$$

Equation 2.45 has an intuitive physical interpretation. Each commutator represents a field-matter interaction at time t_i caused by the action of the dipole operator $\mu(t_i)$ on the density matrix. The number of commutators determines the number of field interactions and is directly related to linear and nonlinear experiments. To introduce the effects of the dipole operator interacting with the density matrix, we will first describe the linear (first-order) response before evaluating the third-order response functions that are necessary to describe 2D IR and pump-probe experiments.

2.2.1.1 Linear Response: Free Induction Decay and Absorption

The first-order nonlinear response function $R^{(1)}(t)$ according to Eq. 2.45 reads:

$$R^{(1)}(t) = i/\hbar \langle \mu(t)\mu(0)\rho(-\infty) - \mu(t)\rho(-\infty)\mu(0) \rangle \quad (2.46)$$

That is, the dipole operator $\mu(0)$ acts on the density matrix from the left (on the ket) in the first term and from the right (on the bra) in the second one. For example, consider a two-level system without permanent dipoles and a transition dipole moment of μ_{01} . If the system is in the ground state before a laser pulse arrives, the density matrix and the dipole operator are given by:

$$\rho(-\infty) = \begin{pmatrix} 1 & 0 \\ 0 & 0 \end{pmatrix} = |0\rangle \langle 0|, \quad \mu = \mu_{01} \begin{pmatrix} 0 & 1 \\ 1 & 0 \end{pmatrix} = \mu_{01} (|0\rangle \langle 1| + |1\rangle \langle 0|) \quad (2.47)$$

Evaluating the corresponding products in Eq. 2.46, we find that the two terms generate different off-diagonal elements of the density matrix: $\mu(0)\rho(-\infty) \propto \mu_{01} |1\rangle \langle 0|$, $\rho(-\infty)\mu(0) \propto \mu_{01} |0\rangle \langle 1|$. Their time evolution $e^{-i\omega_{01}t} e^{-t/T_2}$ and $e^{+i\omega_{01}t} e^{-t/T_2}$ is obtained by integrating Eq. 2.36. The multiplication with $\mu(t)$ in Eq. 2.46 corresponds

to an emission process and brings the system back to its ground state so that the response function reads:

$$R^{(1)}(t) = i/\hbar\mu_{01}^2 \left(e^{-i\omega_{01}t} - e^{+i\omega_{01}t} \right) e^{-t/T_2} \propto \sin(\omega_{01}t) e^{-t/T_2} \quad (2.48)$$

The first-order polarization is obtained by assuming a real electric field of the laser pulse:

$$E(t) = \hat{E}(t) \left(e^{-i\omega t} + e^{i\omega t} \right) = \mathcal{E}(t) + \mathcal{E}^*(t) \quad (2.49)$$

Here, $\hat{E}(t)$ is a time-dependent envelope of the field, ω is its frequency and the terms $\mathcal{E}(t)$, $\mathcal{E}^*(t)$ represent the positive and negative-frequency contribution to the total electric field $E(t)$. In vibrational spectroscopy, the resonance condition $\omega = \omega_{01}$ is usually fulfilled. Substituting this ansatz together with Eq. 2.48 into Eq. 2.44, we find that two terms oscillate with a frequency of $\pm 2\omega_{01}$ so that the integral is small compared to the slowly varying terms. In neglecting these contributions, the rotating wave approximation is applied.

The result of the preceding paragraphs is often illustrated by double-sided Feynman diagrams (Fig. 2.3) that can also be generalized to higher-order responses and lead to a convenient way of calculating nonlinear response functions. Time evolves from the bottom to the top and the current state of the density matrix is indicated. Field interactions are depicted by solid arrows. Interactions with the positive-frequency and negative-frequency part of the electric field (\mathcal{E} and \mathcal{E}^*) are depicted by arrows pointing to the right and to the left, respectively. Furthermore, dashed arrows are used to visualize the multiplication with the dipole operator that is not part of the commutators. Each field interaction produces a factor $-i/\hbar$ and each interaction from the right causes a factor of -1 (due to the commutators).

When the response functions are known, the polarization (Eq. 2.44) can be calculated and the emitted electric field follows from Eq. 2.28. An approximation frequently used is the semi-impulsive limit in which the pulses are short compared to vibrational dynamics but long compared to the oscillation period of the light field so that $\hat{E}(t) = \hat{E}\delta(t)$ (with the Dirac delta function $\delta(t)$). In this case, the polarization is directly proportional to the response function. For example, the first term in Eq. 2.48 generates a polarization that oscillates at the frequency $+\omega_{01}$ acting as a source for an

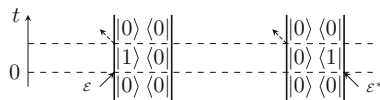


Fig. 2.3 Double-sided Feynman diagrams for the first-order response function. The *left hand side* diagram corresponds to the first term in Eq. 2.46 interacting with the positive-frequency part of the electric field whereas the *right hand side* diagram shows the second term interacting with the negative-frequency part of the electric field

electric field that is π -phase shifted with respect to the driving light field. Absorption is therefore caused by a destructive interference between the incident field and the emitted field originating from the so-called free induction decay. It should be noted that the second diagram is just the complex conjugate of the first one and therefore does not carry additional information.

In Eq. 2.48, dephasing is incorporated phenomenologically by the decay term e^{-t/T_2} . The dephasing is a result of fluctuating transition frequencies due to the interaction with a bath as discussed in Sect. 2.1.2. Assuming that the fluctuations define the instantaneous frequency ($\omega_{01}(t) = \omega_{01} + \delta\omega_{01}(t)$) and taking the ensemble average gives:

$$\begin{aligned} |0\rangle\langle 1| &= \rho_{01}(t) \propto \left\langle \exp\left(-i \int_0^t \omega_{01}(t') dt'\right) \right\rangle \\ &= e^{-i\omega_{01}t} \left\langle \exp\left(-i \int_0^t \delta\omega_{01}(t') dt'\right) \right\rangle \end{aligned} \quad (2.50)$$

This result is equivalent to Eq. 2.17. That is, applying the cumulant expansion we get the infrared absorption profile as Fourier transform of an exponential of the lineshape function (Eq. 2.19):

$$A(\omega) \propto \Re\left(i \int P^{(1)}(t) e^{i\omega t} dt\right) \propto \mu_{01}^2 \Re\left(\int e^{i(\omega - \omega_{01})t - g(t)} dt\right) \quad (2.51)$$

$g(t)$ is directly related to the frequency fluctuation correlation function $C(t)$. $C(t)$ contains information about the system-bath interaction and is one of the key quantities to be measured with vibrational spectroscopy. However, extracting the frequency fluctuation correlation function would require the impossible operation of inverting Eq. 2.51. Additionally, lineshape fitting by assuming an analytical form of $C(t)$ is often misleading because of the congested nature of condensed-phase linear absorption spectra e.g., due to the different time scales of the processes involved that lead to frequency modulations. The next section will show how third-order spectroscopy helps in revealing different line broadening contributions more reliably.

2.2.1.2 Third-Order Nonlinear Response: Four-Wave Mixing

For symmetry reasons, even-order nonlinear response functions vanish in isotropic media. Therefore, the lowest-order nonlinearity in liquid molecular systems is usually described by the third-order response function $R^{(3)}$ that is responsible for so-called four-wave mixing processes. In such processes three field interactions occur with the laser field:

$$E(t) = \hat{E}_1(t) e^{i(\vec{k}_1 \vec{r} - \omega_1 t + \Phi_1)} + \hat{E}_2(t) e^{i(\vec{k}_2 \vec{r} - \omega_2 t + \Phi_2)} + \hat{E}_3(t) e^{i(\vec{k}_3 \vec{r} - \omega_3 t + \Phi_3)} + c.c. \quad (2.52)$$

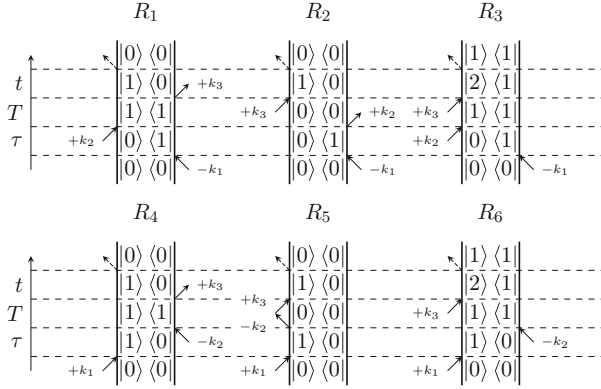


Fig. 2.4 Double-sided Feynman diagrams for the third-order response functions for the rephasing ($-\vec{k}_1 + \vec{k}_2 + \vec{k}_3$) and non-rephasing ($+\vec{k}_1 - \vec{k}_2 + \vec{k}_3$) phase-matching conditions

Here, \hat{E}_i , \vec{k}_i , ω_i and Φ_i are the field envelopes, wave vectors, frequencies and phases of the i th laser field, respectively. Since energy and momentum conservation must be obeyed, the conditions $\omega_{sig} = \pm\omega_1 \pm \omega_2 \pm \omega_3$ and $\vec{k}_{sig} = \pm\vec{k}_1 \pm \vec{k}_2 \pm \vec{k}_3$ (phase matching) must be fulfilled for the signal's frequency and wave vector. The signs depend on the phases of the electric fields involved. A straightforward generalization of the formalism developed in the previous section leads to the six third-order Feynman diagrams for the phase matching directions $\vec{k}_{sig} = \mp\vec{k}_1 \pm \vec{k}_2 + \vec{k}_3$ shown in Fig. 2.4 where the phase of the electric field is indicated by its wave vector. Similar to the linear response, terms that do not survive the rotating wave approximation as well as the complex conjugates that do not carry additional information are neglected.

Figure 2.5 schematically depicts the pulse sequence connected with these diagrams. The first pulse generates a coherence. As in the linear response, dephasing leads to a decay of the off-diagonal density matrix elements in the form of a free induction decay. After the *coherence time* τ , a second pulse prepares the system in a population state. During the *population time* T , the system evolves freely before the third pulse generates a coherence again. The resulting polarization is the source for the emitted signal field. Four-wave mixing is often illustrated by noticing that the first two pulses of the sequence generate a holographic population and frequency grating from which the third pulse is diffracted off [27, 28]. Population relaxation and spectral diffusion wash out the grating so that the two processes can be studied by varying the population time.

Note that the time evolution during the coherence times carries different signs for R_1 – R_3 compared to R_4 – R_6 , e.g.:

$$R_1(\tau, T, t) = -(-i/\hbar)^3 \left\langle \mu_{01}^4 e^{+i\omega_{01}\tau} e^{-\tau/T_2} e^{-T/T_1} e^{-i\omega_{01}t} e^{-t/T_2} \right\rangle \propto \left\langle e^{-i\omega_{01}(t-\tau)} \right\rangle \quad (2.53)$$

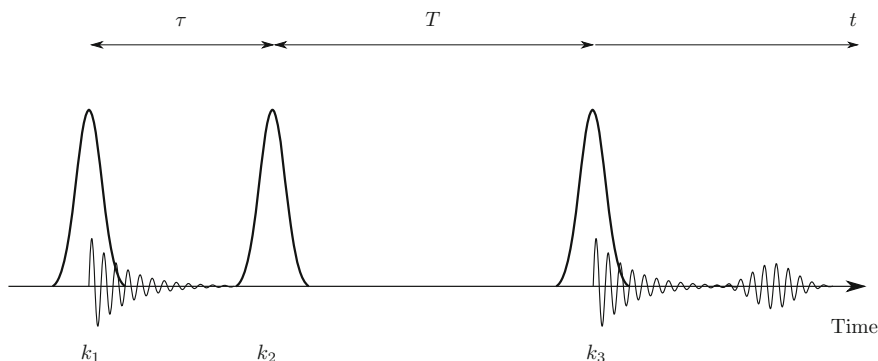


Fig. 2.5 Pulse sequence for the generation of a third-order nonlinear polarization. The first pulse creates a coherence that decays with a characteristic dephasing time. A second pulse creates a population state after the coherence time τ . After the population time T , the third pulse creates a coherence again and the resulting third-order nonlinear polarization is the source for the emitted signal field. The linear polarization after the first field interaction and nonlinear polarization after the third field interaction are schematically shown as oscillating lines

$$R_4(\tau, T, t) = -(-i/\hbar)^3 \left\langle \mu_{01}^4 e^{-i\omega_{01}\tau} e^{-\tau/T_2} e^{-T/T_1} e^{-i\omega_{01}t} e^{-t/T_2} \right\rangle \propto \left\langle e^{-i\omega_{01}(t+\tau)} \right\rangle \quad (2.54)$$

In the case of inhomogeneous broadening, diagrams R_1 – R_3 cause a macroscopic polarization at $t = \tau$ that will emit a signal field after the free induction decay—a phenomenon called photon echo. R_1 – R_3 are therefore referred to as *rephasing* Feynman diagrams while R_4 – R_6 are the *non-rephasing* diagrams.

R_1 and R_4 are in the $v = 1$ state after the second field interaction whereas R_2 and R_5 are in the ground state. Although their evolution during the population is the same, the origin of the signal is different with the former being caused by the stimulated emission from the $v = 1$ state and the latter stemming from the ground state bleach. Both contributions appear at the same spectral positions. Diagrams R_3 and R_6 are in a $|2\rangle \langle 1|$ -coherence after the third field interaction, therefore sensitive to the $v = 1$ to 2 absorption that is red-shifted due to the anharmonicity of condensed-phase molecular vibrations. Note that only one field interaction from the right occurs so that these diagrams generate signals with an opposite sign compared to the ones discussed before.

While the stimulated emission and excited state absorption decay with the T_1 lifetime, the ground-state bleaching decay may be delayed when the excitation does not relax to the ground state $|0\rangle$ directly. Instead one often speaks of a so-called hot ground state $|0'\rangle$ where the population of anharmonically coupled low-frequency modes causes a persistent bleaching of the initially excited transition. The corresponding time-dependent amplitude maps the recovery of the original ground state, thus giving insight into the thermalization of the sample. Since the ground state bleach and excited state emission signals arise at the same frequency positions, the

time evolution of the excited state absorption is the most direct way to extract the excited state lifetime.

In order to calculate the third-order nonlinear polarization (Eq. 2.44), the ensemble average has to be evaluated. Using the cumulant expansion and the definition of the lineshape functions (Eq. 2.19), the rephasing and non-rephasing response functions take the following form:

$$R_{1,2,3}(\tau, T, t) = -2i/\hbar^3 \mu_{01}^4 \left(e^{-i\omega_{01}(t-\tau)} - e^{-i((\omega_{01}-\Delta)t-\omega_{01}\tau)} \right) e^{-(\tau+t)/(2T_1)} e^{-T/T_1} \cdot e^{-g(\tau)+g(T)-g(t)-g(\tau+T)-g(T+t)+g(\tau+T+t)} \quad (2.55)$$

$$R_{4,5,6}(\tau, T, t) = -2i/\hbar^3 \mu_{01}^4 \left(e^{-i\omega_{01}(t+\tau)} - e^{-i((\omega_{01}-\Delta)t+\omega_{01}\tau)} \right) e^{-(\tau+t)/(2T_1)} e^{-T/T_1} \cdot e^{-g(\tau)-g(T)-g(t)+g(\tau+T)+g(T+t)-g(\tau+T+t)} \quad (2.56)$$

Here we made use of the harmonic approximation for the transition dipole moments $\mu_{12} = \sqrt{2}\mu_{01}$ and introduced the anharmonicity $\Delta = \omega_{01} - \omega_{12}$; we implicitly assumed that the FFCF of the $v = 0$ to 1 is the same as that of the $v = 1$ to 2 transition. Note that from Eq. 2.47 onward we neglected the time-dependence of the dipole moment's amplitude corresponding to the Condon-approximation. The assumption is not applicable for calculations of water OH stretching lineshapes where frequency shifts due to fluctuating hydrogen-bond geometries are accompanied by changes of the transition dipole moment [29].

Two-Dimensional Infrared Spectroscopy

Measuring the response functions in its dependency of all three time delays opens the possibility of obtaining two-dimensional infrared (2D IR) spectra. Although this work concentrates on vibrational spectroscopy, most of the concepts presented in the following are applicable to 2D spectroscopy in general from the UV to the mid-infrared. One way to measure 2D spectra is depicted in Fig. 2.6a. Three pulses with

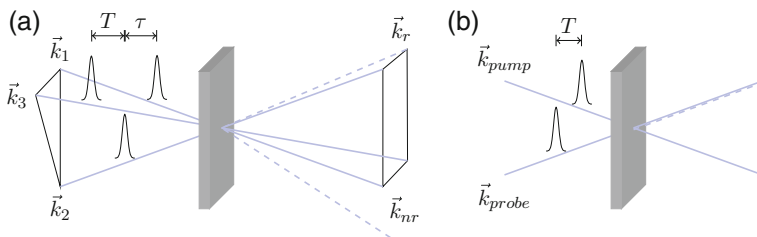


Fig. 2.6 Schematic representation of **a** two-dimensional infrared and **b** pump-probe experiments. In **a**, the coherence time τ and population time T can be varied allowing for a discrimination of the rephasing ($\vec{k}_r = -\vec{k}_1 + \vec{k}_2 + \vec{k}_3$) and non-rephasing signals ($\vec{k}_{nr} = +\vec{k}_1 - \vec{k}_2 + \vec{k}_3$). In **b**, the only free parameter is T and the signal is emitted in the direction of the probe

different wave vectors and tuneable time delays interact in the sample so that the non-linear polarization emits a signal field E_{sig} in the rephasing and non-rephasing phase matching directions $\vec{k}_r = -\vec{k}_1 + \vec{k}_2 + \vec{k}_3$ and $\vec{k}_{nr} = +\vec{k}_1 - \vec{k}_2 + \vec{k}_3$. Section 2.3.2 describes one possibility to measure E_{sig} by means of spectral interferometry. Compared to the linear case, the third-order response $R(\tau, T, t)$ contains two coherence periods (τ and t). A two-dimensional Fourier transform converts the response functions into the frequency domain so that the response functions $R(\omega_1, T, \omega_3)$ correlate the *excitation frequency* ω_1 and *detection frequency* ω_3 .

The most common way to show such correlation plots are so-called absorptive 2D spectra $S(\omega_1, T, \omega_3)$ for which the rephasing and non-rephasing terms are added [30, 31]:

$$S(\omega_1, T, \omega_3) = \Re \left\{ i \left(\sum_{n=1}^3 R_n(-\omega_1, T, \omega_3) + \sum_{n=4}^6 R_n(+\omega_1, T, \omega_3) \right) \right\} \quad (2.57)$$

Here, the semi-impulsive limit was applied. Note that the rephasing terms are evaluated as a function of $-\omega_1$ so that the positive-frequency part of the 2D spectrum is composed of rephasing and non-rephasing spectra lying in the same quadrant of the (ω_3, ω_1) -plane.

Some capabilities behind the general approach of 2D spectroscopy are illustrated in Fig. 2.7 for a system consisting of two non-interacting oscillators (ν_a, ν_b) at the frequencies ω_a and ω_b with a T_1 lifetime of 1.5 and 1.0 ps, respectively, and two different FFCFs (Fig. 2.7b). A constant was chosen for ν_a while ν_b follows a Kubo ansatz with a correlation time of 500 fs. The amplitude of both FFCFs are the same. Extracting the line broadening contributions from the linear spectra (Fig. 2.7a, calculated with Eq. 2.51) would involve a careful peak shape analysis of the partly overlapping bands.

The information content of 2D spectra for population times of 50 and 500 fs as shown in Fig. 2.7c, d and calculated with Eq. 2.57 is much larger. Both vibrations show a positive feature (yellow-red contours) along the diagonal ($\omega_1 = \omega_3$) due to the ground state bleach and excited state emission as well as a negative signal (blue contours) anharmonically red shifted with respect to the detection-frequency axis caused by the excited state absorption. The signal contributions decay with increasing T according to their lifetime. Dramatic differences are observed for the peak shapes. Since 2D spectra measure correlations between the excitation and detection frequency, their shape is dictated by the course of the FFCF. The correlation between these frequencies for inhomogeneously broadened transitions is reflected in stationary lineshapes that are elongated along the diagonal as shown for the peaks of ν_a . For non-constant FFCFs such as in the case of ν_b , a vibration's memory of its initial excitation frequency is gradually extinguished leading to round (homogeneous) 2D lineshapes on the time scale of frequency fluctuations. Generally, the diagonal width of a 2D peak reflects its total linewidth whereas the antidiagonal width is determined by the homogeneous linewidth including contributions from pure dephasing and the finite vibrational lifetime (cf. Eq. 2.37) [32, 33].

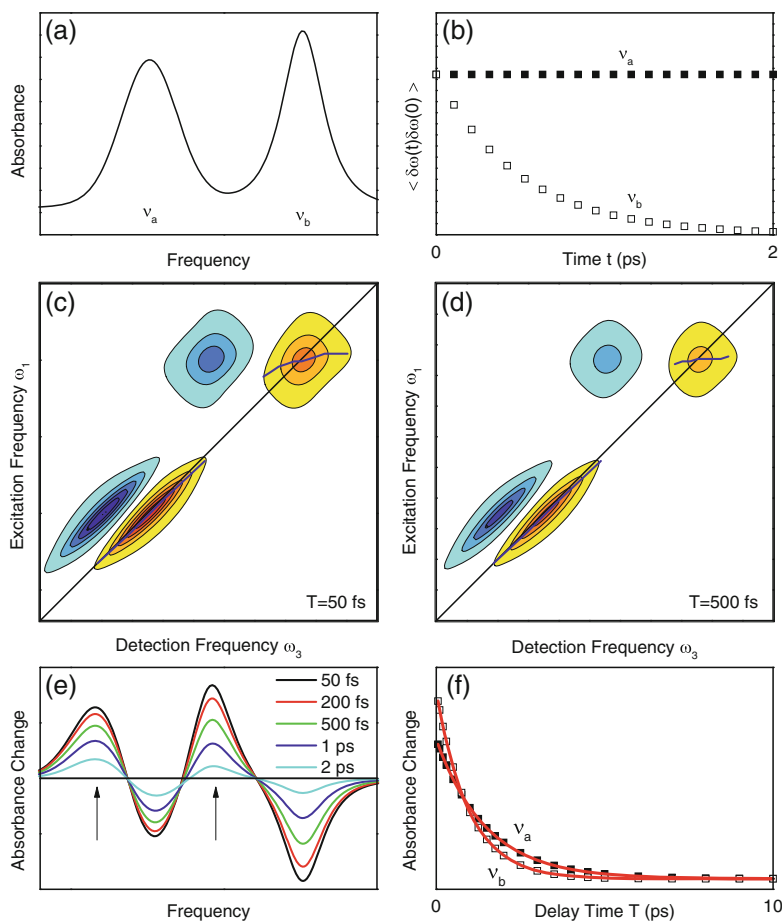


Fig. 2.7 Calculated **a** linear, **c**, **d** 2D, and **e** pump-probe spectra of two transitions ν_a and ν_b for a FFCF shown in **b**. Along the diagonal ($\omega_1 = \omega_3$) the 2D spectra show positive peaks (yellow, red) originating from the ground state bleach and stimulated emission. The negative excited state absorption signal (blue) is anharmonically red-shifted along the detection-frequency axis. Inhomogeneous broadening of ν_a results in spectra elongated along the diagonal whose antidiagonal width is determined by the lifetime broadening. The FFCF of ν_b decays on a 500 fs time scale leading to a reshaping its 2D spectrum. Those features are not resolved in pump-probe spectra **e** due to the integration along the excitation-frequency axis which also leads to a stronger overlap of the two signal contributions for ν_a . **f** The time evolution of the excited state absorption at the frequencies indicated by arrows in **e** reveals T_1 lifetimes of 1.5 and 1.0 ps, respectively

Frequently, center lines that are plotted as blue lines in Fig. 2.7c, d are used for a quantitative 2D lineshape analysis. They are constructed by scanning the detection-frequency axis and connecting the respective points with a maximum signal amplitude along the excitation-frequency axis. Round peak shapes originating from homogeneous lineshapes give horizontal lines with a *center line slope* (CLS) of zero. In

contrast, inhomogeneous lineshapes that are elongated along the diagonal have a CLS of 1. Plotting the CLS as a function of population time allows for a quantification of spectral reshaping rates (i.e., spectral diffusion) of 2D peaks. It is often assumed that the CLS decay or the change of the eccentricity of 2D spectra is directly proportional to the FFCF [34, 35]. This assumption is only true within a so-called short-time approximation [36] and for Gaussian frequency fluctuations. It has been shown to be invalid for some realistic systems [37, 38].

In addition to the information obtained by a lineshape analysis, 2D spectra are able to reveal anharmonic couplings between different vibrations which were briefly discussed in Sect. 2.1.1. Generally, a system of two coupled oscillators can be described in a normal-mode picture or in an exciton picture [39, 40]. In both cases, couplings give rise to an energy level scheme which contains all information about diagonal and off-diagonal anharmonicities. Off-diagonal anharmonicities cause the appearance of (off-diagonal) *cross peaks* in the 2D spectrum. For instance, a population of one vibration results in a depopulation of the common ground state, i.e., there will also be a bleach of the fundamental transition of the second vibration so that an off-diagonal signal will occur at the excitation frequency of the first and the detection frequency of the second mode. Additional signals due to absorption of combination modes cause a second contribution to the cross peaks which permits the direct observation of off-diagonal vibrational couplings.

An instantaneous response is expected if anharmonic coupling is the only mechanism leading to cross-peak signals. However, cross peaks also indicate population transfer from one mode to another. In this case, they follow a more complicated time evolution that is determined by the time constants of the initial energy transfer and the subsequent population relaxation of the energy-accepting vibration.

Pump-Probe Spectroscopy

Pump-probe spectroscopy is a special case of third-order nonlinear spectroscopy where the first two field interactions originate from the same pump pulse, i.e., $\vec{k}_1 = \vec{k}_2 = \vec{k}_{pump}$ and $\tau = 0$ (cf. Fig. 2.6b). A pump-probe signal is therefore emitted in the direction of the probe $\vec{k}_{sig} = -\vec{k}_{pump} + \vec{k}_{pump} + \vec{k}_{probe}$ so that the probe and signal fields interfere on the detector giving rise to a pump-induced *absorbance change*

$$\Delta A = -\log \left(T_{sample} / T_{sample}^{(0)} \right) \quad (2.58)$$

where T_{sample} and $T_{sample}^{(0)}$ represent the sample transmission with and without pump excitation. From an experimental point of view, pump-probe spectroscopy is easier to implement than 2D IR techniques because it involves only two beams and one time delay. The price one has to pay is that the frequency resolution along the excitation axis is lost. If the pump pulses are approximated as delta pulses with a flat spectrum, fixing $\tau = 0$ results in pump-probe spectra that are equivalent to 2D spectra integrated along the excitation-frequency axis.

Figure 2.7e shows transient pump-probe spectra as a function of the pump-probe delay time (i.e., the population time T in 2D spectra). Negative absorbance changes are caused by the ground state bleach and excited state emission pathways. The anharmonicity causes red-shifted positive signals due to the excited state absorption. Note that by convention, the sign of 2D and pump-probe signals is different. The pump-probe spectra do not offer an intuitive way of distinguishing different line broadening mechanisms. Moreover, they suffer from overlapping contributions of different signals. For example, comparison between 2D and pump-probe spectra of ν_a reveals that the latter are strongly influenced by an overlap of the ground and excited state pathways due to the pronounced inhomogeneous lineshape and the small anharmonicity. While the two signal contributions are well separated for ν_b , other overlapping pump-probe contributions occur due to the $v = 0$ to 1 transition of ν_a and the $v = 1$ to 2 transition of ν_b . Additional cancellation effects would be observed if anharmonic couplings and energy transfer between ν_a and ν_b were included in the model calculations.

If all signal contributions are well separated, the pump-probe technique offers the advantage of only having to scan one time delay to measure excited state lifetimes. An example is shown in Fig. 2.7f that shows the time evolution of the excited state absorption as a function of the pump-probe delay time (T). In agreement with the parameters put into the model, the signals fit well to monoexponential decays with time constants of 1.5 and 1.0 ps for ν_a and ν_b , respectively (red lines).

Experiments are conducted with pulses of finite duration. Therefore, a sequential interaction as assumed so far is not always fulfilled. At pulse delays shorter than the pulse duration additional field interactions occur causing spikes in the time-resolved measurements. Those artifacts, commonly referred to as *coherent pump-probe coupling*, may partly mask a molecule's response around zero delay times.

Negative delay times correspond to a situation when the probe interaction precedes the arrival of the pump pulse. As a consequence, the probe creates a coherence followed by a free induction decay that can be perturbed by the pump interactions. The corresponding pump-probe signals at negative delay times are therefore called perturbed free induction decay and can give information about dephasing properties of the system [41].

In the theoretical description of the nonlinear response, we neglected that the dipole interaction (Eq. 2.32) has the form of a dot product, i.e., Eq. 2.44 should carry a proportionality factor that depends on the relative orientation of the transition dipole and the electric field polarization at the time of each interaction. There are different mechanisms leading to a reorientation of transition dipoles between two interactions, e.g., rotation of a molecule or functional group as well as intermolecular energy transfer. It was recognized in time-resolved fluorescence [42, 43] and later applied to time-resolved vibrational spectroscopy [44] that the use of linearly polarized pulses allows for measuring the time scales of such reorientations. The idea is as follows: If a light pulse is linearly polarized along the z -axis of a Cartesian coordinate system then the interaction probability with a dipole moment is proportional to its z -component.

Expressing the dipole moment in spherical coordinates with the polar and azimuthal angles Θ and Φ , the initial normalized distribution of excited dipoles after the first two field interactions is

$$W(\Theta_0, \Phi_0) = \frac{3}{4\pi} \cos^2 \Theta_0 = \frac{3}{4\pi} (1 + P_2(\cos \Theta_0)) \quad (2.59)$$

with the second-order Legendre polynomial P_2 . The probability to find a dipole at the angles (Θ, Φ) after the time T provided that it was initially aligned at (Θ_0, Φ_0) , can be expressed in terms of spherical harmonic functions. We then calculate the probability that the signal, e.g., generated in a pump-probe experiment, is emitted parallel ($\Delta A_{||}$) or perpendicular (ΔA_{\perp}) to the excitational polarization. If the vibrational population relaxes directly to the ground state, the pump-probe signal is proportional to the probability $P_v(T)$ of a vibrational excitation to survive during the population time and we get:

$$\Delta A_{||}(T) \propto P_v(T) \left(\frac{1}{3} + \frac{4}{15} \left\langle P_2 \left[\hat{\mu}(T) \hat{\mu}(0) \right] \right\rangle \right) \quad (2.60)$$

$$\Delta A_{\perp}(T) \propto P_v(T) \left(\frac{1}{3} - \frac{2}{15} \left\langle P_2 \left[\hat{\mu}(T) \hat{\mu}(0) \right] \right\rangle \right) \quad (2.61)$$

Here $\hat{\mu}(T)$ is the unit vector in the direction of a dipole moment at time T and $\langle \rangle$ denotes the ensemble average. The *anisotropy*

$$r(T) = \frac{\Delta A_{||}(T) - \Delta A_{\perp}(T)}{\Delta A_{||}(T) + 2 \cdot \Delta A_{\perp}(T)} = \frac{2}{5} \left\langle P_2 \left[\hat{\mu}(T) \hat{\mu}(0) \right] \right\rangle \quad (2.62)$$

is therefore a direct measure of orientational relaxation. Note that the denominator that is often referred to as *isotropic absorbance change*

$$\Delta A_{iso} = \frac{1}{3} (\Delta A_{||}(T) + 2 \cdot \Delta A_{\perp}(T)) \propto P_v(T) \quad (2.63)$$

does not contain reorientational effects and is the most direct probe for vibrational relaxation. It should be mentioned that the picture of reorienting transition dipoles is only correct for direct vibrational relaxation to the ground state. If pump-probe signals are dominated by anharmonic couplings to low-frequency modes populated after intermolecular energy relaxation, the anisotropy at population times longer than the vibrational lifetime is influenced by oscillators that were not excited initially.

The control of the polarization of all pulses in a nonlinear experiment is useful to suppress or enhance certain Feynman diagrams involving vibrational transitions that are not parallel to each other. Polarization control is therefore often applied in 2D IR or higher-order spectroscopy to enhance cross peaks with respect to the diagonal ones. A detailed description is given in Chap. 5 of [4].

2.3 Experimental

2.3.1 Generation and Characterization of Short Tuneable Mid-Infrared Pulses

With Ti:sapphire as a laser gain medium [45], reliable near-infrared femtosecond lasers are fundamental tools for ultrafast spectroscopy. Amplified laser systems with kHz-repetition rates and mJ-pulse energies are now commercially available. Two different laser systems were used for the 2D IR (Coherent Micra+Elite, <40 fs pulse duration, 2.5 mJ pulse energy, 1 kHz repetition rate) and two-color pump-probe (Coherent Libra HE, 45 fs pulse duration, 3.5 mJ pulse energy, 1 kHz repetition rate) experiments presented in this thesis.

A convenient method to generate tuneable femtosecond pulses in the mid-infrared is nonlinear parametric frequency conversion [46]. Figure 2.8 depicts the experimental setup of such a frequency converter. Near-infrared 800 nm pulses (pulse energy 0.7 mJ) from an amplified laser system are split into three arms with different pulse energies. The smallest fraction of energy is used for supercontinuum generation in a sapphire plate (1 mm thickness). Signal and idler pulses with pulse energies in the sub- μJ range are obtained by optical parametric amplification of the supercontinuum in a BBO crystal (type II, $\theta = 25^\circ$, 4 mm thickness). Using the signal as a seed for a second amplification in the same BBO crystal leads to high-energy ($\approx 150 \mu\text{J}$) signal and idler radiation. An optional third amplification with a 2 mm thick BBO yields $>250 \mu\text{J}$. Difference frequency generation of signal and idler in GaSe (for $1000\text{--}2500 \text{ cm}^{-1}$, type II, z-cut $\theta = 14^\circ$, 0.5–1 mm thickness) or AgGaS₂ (for $2500\text{--}3500 \text{ cm}^{-1}$, type I, $\theta = 42^\circ$, 0.5–1 mm thickness) delivers intense femtosecond pulses in the mid-infrared. Pulse energies of $2 \mu\text{J}$ with pulse durations of 70–150 fs depending on the output frequency are obtained with two amplifications, whereas a third amplification leads to $7 \mu\text{J}$ at 50–100 fs. All parameters of the pulses used in the experiments are given in the appendix (Table A.1, p. 100).

Due to the limited response times of photodetectors, a direct measurement of the electric field of optical pulses is impossible. Therefore, a broad set of referencing techniques combined with time-integrating detectors is used for ultrashort pulse characterization. In the simplest case, a pulse is referenced with itself by a nonlinear second-order process in an autocorrelation setup [47]. For pump-probe experiments, one is interested in the time resolution of the experiment that is given by the cross-correlation of the pump and probe pulses. The time-integrated (second-order) cross-correlation signal I_{XC} reads:

$$I_{XC}(\tau) \propto \int_{-\infty}^{\infty} |E_{pump}(t) \cdot E_{probe}(t - \tau)|^2 dt = \int_{-\infty}^{\infty} I_{pump}(t) I_{probe}(t - \tau) dt \quad (2.64)$$

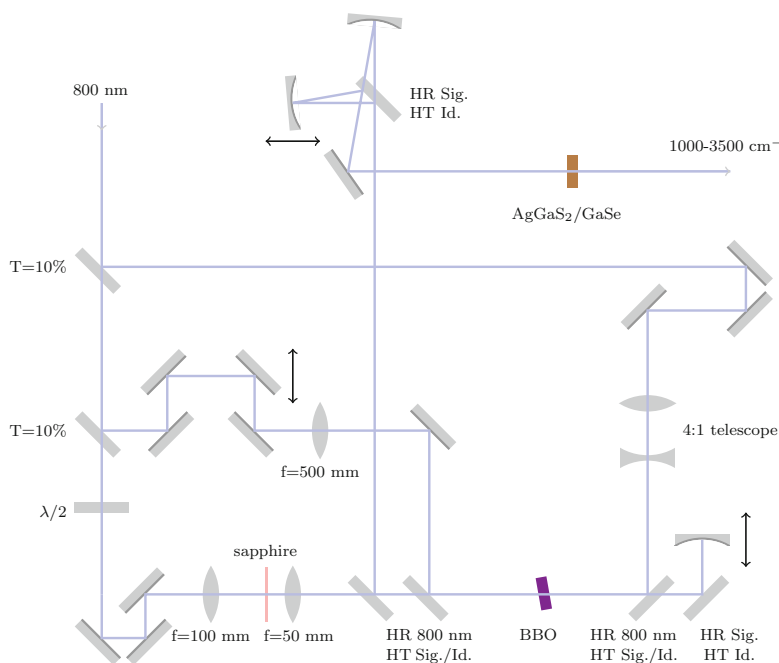


Fig. 2.8 Parametric frequency conversion for the generation of tuneable mid-infrared pulses. Weak signal and idler pulses with pulse energies $< 1 \mu\text{J}$ are generated by optical parametric amplification of a supercontinuum generated in a sapphire plate. Subsequently, the signal is recollimated and further amplified in a second pass through the amplification crystal. Difference frequency generation of signal and idler radiation with pulse energies in the range of $150 \mu\text{J}$ leads to mid-infrared pulses. Typical pulse energies exceed $2 \mu\text{J}$ and values of up to $7 \mu\text{J}$ are obtained with an optional third amplification for the signal radiation (not shown). Tuneability is achieved by changing the phase matching angle of the amplification crystal (BBO) and the difference frequency generation crystal (AgGaS_2 or GaSe). Abbreviations: T—transmission, HR/HT: dichroic mirrors optimized for high reflection/high transmission of different spectral components, Sig./Id.: signal and idler radiation with wavelengths between $1200\text{--}1600\text{nm}$ and $1600\text{--}2400\text{nm}$, respectively

Here $E_{pump,probe}$ and $I_{pump,probe}$ are the electric fields and intensities of the pump and probe pulses, respectively and τ is a tuneable time delay between them. The temporal width of $I_{XC}(\tau)$ is a measure of the time resolution in pump-probe experiments. Note that any phase information about the pulses is lost due to the functional form of Eq. 2.64. In some limits pulse durations can be extracted from such correlation techniques when the analytical form of the pulse envelope is known. For example, Fig. 2.9 shows a cross-correlation of pump and probe pulses with a frequency around 3000cm^{-1} together with a Gaussian fit of 110fs width (FWHM). Assuming that both pulses have the same spectral bandwidth and phase one extracts a pulse duration of $\approx 80\text{fs}$. However, more sophisticated methods are necessary to retrieve the full phase information without further assumptions.

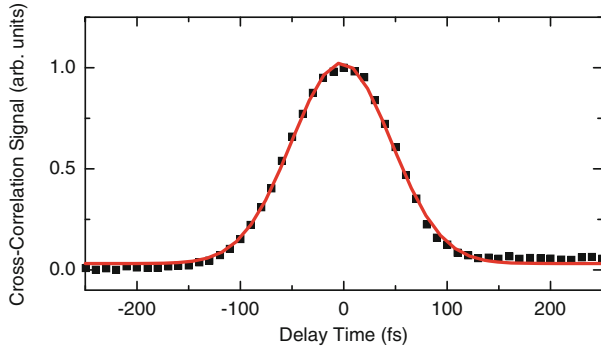


Fig. 2.9 Cross-correlation trace of pump and probe pulses centered around 3000 cm^{-1} (*squares*). The *red line* represents a Gaussian fit with a width of 110 fs (FWHM) (color figure online)

Frequency-resolved detection of auto-correlation or cross-correlation signals is an established technique well-known as frequency-resolved optical gating (FROG) [48]. Since the photon-echo setup (cf. Sect. 2.3.2) uses three pulses with independent delays in a boxcar geometry, a so-called transient grating (TG)-FROG is easily implemented. In such an arrangement, two pulses that are overlapped in space and time generate a refractive-index grating. A third pulse that is diffracted off that grating is independently delayed so that frequency-resolved and time-integrated detection leads to the TG-FROG signal:

$$I_{TG-FROG}(\omega, \tau) \propto \left| \int_{-\infty}^{\infty} E^2(t) E^*(t - \tau) e^{-i\omega t} dt \right|^2 \quad (2.65)$$

Iterative procedures are used to extract the electric field amplitude and phase of a pulse.

Another possibility is to measure a pulse phase by spectral interference with a frequency-shifted copy. This technique is referred to as spectral phase interferometry for direct electric-field reconstruction (SPIDER) [49]. A spectrometer measures the interference pattern:

$$I_{SPIDER}(\omega) = |E(\omega)|^2 + |E(\omega + \Omega)|^2 + 2 \cdot |E(\omega)| |E(\omega + \Omega)| \cos(\Phi(\omega + \Omega) - \Phi(\omega) + \omega\tau) \quad (2.66)$$

Here, $E(\omega)$ and $\Phi(\omega)$ are the spectral amplitude and phase of the electric field, Ω is the frequency shift and τ is the delay between the two pulses. $E(\omega)$ is easily obtained from the square root of the pulse spectrum so that the spectral phase can be retrieved non-iteratively by a Fourier analysis.

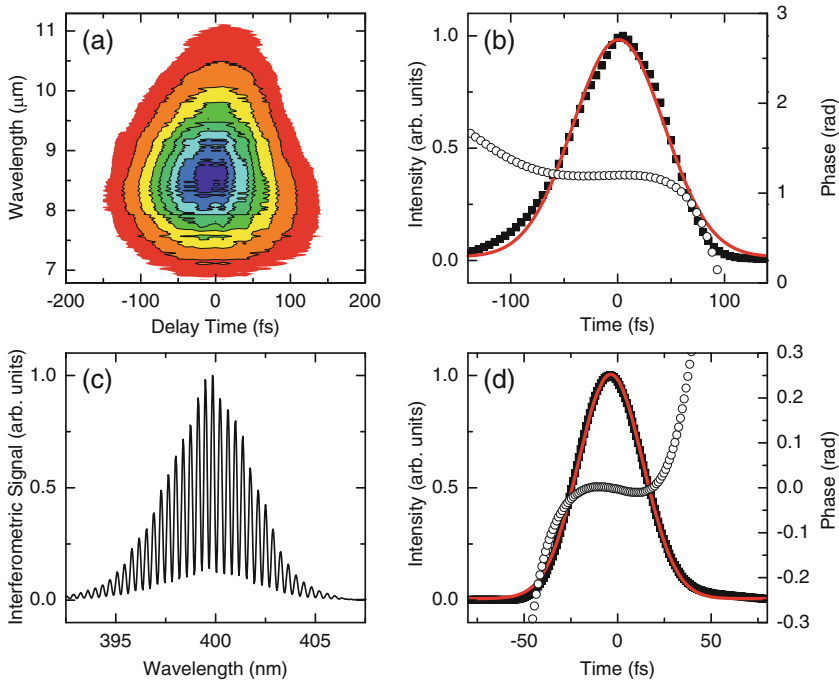


Fig. 2.10 **a** FROG trace of a pulse with a center wavelength between 8 and 9 μm that is used for photon-echo measurements in the phosphate stretching range as discussed in Sect. 3.1. **b** Retrieved intensity (*solid squares*) and phase profiles (*open circles*). A Gaussian fit (*red line*) indicates pulse durations of approximately 100 fs (FWHM). **c** SPIDER interferogram of a pulse from the amplified laser system used for the pump-probe experiments. The intensity and phase profiles for the retrieved ≈ 40 fs pulse are shown in **d** (color figure online)

Figure 2.10a, b display the FROG trace as well as the retrieved pulse used in a typical photon-echo measurement in the phosphate stretching range (cf. Sect. 3.1). Moderate distortions of the FROG trace point to slight residual third-order dispersion of the pulse. The envelope shows a width of 100 fs corresponding to about 3.6 cycles of the electric field. Pulse retrieval was facilitated by commercial software (FROG 3.2.2, Swamp Optics, LLC). For comparison, Fig. 2.10c, d show a SPIDER interferogram of a pulse derived from a typical amplified femtosecond laser system measured with a commercial LX-SPIDER (APE GmbH, [50]) and the corresponding retrieved pulse (pulse duration ≈ 40 fs).

It should be noted that none of the techniques described above is sensitive to the carrier-envelope phase, i.e., the relative phase between the oscillating electric field of a pulse and its envelope. Therefore, the task of field-resolved detection requires other methods such as free-space electro-optic sampling [51].

2.3.2 Passively Phase-Stabilized Heterodyne-Detected Photon Echo

2D IR spectroscopy can be performed by a variety of experimental setups. Pump-probe measurements with tuneable narrow-band pump pulses allow for a direct acquisition of 2D IR spectra in the frequency domain [52]. The drawback of limited (picosecond) time resolution is circumvented with coherent spectroscopy in the time domain by using three pulses with independent delays where the excitation-frequency axis is obtained by a numerical Fourier transform along the (first) coherence time delay. Using coherent techniques requires active or passive phase stabilization of the pulses involved. This task was achieved by different groups using either a non-collinear, a pump-probe or a collinear beam geometry [53–59].

Figure 2.11 shows the experimental implementation to measure 2D IR spectra used in this work based on the approach outlined in [53]. Mid-infrared pulses are split into two copies by the help of a beamsplitter. A translation stage in the beam path of one pulse allows for tuneability of the relative time delay Δt_1 . Focussing the two initially horizontally aligned pulses onto a horizontal reflective diffractive optic element (DOE) generates 4 pulses that define the corners of a rectangle (cf. Fig. 2.12a). For clarity, the four beam paths after diffraction are drawn as dashed

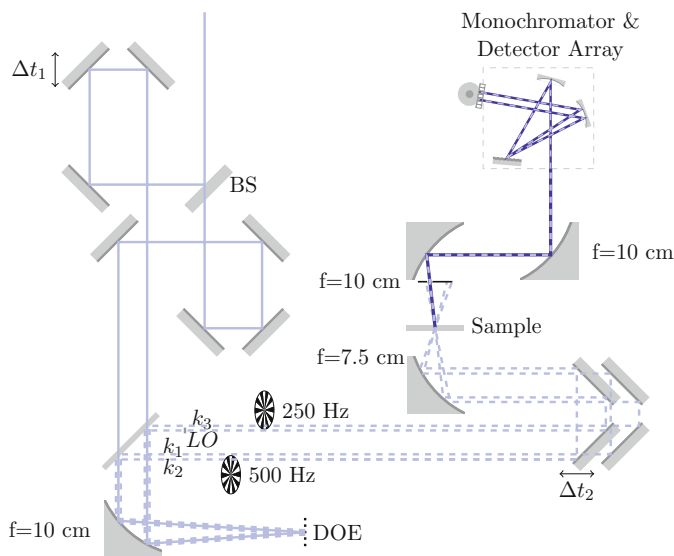
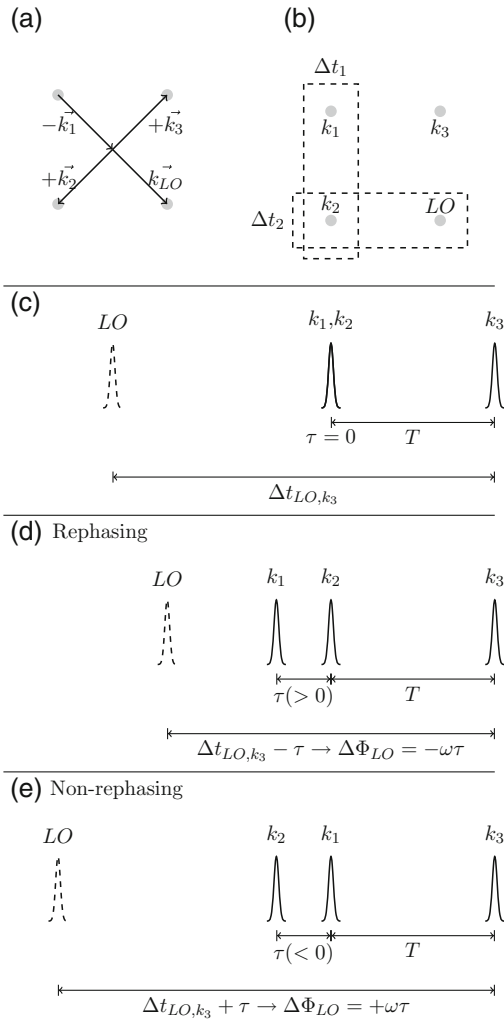


Fig. 2.11 Sketch of the photon-echo setup for measuring 2D IR spectra. Phase locked pairs of pulses are obtained by the use of a beamsplitter (BS) and a diffractive optic element (DOE). In this way, the third-order nonlinear signal (solid blue line) generated by k_1 , k_2 and k_3 is heterodyned with a local oscillator (LO) pulse and the resulting spectral interferogram is detected by a 64-pixel mercury cadmium telluride detector array. Translation stages allow for independent tuning of the two delay times between the signal-generating beams

Fig. 2.12 **a** Phase matching geometry used for photon echo experiments. The local oscillator is automatically aligned collinearly with the emitted third-order signal ($\vec{k}_{signal} = -\vec{k}_1 + \vec{k}_2 + \vec{k}_3 = \vec{k}_{LO}$). **b** Schematic plot of the correlated delays used in the experimental setup (Fig. 2.11). The second delay Δt_2 sets τ . The first delay Δt_1 corresponds to T only if $\tau < 0$ (k_2 precedes k_1). In case of $\tau > 0$, $\Delta t_1 = T - \tau$ so that the first delay has to correct for τ to ensure a constant T . **c–e** show the corresponding pulse sequences and the resulting variable time delay of the local oscillator that leads to measurements in the rotating frame with respect to the coherence time τ . For details see text



lines in Fig. 2.11. The lower two beams (k_2 , LO) experience a second time delay Δt_2 with respect to the upper ones (k_1 , k_3). After being focussed into the sample, k_1 , k_2 and k_3 generate a third-order nonlinear signal in the (rephasing) phase matching direction $\vec{k}_{signal} = -\vec{k}_1 + \vec{k}_2 + \vec{k}_3 = \vec{k}_{LO}$ so that the signal and local oscillator pulses propagate collinearly (cf. Fig. 2.12a). The focal spot size is about 100 and 200 μm at 3000 and 1250 cm^{-1} , respectively, and each pulse has an energy on the order of 1 μJ . In order to avoid signals generated by the local oscillator, it is attenuated by a copper mesh (OD = 2) and advanced in time by inserting 0.5 mm ZnSe into the k_3 beam path. The spectral interference pattern between the signal and local oscillator

$$I_{2DIR}(\omega_{Det}) = |E_{LO}(\omega_{Det}) + E_{signal}(\omega_{Det})|^2 \quad (2.67)$$

is then measured as a function of the detection frequency ω_{Det} with a monochromator and a 64-pixel mercury cadmium telluride (MCT) detector array. Here, E_{LO} and E_{signal} are the local oscillator and signal electric fields, respectively.

Assuming that the signal fields are small compared to the local oscillator one obtains:

$$I_{2DIR}(\omega_{Det}) = |E_{LO}(\omega_{Det})|^2 + 2\Re(E_{LO}^*(\omega_{Det})E_{signal}(\omega_{Det})) \\ |E_{LO}(\omega_{Det})|^2 + 2|E_{LO}(\omega_{Det})||E_{signal}(\omega_{Det})| \cdot \cos(\Phi_{signal} - \Phi_{LO}) \quad (2.68)$$

$|E_{LO}(\omega)|^2$ is the local oscillator spectrum. It is subtracted by chopping one of the signal generating beams at a 500Hz rate (here: k_2) and taking the differential signal between two consecutive pulses. In principle, a scattering contribution to the measured signal originating from scattering of the sample and the sample-cuvette windows cannot be excluded. This contribution is eliminated by an optional second chopper for k_3 running at 250Hz and thereby allowing for subtraction of the k_2 -scattering.

The phase difference in Eq. 2.68 can be written as

$$\Phi_{signal} - \Phi_{LO} = (-\Phi_1 + \Phi_2) + (\Phi_3 - \Phi_{LO}) + \phi_{signal} \\ = (-\Phi_1 + \Phi_3) + (\Phi_2 - \Phi_{LO}) + \phi_{signal} \quad (2.69)$$

where $\Phi_{1,2,3,LO}$ are the phases of k_1, k_2, k_3 and k_{LO} , respectively and ϕ_{signal} is the phase related to a system's nonlinear response function. An important consequence of using the DOE is that the setup is inherently phase stabilized because it produces phase locked pairs of pulses. Before the DOE, phase differences between k_1 and k_2 as well as k_3 and k_{LO} cancel out (cf. first line in Eq. 2.69). After the DOE, phase fluctuations cancel out because there are similar beam paths for the pairs (k_1, k_3) and (k_2, k_{LO}) (second line in Eq. 2.69).

Note that E_{signal} and I_{2DIR} intrinsically carry a time-dependence with respect to Δt_1 and Δt_2 . As depicted in Fig. 2.12b, the first delay moves (k_1, k_2) with respect to (k_3, k_{LO}) whereas the second moves (k_2, k_{LO}) with respect to (k_1, k_3) . Δt_2 moves are directly connected to the coherence time τ . Positive values of τ scan the rephasing signal contributions. $\tau < 0$ corresponds to a change of the (k_1, k_2) time-ordering so that the non-rephasing signal is measured as a function of $-\tau$. For the non-rephasing diagrams, Δt_1 defines the population time T . Since Δt_2 moves k_2 relative to k_3 , Δt_1 has to be moved accordingly to ensure a constant population time T for the rephasing diagrams.

An interesting consequence of the correlated time delays is that the local oscillator moves in time as a function of τ (Fig. 2.12c–e). While the relative phase shift for rephasing diagrams (Fig. 2.12d) equals $-\omega\tau$ because the local oscillator approaches k_3 , a relative phase shift of $+\omega\tau$ occurs for the non-rephasing diagrams when the local oscillator is shifted away from k_3 . Consequently, the τ -dependence in the third-order response functions (Eqs. 2.55, 2.56) cancels out so that the spectral interferogram is

free from oscillations in τ . This is equivalent to projecting the 2D spectrum onto $\nu_1 = 0$. Correct spectra are obtained by multiplying the proper phase factors in the analysis procedure. The advantage over a fixed $k_3 - k_{LO}$ time difference is that according to the Nyquist-Shannon sampling theorem [60], the coherence time step determines the ν_1 width of the 2D spectrum rather than its maximum ν_1 value. Therefore, the measurement times are greatly reduced by choosing appropriate coherence time steps.

In order to compute a 2D spectrum, the signal amplitude and phase of one data set containing a full τ -scan at a defined population time T are extracted by a Fourier analysis that is described in detail elsewhere [61–63]. Briefly, the signal is first Fourier-transformed along ω_{Det} into the time domain. Only the positive time components are chosen by a supergaussian filter function for causality reasons. After transforming the signal back to the spectral domain, the local oscillator field amplitude is divided out. 2D spectra are obtained by a Fourier transform along the coherence time axis. For proper extraction of the signals, the relative phase between the signal and the local oscillator have to be known exactly. In a phasing procedure, the 2D spectrum integrated along the excitation-frequency axis is compared to a pump-probe spectrum measured at the same population time. The spectral interferogram is then multiplied with a constant phase and two linear phase terms that take into account the uncertainty of relative timing between k_1 and k_2 as well as k_3 and k_{LO} . Changing the phase parameters leads to proper phasing that is assumed to be achieved when the integrated 2D spectrum fits the pump-probe spectrum [30].

2.3.3 Two-Color Pump-Probe Setup

Figure 2.13 depicts the setup to perform two-color pump-probe measurements. Two independently tunable OPAs (Sect. 2.3.1) serve as sources for pump and probe pulses. The pump-probe delay time corresponding to the population time T is introduced by a mechanical delay stage in the pump arm. Probe pulses from the OPA are attenuated and split into a probe and a reference by taking the front- and backsurface-reflection of a BaF₂ wedge. Pump and probe pulses with pulse energies of about 2 μ J and a few tens of nJ, respectively, are focussed into the same spot in the sample by 30° off-axis parabolic mirrors (spot size $\approx 100 \mu\text{m}$). The probing of homogeneously excited sample volumes is realized by tighter focussing of the probe beam. In practice, increasing the probe beam waist with a telescope before focussing leads to smaller spot sizes in the sample. The reference pulse is transmitted through the sample at a different position. After the sample interaction the probe beam is dispersed by a monochromator and detected with a 64-pixel MCT array. Chopping the pump beam at 500 Hz and using the reference pulse for correction of probe-pulse intensity fluctuations, we calculate the transient absorbance change ΔA as a function of the delay time T and the probe frequency ν_{Pr} (equivalent to the detection frequency of 2D spectra):

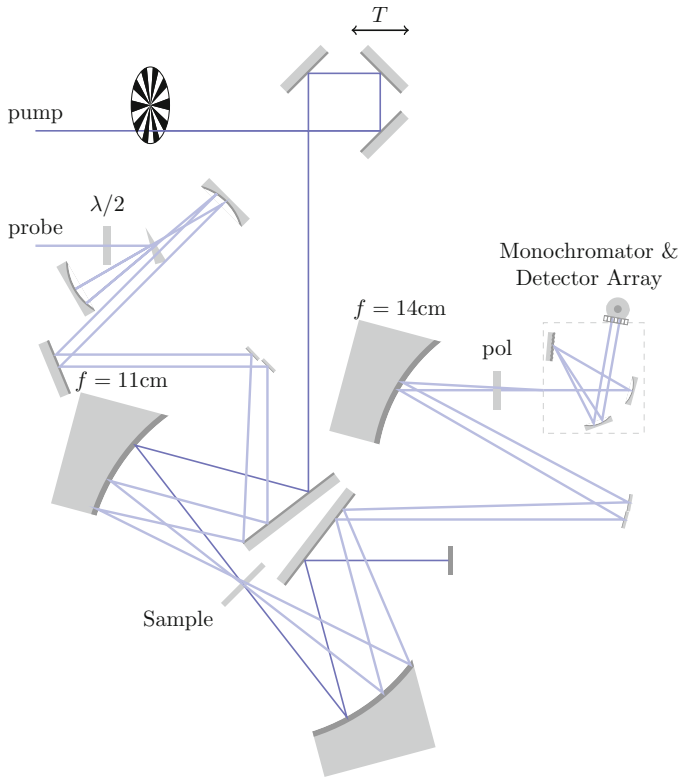


Fig. 2.13 Sketch of the two-color pump-probe setup. Pump and probe pulses are generated in two independently tuneable OPAs. A translation stage in the pump beam path allows for control of the pump-probe delay T . Probe and reference pulses are obtained by taking the reflection of two sides of a BaF₂ wedge. Spectrally-resolved pump-induced absorbance changes are measured by overlapping probe pulses with chopped pump pulses (500Hz) in the same spot of the sample and detecting the probe with a monochromator and 64-pixel MCT array. A second array measures the reference pulse intensities (without pump overlap) simultaneously in order to correct for intensity fluctuations. For polarization-resolved measurements, the probe is polarized under a 45° angle with respect to the pump by a half-wave plate ($\lambda/2$). A polarizer (pol) then allows for detecting absorbance changes with arbitrary relative polarization compared to the pump pulses

$$\Delta A(T, \nu_{Pr}) = -\log \left(\frac{I_{pump}^{(probe)}(T, \nu_{Pr})}{I_0^{(probe)}(T, \nu_{Pr})} \cdot \frac{I_0^{(reference)}(T, \nu_{Pr})}{I_{pump}^{(reference)}(T, \nu_{Pr})} \right) \quad (2.70)$$

Here the subscripts *pump* and 0 indicate intensities with and without pump excitation, and the superscripts denote intensities from the probe and the reference, respectively. Equation 2.70 is evaluated on a shot-to-shot basis to avoid contributions from pulse energy fluctuations.

In single-color measurements, significant interference fringes due to scattering of the pump beam can occur. Those signals cannot be eliminated in the same way as in the 2D IR setup. Instead, moving the pump-probe delay in fractions of the wavelength and averaging over an oscillation period helps to suppress interferences. Since the wavelength of the pulses used in this thesis is $<10\mu\text{m}$, the reduction in time resolution ($<33\text{ fs}$) is negligible.

Polarization-resolved measurements are performed by inserting a half-wave plate into the probe beam path and thereby polarizing the probe under a 45° angle with respect to the pump. Polarization analysis of the emitted signal is the basis for a construction of the pump-probe anisotropy (cf. Eq. 2.62):

$$r(T) = \frac{\Delta A_{\parallel}(T) - \Delta A_{\perp}(T)}{\Delta A_{\parallel}(T) + 2 \cdot \Delta A_{\perp}(T)} \quad (2.71)$$

Absorbance changes parallel $\Delta A_{\parallel}(T)$ and perpendicular $\Delta A_{\perp}(T)$ to the pump polarization are selected with a polarizer after the sample interaction.

The experimental setup is placed in a sealed box that can be purged with nitrogen to prevent infrared absorption by water vapor or carbon dioxide in air (cf. Fig. 2.2a, green line).

2.3.4 Phospholipid Reverse Micelles

The central focus of this thesis are phospholipid reverse micelles made of 1,2-dioleoyl-sn-glycero-3-phosphocholine (DOPC) as depicted in Fig. 2.14 for the study of phosphate-water interactions and structural fluctuations of confined water on ultra-fast time scales. However, such aggregates can also be formed by other surfactants. In fact, the molecule investigated most extensively is dioctyl sodium sulfosuccinate (aerosol OT, AOT, cf. Fig. 2.14) [64] that was initially synthesized as a wetting agent to reduce the surface tension of water e.g., for the use as washing powder or modification of the floating properties of swimming objects [65, 66]. Reverse micelles are ideal tools to embed nanoscopic water pools in nonpolar solvents with the water content determining their size [67, 68]. Therefore, an important parameter to characterize such systems is the relative water concentration

$$w_0 = \frac{[\text{water}]}{[\text{surfactant}]} \quad (2.72)$$

where the brackets indicate molar concentrations. It has been shown for AOT [69, 70] that the reverse-micelle diameter d_{RM} scales linearly with w_0 up to a value of $w_0 = 30$:

$$d_{RM} = cw_0 + d_0 \quad (2.73)$$

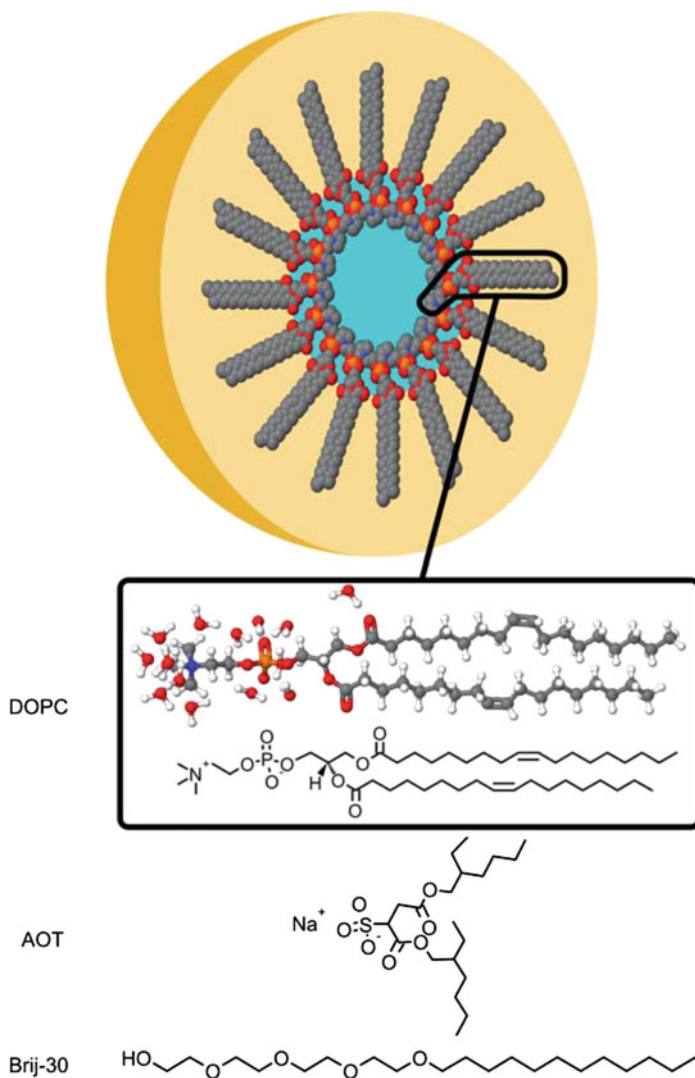


Fig. 2.14 Experimental System. *Top* Schematic of a dioleoylphosphatidylcholine (DOPC) reverse micelle in a nonpolar medium (benzene, *yellow*). Phospholipid head groups interact with nanoscopic water pools (*blue*) in a way described in Sect. 1.1. A single DOPC molecule is highlighted and the alignment of water molecules in the head-group potential is depicted in a ball and stick model. *Bottom* Molecular structures of the ionic AOT and non-ionic Brij-30 surfactants used as reference systems

Here d_0 represents the diameter without water roughly corresponding to twice the length of an AOT molecule and the constant $c = 0.3$ nm reflects growing water pools in the reverse micelle's interior as w_0 is increased. At a low water concentration, H_2O

molecules interact with the charged interface and are highly immobilized compared to bulk water whose behavior is approached by increasing the value of w_0 [71–73]. AOT is the workhorse of reverse-micelle studies [74, 75] but it has also been shown that different phospholipids self-assemble into reverse-micelle structures [76].

For the preparation of phospholipid reverse micelles used in the time-resolved experiments presented in Chaps. 3 and 4, DOPC was dissolved in benzene with a concentration of 0.25 M. Appropriate amounts of water were added in order to obtain samples in a wide range of hydration between $w_0 = 1$ and 16. Dynamic light scattering of solutions at $w_0 = 5$ and 16.5 indicate reverse-micelle diameters of (4.65 ± 0.15) and (7.9 ± 0.5) nm, respectively. Assuming a linear relationship as in Eq. 2.73 we extract $c = (0.30 \pm 0.02)$ nm and $d_0 = (3.2 \pm 0.2)$ nm, i.e., the growth of DOPC reverse micelles with w_0 is similar to the well-known AOT case. The value of d_0 agrees reasonably with the 3.6 nm thickness of fully hydrated DOPC bilayers [77]. Values for reverse micelle diameters in the hydration range of $w_0 = 1 - 16$ used for the time-resolved experiments in this work vary between 3.5 and 8 nm (cf. Table 2.1). The number of DOPC molecules per reverse micelle varies between 60–300. This parameter is determined by the ratio of the reverse-micelle surface area and the area of a DOPC molecule which is assumed to increase linearly with w_0 between 0.6 and 0.7 nm² according to the results obtained by phospholipid hydration. The water pool size increases from ≈ 60 ($w_0 = 1$) to 4600 ($w_0 = 16$) H₂O molecules. Increasing reverse micelle volumes (V_{RM}) lead to decreasing reverse micelle concentrations and therefore a larger space that a single reverse micelle can take up (V_{space}). Table 2.1 lists these parameters as a function of w_0 suggesting that the sample may be thought of as mainly non-interacting particles at the DOPC concentration used in the experiments.

While the hydration structure of phospholipids in aqueous solution is well characterized, less is known about water structure in reverse-micellar systems. However, it is conceivable that the main characteristics of the lipid head-group organization and hydration structure in these systems, i.e., the hydration sites, hydrogen-bond strengths and the occurrence of inter- and intramolecular charge pairs, are comparable. The typical behavior of water in confinement was found for phospholipid reverse

Table 2.1 Parameters of the DOPC reverse-micelle system at a concentration of 0.25 M in benzene as a function of hydration (w_0): diameter (d_{RM} , Eq. 2.73), number (#) of DOPC and water molecules per reverse micelle, volume of a reverse micelle (V_{RM}) and the average free volume determined from the reverse-micelle concentration (V_{space})

w_0	d_{RM} (nm)	# DOPC	# H ₂ O	V_{RM} (nm ³)	V_{space} (nm ³)
1	3.5	64	64	22	428
3	4.1	86	258	36	574
5	4.7	111	554	54	738
8	5.6	152	1219	92	1016
16	8.0	287	4596	268	1915

micelles [78, 79], i.e., immobilized water interacting with the lipid head groups at low hydration levels and a buildup of bulk-like water pools after full hydration of the phospholipid head groups ($w_0 > 6-8$).

Most of this thesis deals with ultrafast dynamics inside DOPC reverse micelles. However, it is sometimes instructive to compare the results to systems containing different surfactant molecules (cf. Fig. 2.14, bottom). The permanent charges of ionic surfactants cause electrostatic potentials in which water molecules align as described in Sect. 1.1. As a result, interface-bound water experiences a markedly different environment compared to the bulk that affects intermolecular vibrations such as librations, i.e., hindered rotations.

An important difference between DOPC and AOT is the configuration of the head group. DOPC has a zwitterionic structure where the N^+ counterion is an integrated part of the phospholipid molecule whereas the Na^+ counterions of AOT are free. Therefore, the DOPC head-group volume is significantly larger than the one of AOT. Indeed, solvation dynamics suggest that water reorientation in lecithin reverse micelles is more restricted than for AOT at similar hydration levels due to the higher amount of water accepted by the lecithin interface [80]. Moreover, hydrogen bonds of water interacting with AOT head groups were found to be weaker than bulk-water hydrogen bonds [81] in contrast to the stronger hydrogen bonds at phospholipid interfaces.

The effect of charged head groups may be independently tested by non-ionic surfactants with head groups consisting of polyoxyethylenes and a glycol group such as glycol dodecyl ether (Brij-30, Fig. 2.14). While non-ionic reverse micelles are significantly less studied than their ionic counterparts, it is known that water forms pools inside Brij-30 reverse micelles [82, 83]. A non-uniform water distribution in the Brij-30 micelle core was found with only little penetration into the polyoxyethylene-chain region and increased water mobility compared to anionic reverse micelles.

References

1. M. Born, R. Oppenheimer, Zur Quantentheorie der Molekeln. German. Ann. Phys. **389**, 457–484 (1927)
2. G. Herzberg, *Molecular Spectra and Molecular Structure I Spectra of Diatomic Molecules* (D. Van Nostrand Company Inc, New York, 1950)
3. G. Herzberg, *Molecular Spectra and Molecular Structure II Infrared and Raman Spectra of Polyatomic Molecules* (Krieger Publishing Company, Malabar, 1991)
4. P. Hamm, M. Zanni, *Concepts and Methods of 2D Infrared Spectroscopy* (Cambridge University Press, Cambridge, 2011)
5. L. Pauling, E.B. Wilson, *Introduction to Quantum Mechanics* (McGraw-Hill Book Company, Inc., New York, 1935)
6. E. Schrödinger, Quantisierung als Eigenwertproblem. German. Ann. Phys. **384**, 489–527 (1926)
7. E. Fermi, Über den Ramaneffekt des Kohlendioxyds. German. Z. Phys. **71**, 250–259 (1931)
8. C.V. Raman, The molecular scattering of light. Nobel Lecture (1930)
9. B.S. Hudson, Vibrational spectroscopy using inelastic neutron scattering: overview and outlook. Vib. Spectrosc. **42**, 25–32 (2006)

10. R.G. Gordon, Correlation functions for molecular motion. *Adv. Magn. Reson.* **3**, 1–42 (1968)
11. P.W. Anderson, P.R. Weiss, Exchange narrowing in paramagnetic resonance. *Rev. Mod. Phys.* **25**, 269–276 (1953)
12. R. Kubo, A stochastic theory of line-shape and relaxation, in *Fluctuation, Relaxation and Resonance in Magnetic Systems*, ed. by D. ter Haar (Oliver & Boyd, Edinburgh, 1962)
13. R. Kubo, A stochastic theory of lineshape. *Adv. Chem. Phys.* **15**, 101–127 (1969)
14. W.G. Rothschild, Motional characteristics of large molecules from their Raman and infrared band contours: vibrational dephasing. *J. Chem. Phys.* **65**, 455–462 (1976)
15. N. Bloembergen, E.M. Purcell, R.V. Pound, Relaxation effects in nuclear magnetic resonance absorption. *Phys. Rev.* **73**, 679–712 (1948)
16. P.A.M. Dirac, The quantum theory of the emission and absorption of radiation. *Proc. R. Soc. Lond., Ser. A* **114**, 243–265 (1927)
17. D.W. Oxtoby, Vibrational population relaxation in liquids. *Adv. Chem. Phys.* **47**, 487–519 (1981)
18. B.J. Berne, Time-dependent properties of condensed media, in *Physical Chemistry: An Advanced Treatise*, vol. 8B, ed. by D. Henderson (Academic, New York, 1971), pp. 540–713
19. J.S. Bader, B.J. Berne, Quantum and classical relaxation rates from classical simulations. *J. Chem. Phys.* **100**, 8359–8366 (1994)
20. J.L. Skinner, Semiclassical approximations to golden rule rate constants. *J. Chem. Phys.* **107**, 8717–8718 (1997)
21. W.S. Benedict, E.K. Plyler, Absorption spectra of water vapor and carbon dioxide in the region of 2.7 microns. *J. Res. Natl. Bur. Stand.* **46**, 246–259 (1951)
22. A. Novak, Hydrogen bonding in solids correlation of spectroscopic and crystallographic data, *Large Molecules*, vol. 18, Structure and Bonding (Springer, Berlin, 1974), pp. 177–216
23. C.M. Huggins, G.C. Pimentel, Systematics of the infrared spectral properties of hydrogen bonding systems: frequency shift, half width and intensity. *J. Phys. Chem.* **60**, 1615–1619 (1956)
24. S. Mukamel, *Principles of Nonlinear Optical Spectroscopy* (Oxford University Press, Oxford, 1995)
25. M. Cho, *Two-dimensional Optical Spectroscopy* (CRC Press, Taylor & Francis Group, Boca Raton, 2009)
26. R.W. Boyd, *Nonlinear Optics*, 3rd edn. (Elsevier, 2008)
27. M.D. Fayer, Dynamics of molecules in condensed phases: Picosecond holographic grating experiments. *Annu. Rev. Phys. Chem.* **33**, 63–87 (1982)
28. K. Duppen, D.A. Wiersma, Picosecond multiple-pulse experiments involving spatial and frequency gratings: a unifying nonperturbational approach. *J. Opt. Soc. Am. B* **3**, 614–621 (1986)
29. S.A. Corcelli, J.L. Skinner, Infrared and Raman line shapes of dilute HOD in liquid H₂O and D₂O from 10 to 90°C. *J. Phys. Chem. A* **109**, 6154–6165 (2005)
30. S.M. Gallagher Faeder, D.M. Jonas, Two-dimensional electronic correlation and relaxation spectra: Theory and model calculations. *J. Phys. Chem. A* **103**, 10489–10505 (1999)
31. M. Khalil, N. Demirdöven, A. Tokmakoff, Obtaining absorptive line shapes in two-dimensional infrared vibrational correlation spectra. *Phys. Rev. Lett.* **90**, 047401 (2003)
32. K. Okumura, A. Tokmakoff, Y. Tanimura, Two-dimensional line-shape analysis of photon-echo signal. *Chem. Phys. Lett.* **314**, 488–495 (1999)
33. A. Tokmakoff, Two-dimensional line shapes derived from coherent third-order nonlinear spectroscopy. *J. Phys. Chem. A* **104**, 4247–4255 (2000)
34. K. Kwak, S. Park, I.J. Finkelstein, M.D. Fayer, Frequency-frequency correlation functions and apodization in two-dimensional infrared vibrational echo spectroscopy: a new approach. *J. Chem. Phys.* **127**, 124503 (2007)
35. K. Lazonder, M.S. Pshenichnikov, D.A. Wiersma, Easy interpretation of optical two-dimensional correlation spectra. *Opt. Lett.* **31**, 3354–3356 (2006)
36. K. Kwak, M. Cho, Two-color pump-probe spectroscopies of two- and three-level systems: 2-dimensional line shapes and solvation dynamics. *J. Phys. Chem. A* **107**, 5903–5912 (2003)

37. G. Stirnemann, J.T. Hynes, D. Laage, Water hydrogen bond dynamics in aqueous solutions of amphiphiles. *J. Phys. Chem. B* **114**, 3052–3059 (2010)
38. A. Ghosh, R.M. Hochstrasser, A peptide's perspective of water dynamics. *Chem. Phys.* **390**, 1–13 (2011)
39. M. Khalil, A. Tokmakoff, Signatures of vibrational interactions in coherent two-dimensional infrared spectroscopy. *Chem. Phys.* **266**, 213–230 (2001)
40. S. Woutersen, P. Hamm, Nonlinear two-dimensional vibrational spectroscopy of peptides. *J. Phys.: Condens. Matter* **14**, R1035–R1062 (2002)
41. M. Chachisvilis, H. Fidder, V. Sundström, Electronic coherence in pseudo twocolour pump-probe spectroscopy. *Chem. Phys. Lett.* **234**, 141–150 (1995)
42. T. Tao, Time-dependent fluorescence depolarization and Brownian rotational diffusion coefficients of macromolecules. *Biopolymers* **8**, 609–632 (1969)
43. G.R. Fleming, J.M. Morris, G.W. Robinson, Direct observation of rotational diffusion by picosecond spectroscopy. *Chem. Phys.* **17**, 91–100 (1976)
44. H. Graener, G. Seifert, A. Laubereau, Direct observation of rotational relaxation times by time-resolved infrared spectroscopy. *Chem. Phys. Lett.* **172**, 435–439 (1990)
45. P.F. Moulton, Spectroscopic and laser characteristics of Ti:Al₂O₃. *J. Opt. Soc. Am. B* **3**, 125–133 (1986)
46. R.A. Kaindl, M. Wurm, K. Reimann, P. Hamm, A.M. Weiner, M. Woerner, Generation, shaping, and characterization of intense femtosecond pulses tunable from 3 to 20 μm . *J. Opt. Soc. Am. B* **17**, 2086–2094 (2000)
47. R. Trebino, *Frequency-resolved Optical Gating: The Measurement of Ultrashort Laser Pulses* (Kluwer Academic, Boston, 2000)
48. R. Trebino, K.W. DeLong, D.N. Fittinghoff, J.N. Sweetser, M.A. Krumbügel, B.A. Richman, D.J. Kane, Measuring ultrashort laser pulses in the timefrequency domain using frequency-resolved optical gating. *Rev. Sci. Instrum.* **68**, 3277–3295 (1997)
49. C. Iaconis, I.A. Walmsley, Spectral phase interferometry for direct electric-field reconstruction of ultrashort optical pulses. *Opt. Lett.* **23**, 792–794 (1998)
50. G. Stibenz, P. Staudt, C. Lukas, S.-P. Gorza, and I. A. Walmsley, Fully automated, phase corrected long crystal SPIDER for the characterization of broadband pulses, in *Conference on Lasers and Electro-Optics/Quantum Electronics and Laser Science Conference and Photonic Applications Systems Technologies* (2008)
51. Q. Wu, X.-C. Zhang, Free-space electro-optic sampling of terahertz beams. *Appl. Phys. Lett.* **67**, 3523–3525 (1995)
52. P. Hamm, M. Lim, R.M. Hochstrasser, Structure of the amide I band of peptides measured by femtosecond nonlinear-infrared spectroscopy. *J. Phys. Chem. B* **102**, 6123–6138 (1998)
53. M.L. Cowan, J.P. Ogilvie, R.J.D. Miller, Two-dimensional spectroscopy using diffractive optics based phased-locked photon echoes. *Chem. Phys. Lett.* **386**, 184–189 (2004)
54. T. Brixner, T. Mančal, I.V. Stiopkin, G.R. Fleming, Phase-stabilized twodimensional electronic spectroscopy. *J. Chem. Phys.* **121**, 4221–4236 (2004)
55. V. Volkov, R. Schanz, P. Hamm, Active phase stabilization in Fourier-transform two-dimensional infrared spectroscopy. *Opt. Lett.* **30**, 2010–2012 (2005)
56. L.P. DeFlores, R.A. Nicodemus, A. Tokmakoff, Two-dimensional Fourier transform spectroscopy in the pump-probe geometry. *Opt. Lett.* **32**, 2966–2968 (2007)
57. J. Helbing, P. Hamm, Compact implementation of Fourier transform twodimensional IR spectroscopy without phase ambiguity. *J. Opt. Soc. Am. B* **28**, 171–178 (2011)
58. S.-H. Shim, M.T. Zanni, How to turn your pump-probe instrument into a multidimensional spectrometer: 2D IR and Vis spectroscopies via pulse shaping. *Phys. Chem. Chem. Phys.* **11**, 748–761 (2009)
59. W. Kuehn, K. Reimann, M. Woerner, T. Elsaesser, R. Hey, Two-dimensional terahertz correlation spectra of electronic excitations in semiconductor quantum wells. *J. Phys. Chem. B* **115**, 5448–5455 (2011)
60. C.E. Shannon, Communication in the presence of noise. *Proc. IEEE* **37**, 10–21 (1949)

61. L. Lepetit, G. Chériaux, M. Joffre, Linear techniques of phase measurement by femtosecond spectral interferometry for applications in spectroscopy. *J. Opt. Soc. Am. B* **12**, 2467–2474 (1995)
62. N. Huse, Multidimensional vibrational spectroscopy of hydrogen-bonded systems in the liquid phase: Coupling mechanisms and structural dynamics. Ph.D. thesis. Humboldt Universität zu Berlin, 2006
63. M. Yang, Ultrafast two-dimensional infrared spectroscopy of hydrogen-bonded base pairs and hydrated DNA. Ph.D. thesis. Humboldt Universität zu Berlin, 2012
64. T.K. De, A. Maitra, Solution behaviour of Aerosol OT in non-polar solvents. *Adv. Colloid Interface Sci.* **59**, 95–193 (1995)
65. C.R. Caryl, Sulfosuccinic esters. Structure and wetting power. *Ind. Eng. Chem.* **33**, 731–737 (1941)
66. C.R. Caryl, W.P. Ericks, Esters of sodium sulfosuccinic acid. *Ind. Eng. Chem.* **31**, 44–47 (1939)
67. R.W. Mattoon, M.B. Mathews, Micelles in non-aqueous media. *J. Chem. Phys.* **17**, 496–497 (1949)
68. M.B. Mathews, E. Hirschhorn, Solubilization and micelle formation in a hydrocarbon medium. *J. Colloid Sci.* **8**, 86–96 (1953)
69. M. Zulauf, H.F. Eicke, Inverted micelles and microemulsions in the ternary system water/Aerosol-OT/isooctane as studied by photon correlation spectroscopy. *J. Phys. Chem.* **83**, 480–486 (1979)
70. M.-P. Pileni, T. Zemb, C. Petit, Solubilization by reverse micelles: solute localization and structure perturbation. *Chem. Phys. Lett.* **118**, 414–420 (1985)
71. M. Wong, J.K. Thomas, T. Nowak, Structure and state of water in reversed micelles. *J. Am. Chem. Soc.* **99**, 4730–4736 (1977)
72. R.E. Riter, D.M. Willard, N.E. Levinger, Water immobilization at surfactant interfaces in reverse micelles. *J. Phys. Chem. B* **102**, 2705–2714 (1998)
73. J. Faeder, B.M. Ladanyi, Molecular dynamics simulations of the interior of aqueous reverse micelles. *J. Phys. Chem. B* **104**, 1033–1046 (2000)
74. P.L. Luisi, M. Giomini, M.P. Pileni, B.H. Robinson, Reverse micelles as hosts for proteins and small molecules. *Biochim. Biophys. Acta, Rev. Biomembr.* **947**, 209–246 (1988)
75. M.P. Pileni, Reverse micelles as microreactors. *J. Phys. Chem.* **97**, 6961–6973 (1993)
76. P. Walde, A.M. Giuliani, C.A. Boicelli, P.L. Luisi, Phospholipid-based reverse micelles. *Chem. Phys. Lipids* **53**, 265–288 (1990)
77. N. Kučerka, S. Tristram-Nagle, J.F. Nagle, Structure of fully hydrated fluid phase lipid bilayers with monounsaturated chains. *J. Membr. Biol.* **208**, 193–202 (2006)
78. C.A. Boicelli, M. Giomini, A.M. Giuliani, Infrared characterization of different water types inside reverse micelles. *Appl. Spectrosc.* **38**, 537–539 (1984)
79. V.V. Kumar, P. Raghunathan, Proton NMR studies of the interaction of water with lecithin in non-polar organic media. *Chem. Phys. Lipids* **41**, 159–171 (1986)
80. D.M. Willard, R.E. Riter, N.E. Levinger, Dynamics of polar solvation in lecithin/water/cyclohexane reverse micelles. *J. Am. Chem. Soc.* **120**, 4151–4160 (1998)
81. G. Onori, A. Santucci, IR investigations of water structure in Aerosol OT reverse micellar aggregates. *J. Phys. Chem.* **97**, 5430–5434 (1993)
82. H. Caldararu, A. Caragheorghopol, M. Vasilescu, I. Dragutan, H. Lemmetyinen, Structure of the polar core in reverse micelles of nonionic poly(oxyethylene) surfactants, as studied by spin probe and fluorescence probe techniques. *J. Phys. Chem.* **98**, 5320–5331 (1994)
83. D. Pant, N.E. Levinger, Polar solvation dynamics in nonionic reverse micelles and model polymer solutions. *Langmuir* **16**, 10123–10130 (2000)

Chapter 3

Ultrafast Vibrational Dynamics of Phospholipid Hydration Sites

Time-averaged structures of self-assembled phospholipids are well known, whereas time-resolved information about lipid-lipid and lipid-water interactions is mostly deduced from MD simulations and—to some extent—from NMR measurements (cf. Sect. 1.1). Vibrational dynamics of phosphate vibrations in phospholipids have remained unexplored. Slightly more is known about phospholipid hydration-shell vibrational dynamics and a review is given in Chap. 4.

Figure 3.1 shows linear absorption spectra of DOPC reverse micelles at different hydration levels (w_0) between 950 and 1300 cm^{-1} . The assignment to different vibrations of the head group has been reported in the literature [1–3]: The symmetric $\nu_S(\text{PO}_2^-)$ and antisymmetric $\nu_{AS}(\text{PO}_2^-)$ stretching vibration of the non-ester phosphate oxygens is found at 1090 and 1250 cm^{-1} , respectively. Such vibrations involve the two phosphate oxygens that participate in hydrogen bonding with the phospholipid hydration shell and therefore represent interfacial probes for phosphate-water interactions. The pronounced redshift of both vibrations upon hydration illustrates their sensitivity to hydrogen bonding. In contrast, no such hydration dependence is found for the CO-O-C glycerol ester stretching vibrations at 1065 and 1175 cm^{-1} . A shoulder at 1050 cm^{-1} indicates the presence of the C-O-P in-chain phosphate stretching vibration. Although water does not form hydrogen bonds to the choline group, the antisymmetric choline stretching vibration at 970 cm^{-1} is found to blue-shift with increasing w_0 . A broad librational background of hydration-shell water occurs throughout the whole spectral range at high hydration levels. The strong absorption band at $\approx 1035\text{ cm}^{-1}$ is caused by the in-plane CH bending mode of the benzene solvent [4]. As pointed out before, water also forms hydrogen bonds to carbonyl groups exhibiting the characteristic carbonyl stretching mode at 1740 cm^{-1} (cf. Figs. 2.2 and 3.13).

So far, the carbonyl stretching vibration is the only phospholipid marker mode used in time-resolved vibrational spectroscopy. Spectral hole-burning (2D IR) with picosecond pulses in conjunction with MD simulations reveal that the inhomogeneity of carbonyl stretching bands is caused by strong electrostatic interactions between phospholipid head groups [5]. However, the time scales of structural fluctuations of the head groups or water-lipid hydrogen-bond lifetimes have remained unclear.

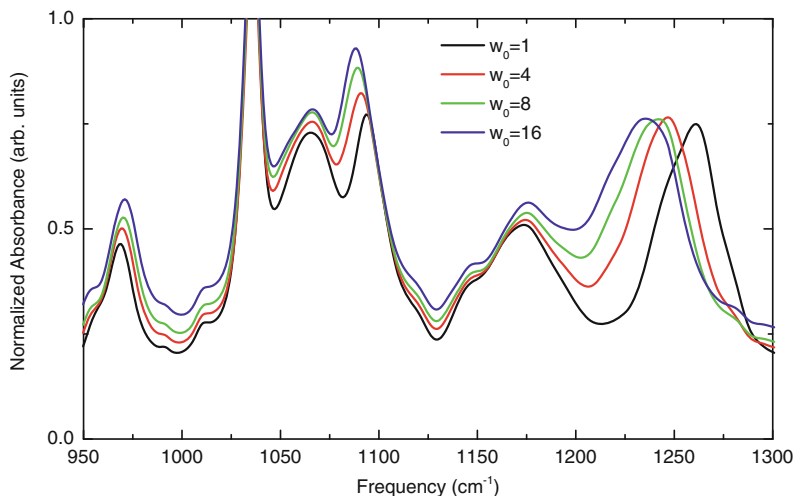


Fig. 3.1 Linear absorption spectra of DOPC reverse micelles in the head-group frequency range. The absorption bands at around 1090 and 1250 cm^{-1} are assigned to the symmetric and antisymmetric phosphate stretching vibration and shift as a function of hydration. Symmetric and antisymmetric glycerol ester stretching vibrations (CO-O-C) are found at 1065 and 1175 cm^{-1} . There is an overlap with the band at 1050 cm^{-1} from the in-chain C-O-P stretching vibration of the phosphate group. The hydration-dependent choline antisymmetric stretching vibration is found at 970 cm^{-1} .

Time-resolved IR data in the spectral range of Fig. 3.1 are limited to a single pump-probe study of the antisymmetric stretching mode of phosphates in the DNA backbone [6] suggesting water to act as a heat sink for phosphate excitations. This chapter describes the investigation of the vibrational dynamics of phosphate stretching vibrations in DOPC reverse micelles. A 2D lineshape analysis reveals the fluctuating nature of phospholipid head groups on a fast 300 fs time scale. Energy relaxation as well as its effect on the phosphate-water hydrogen-bond structure will be discussed and compared to the carbonyl stretch dynamics.

3.1 2D IR: Head-Group Fluctuations and Vibrational Couplings

Figure 3.2 shows broad band 2D IR spectra at a population time $T = 300$ fs. Left- and right-hand side panels of the figure were acquired with pulses of linear parallel polarization spectrally centered at 1100 and 1175 cm^{-1} , respectively, in order to measure spectra of all relevant hydration sites of the DOPC head group. All peaks from the linear spectra (Figs. 3.1 and 3.2a, b) are well reproduced in the 2D spectra. The peaks corresponding to the fundamental transition as well as their anharmonically shifted excited state absorption peaks are elongated along the

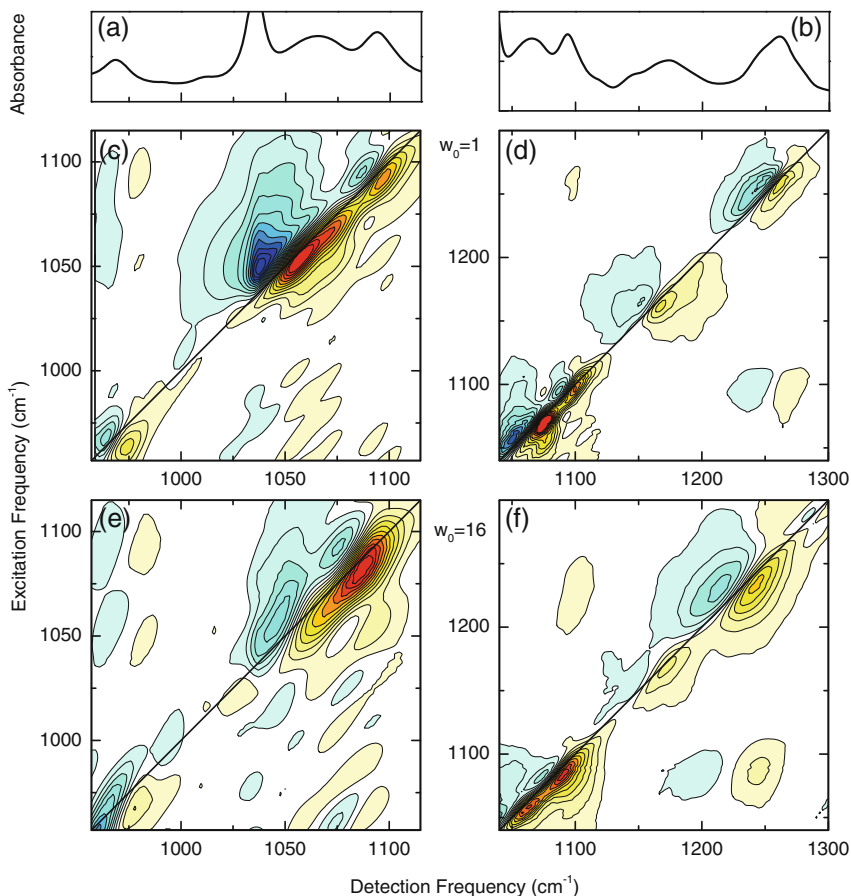


Fig. 3.2 **a, b** Linear spectra for $w_0 = 1$ and broad band 2D IR spectra for **c, d** $w_0 = 1$ and **e, f** $w_0 = 16$ at $T = 300$ fs. Vibrational modes from **a, b** are readily recognized in **c, d**. The diagonal peaks are elongated along the diagonal pointing to an inhomogeneous broadening of the vibrational transitions. Pronounced cross peaks indicate couplings between all parts of the polar head group

diagonal with $\nu_{AS}(PO_2^-)$ exhibiting a higher diagonal width than $\nu_S(PO_2^-)$. Pronounced cross peaks occur between most of the vibrational modes, e.g., for $w_0 = 1$ at $(\nu_1, \nu_3) = (1260, 1097)$ cm^{-1} and $(1095, 1265)$ cm^{-1} between the symmetric and antisymmetric phosphate stretching, at $(1055, 1095)$ cm^{-1} between the symmetric ester/in-chain C-O-P stretching and the symmetric phosphate stretching, at $(1093, 964)$ cm^{-1} between the symmetric phosphate stretching and the antisymmetric choline stretching, and at $(1060, 964)$ cm^{-1} between the symmetric ester/in-chain C-O-P stretching and the antisymmetric choline stretching. Such cross peaks suggest a significant vibrational coupling of different head-group parts which is in line with the predicted formation of charge pairs where choline and phosphate

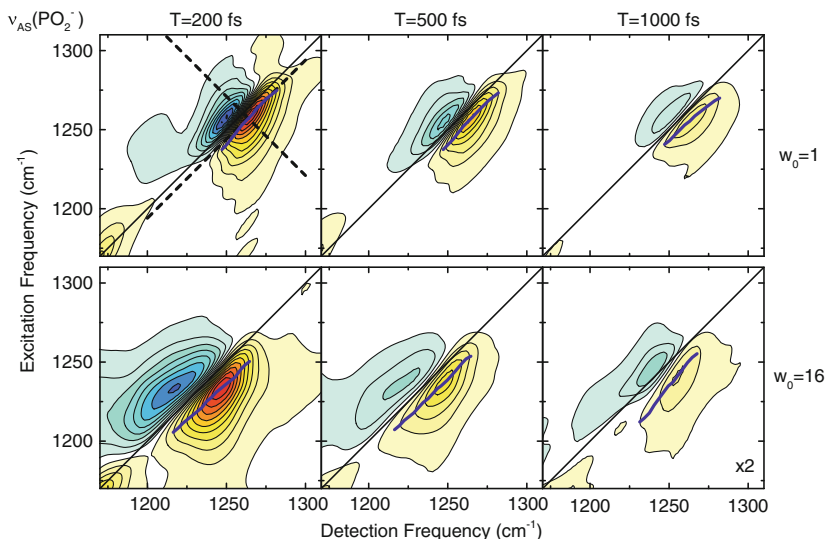


Fig. 3.3 2D IR spectra of the antisymmetric phosphate stretching vibration at $w_0 = 1$ and 16 for the population times T indicated. The elongated peak shape along the diagonal persists up to 1 ps. *Dashed lines* indicate the positions along which the cuts for $\nu_{AS}(PO_2^-)$ in Figs. 3.5 and 3.6 are drawn

groups of different phospholipids interact strongly due to their opposite electrostatic charge [7].

2D IR spectra measured for population times up to 1 ps for $\nu_{AS}(PO_2^-)$ and up to 4 ps for $\nu_S(PO_2^-)$ are presented in Figs. 3.3 and 3.4, respectively. As before, the redshift of the phosphate stretching vibrations with increasing w_0 is reproduced. Spectra at high hydration levels are slightly broader along the diagonal and antidiagonal directions. The symmetric phosphate stretching peak at $w_0 = 16$ is somewhat tilted with respect to the diagonal.

The $v = 0$ to 1 and $v = 1$ to 2 contributions of all vibrational modes have a roughly symmetrical position around the diagonal line. Such a pattern is observed when the diagonal anharmonicity values are similar to the linewidths of a vibrational transition. An overlap between two signals of opposite sign leads to a cancellation of amplitude close to the diagonal, emphasizing an important requirement for time-resolved vibrational spectroscopy: Generally, the anharmonicity of a transition is needed in order to detect a transient signal. In the case of a harmonic oscillator, signals of opposite signs would fully cancel out, resulting in a net zero signal.

Figures 3.3 and 3.4 also contain center lines (blue lines) in order to follow potentially dynamic 2D lineshapes. However, for both $\nu_{AS}(PO_2^-)$ and $\nu_S(PO_2^-)$, time-dependent changes of the peak shapes are negligible at all hydration levels which is evident from the nearly static center lines. This finding is further supported by plotting cuts along lines parallel to the frequency diagonal and antidiagonal. As an example, such lines are shown in Fig. 3.3 for $\nu_{AS}(PO_2^-)$ at $w_0 = 1$ as dashed lines.

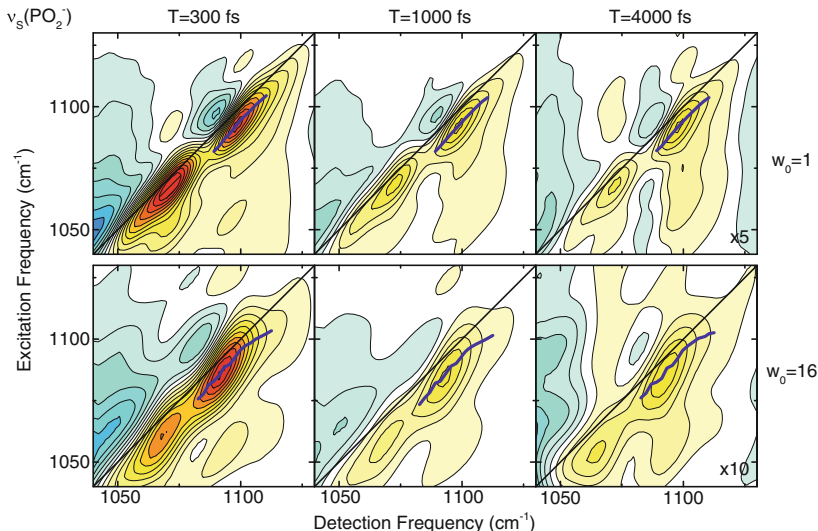


Fig. 3.4 2D IR spectra of the symmetric phosphate stretching vibration at $w_0 = 1$ and 16 for the population times T indicated. The elongated peak shape along the diagonal persists up to 4 ps. Cross peaks gain in relative intensity compared to the diagonal peaks with increasing population time

The result presented in Fig. 3.5 clearly shows that the diagonal and antidiagonal linewidths remain similar for all population times.

Time-dependent deviations occur in the low-frequency range of $\nu_S(\text{PO}_2^-)$ -diagonal cuts due to the overlap with the CO-O-C stretching vibration that has a slightly shorter lifetime. A small increase of amplitude is observed in the corresponding antidiagonal cuts in the high-frequency range. This behavior arises from increasing cross peak amplitudes at long population times (cf. Fig. 3.4) which may tentatively be assigned to energy redistribution in the head-group region. Spectra of the antisymmetric stretching vibration at $w_0 = 16$ show a blueshift at $T = 1$ ps. This shift is attributed to energy redistribution into the water pool as discussed in detail in Sect. 3.2.

Cuts along different directions contain different information about line broadening contributions. Line fitting procedures help to obtain a detailed understanding of the underlying line broadening mechanisms. We now focus on explaining the diagonal and antidiagonal widths of 2D spectra at fixed population times (cf. Fig. 3.6). 2D spectra of the phosphate stretching vibrations were calculated with the density matrix approach outlined in Sect. 2.2.1 taking into account dephasing due to frequency fluctuations and lifetime broadening. A biexponential Kubo ansatz for the frequency fluctuation correlation function (FFCF) of the form

$$C(t) = \Delta\nu_1^2 e^{-t/\tau_{c1}} + \Delta\nu_2^2 e^{-t/\tau_{c2}} \quad (3.1)$$

was chosen with the amplitudes $\Delta\nu_{1,2}$ corresponding to the correlation times $\tau_{c1,2}$. 2D spectra were calculated by changing the 4 free parameters and using the known

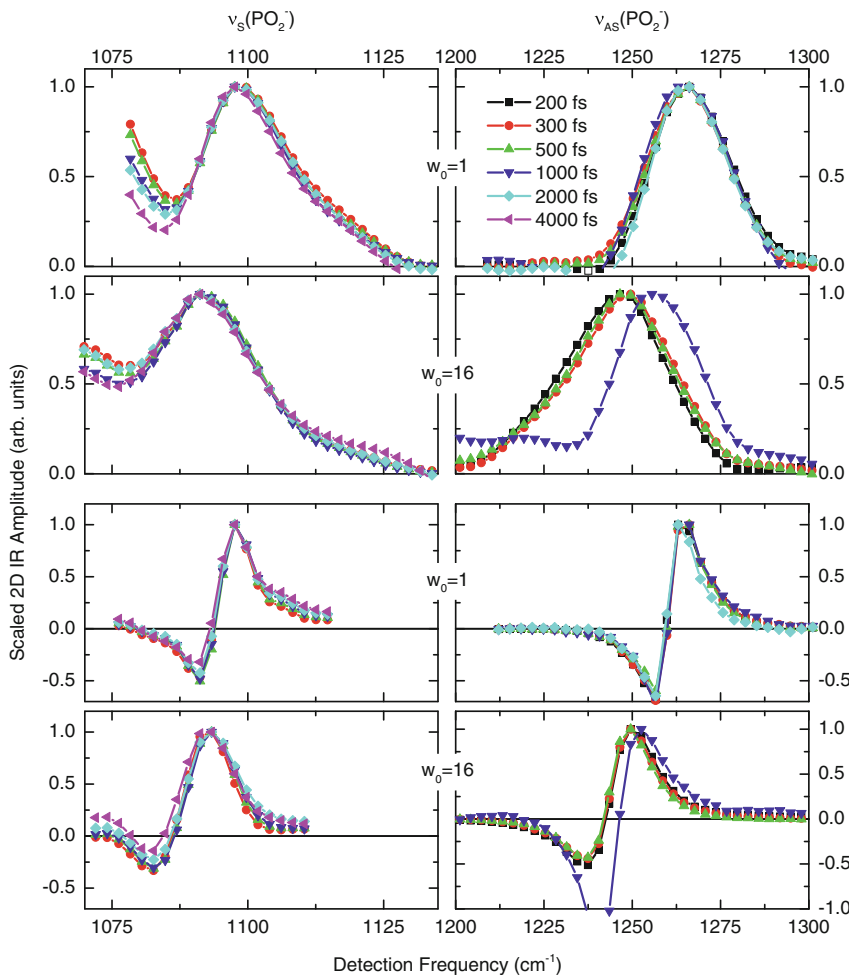


Fig. 3.5 Cuts through the maxima of the 2D spectra of $\nu_S(\text{PO}_2^-)$ (left panels) and $\nu_{AS}(\text{PO}_2^-)$ (right panels) drawn in Figs. 3.3 and 3.4. The cuts are made along lines parallel to the diagonal (top panels) and the antidiagonal (bottom panels) as indicated by the dashed lines in the first panel of Fig. 3.3. All traces are normalized to illustrate the static 2D diagonal and antidiagonal widths. Spectra for $\nu_{AS}(\text{PO}_2^-)$ are measured up to 1 ps and 2 ps for $w_0 = 1$ and 16, respectively due to their shorter vibrational lifetime. The antisymmetric phosphate stretching vibration shows a blueshift for $w_0 = 16$ at $T = 1$ ps

T_1 lifetime (cf. Sect. 3.2). Diagonal and antidiagonal cuts were extracted to fit the experimental ones in Fig. 3.6. Table 3.1 summarizes the fit parameters used and Figs. 3.7 and 3.8 show the resulting calculated spectra. It should be noted that lifetime broadening contributes to the homogeneous linewidth that is reflected in the width of antidiagonal cuts. Dashed lines in Fig. 3.6 for $\nu_S(\text{PO}_2^-)$ ($w_0 = 1$) illustrate that

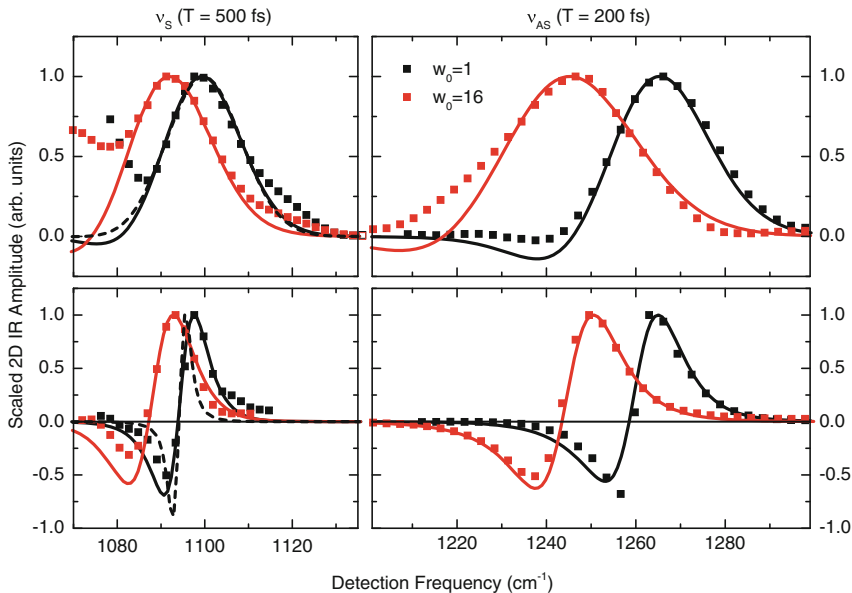


Fig. 3.6 Diagonal (*top panels*) and anti-diagonal (*bottom panels*) cuts through maxima of the 2D spectra of $\nu_S(\text{PO}_2^-)$ at $T = 500$ fs (*left*) and $\nu_{AS}(\text{PO}_2^-)$ at $T = 200$ fs (*right*). Squares display experimental results. Solid lines represent similar cuts through the calculated spectra (Figs. 3.7 and 3.8) using a Kubo ansatz with the parameters summarized in Table 3.1. The dashed lines correspond to calculated spectra of $\nu_S(\text{PO}_2^-)$ ($w_0 = 1$) assuming an inhomogeneous lineshape that is further broadened due to the finite vibrational lifetime. The anti-diagonal cut is too narrow, demonstrating the necessity to incorporate a fast component in the FFCF

Table 3.1 Parameters used to fit the experimental 2D spectra of the phosphate stretching vibrations. A fast 300 fs decay time of the FFCF as well as an inhomogeneous component are needed to fit the experimental spectra independent of the hydration level w_0 and the phosphate vibration used in the analysis. The T_1 lifetimes will be discussed in detail in Sect. 3.2

Mode	w_0	$\Delta\nu_1$ (cm^{-1})	τ_{C1} (fs)	$\Delta\nu_2$ (cm^{-1})	τ_{C2} (fs)	T_1 (fs)
$\nu_S(\text{PO}_2^-)$	1	8.5	300	8.5	∞	1500
	16	11	300	8.5	∞	1000
$\nu_{AS}(\text{PO}_2^-)$	1	5	300	10	∞	300
	16	7	300	14	∞	300

lifetime broadening only is not sufficient to fit the experimental results. In contrast, the experimental results are well reproduced by using the biexponential FFCF. Deviations in the wings of the spectra mainly arise from overlapping bands and cross peaks that are not included in the calculations.

Apparently, the FFCF consists of an inhomogeneous component ($\tau_{C2} \rightarrow \infty$) that is static on the time scale of the experiment and a fast decay component with a 300 fs correlation time for all hydration levels and for both, $\nu_S(\text{PO}_2^-)$ and $\nu_{AS}(\text{PO}_2^-)$. While

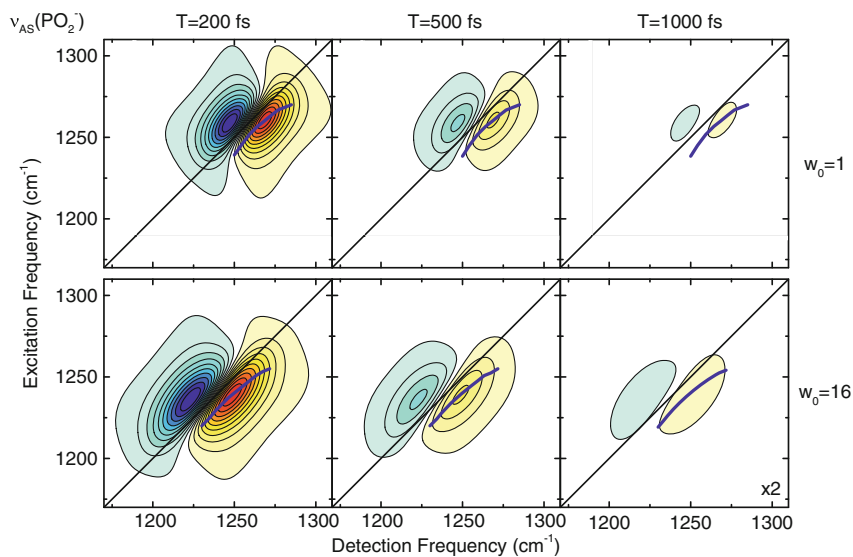


Fig. 3.7 Calculated 2D IR spectra of the antisymmetric phosphate stretching vibration at $w_0 = 1$ and 16

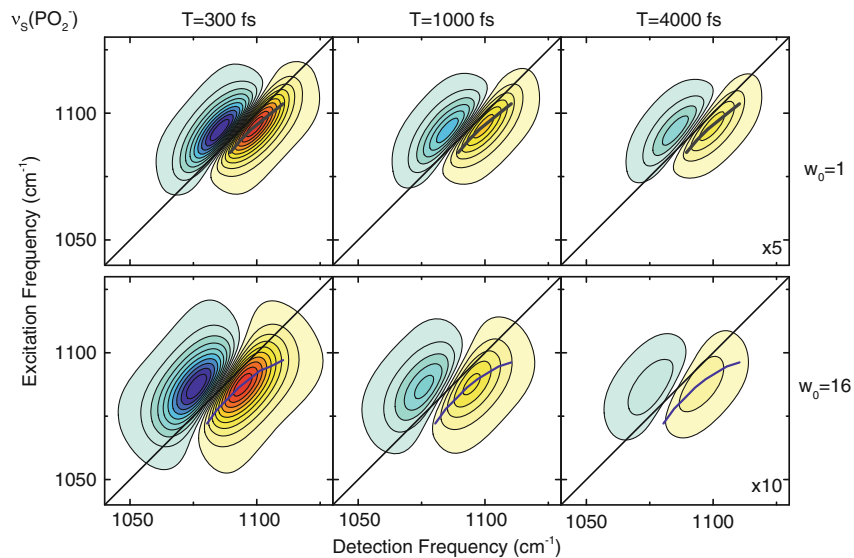


Fig. 3.8 Calculated 2D IR spectra of the symmetric phosphate stretching vibration at $w_0 = 1$ and 16

the inhomogeneous component mainly affects the diagonal width of the 2D spectra, the anti-diagonal width increases with the fast component's amplitude and—to some extent—its inverse correlation time. The pronounced inhomogeneity is therefore the reason for the elongated spectra with a shape persisting well into the regime of a few picoseconds. A fast decay component of the FFCF leads to a quick partial loss of the correlation between the excitation and detection frequencies causing the significant off-diagonal amplitude in the 2D spectra.

The amplitude of the fast FFCF-decay component increases only slightly with the water content of the reverse micelles. It is therefore attributed to the fluctuating character of the phospholipid head groups. THz absorption spectra of phospholipid bilayers with different head groups show pronounced absorption bands for phosphatidylcholines in the range of 100 cm^{-1} that are assigned to intermolecular head-group modes [8]. The corresponding motions on a roughly 300 fs time scale modulate the electric potential in the lipid head-group region. Such modulations are sensed by the phosphate vibrations whose vibrational frequencies are sensitive probes of the head-group configuration. 2D spectroscopy as employed in this thesis is therefore a highly suitable method for a direct observation of fast lipid head-group fluctuations.

The pronounced inhomogeneous character of the vibrational bands indicates a heterogeneous head-group conformation arising from inhomogeneous distributions of head-group dipoles and hydration structures. The experimental results point to the fact that lipid-water hydrogen bonds are preserved despite the fast head-group fluctuations. Since there is a strong redshift of the linear phosphate stretching spectra with increasing hydration, breaking of hydrogen bonds should result in a significant frequency shift of those vibrations. Figure 3.9 shows calculated spectra where the assumption is made that the inhomogeneous contribution to the FFCF decays on a 10 ps time scale, i.e., $\tau_{C2} = 10\text{ ps}$. Clear signs of spectral diffusion are observed for spectra at 4000 fs. Such a reshaping is absent in the measured spectra and therefore 10 ps can be set to be the lower limit of phosphate-water hydrogen-bond lifetimes.

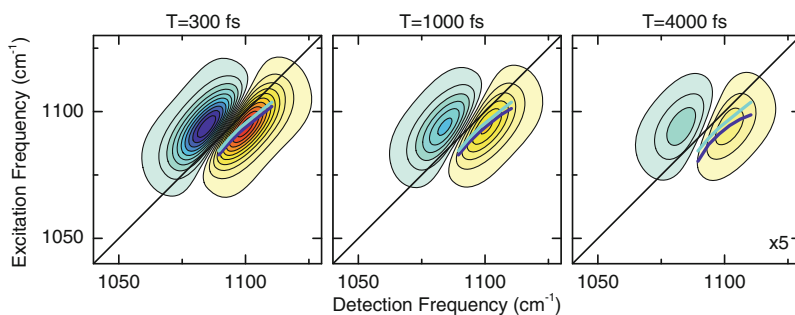


Fig. 3.9 Calculated 2D IR spectrum of $\nu_S(\text{PO}_2^-)$ at $w_0 = 1$ with the assumption of $\tau_{C2} = 10\text{ ps}$. Clear indications of spectral diffusion at $T = 4000\text{ fs}$ are observed through a change of the 2D lineshape and the center lines (blue lines). For comparison, the static center lines ($\tau_{C2} \rightarrow \infty$) from Fig. 3.8 are also shown (cyan lines) (color figure online)

This time scale is determined by the limited observation time that is fixed by the T_1 lifetime of $\nu_S(PO_2^-)$.

3.2 Energy Relaxation: Heat Sink Function of Small Water Pools

The decay of 2D IR signals maps the decay of vibrational excitations and is therefore related to the T_1 lifetime. Since measurements of 2D spectra with N_{exc} points on the excitation-frequency axis require sampling N_{exc} coherence-time points they are a factor of N_{exc} more time-consuming than measurements of pump-probe spectra without resolution of the excitation frequency. Pump-probe experiments can thus be helpful for the precise determination of vibrational lifetimes, if contributions of different vibrational transitions are well-resolved.

Figure 3.10 shows a summary of pump-probe experiments of the symmetric phosphate stretching vibration with pump pulses centered at 1100 cm^{-1} . Negative signals in the pump-probe spectra correspond to the $v = 0$ to 1 contributions of the symmetric phosphate stretching vibration as well as the symmetric CO-O-C ester stretching C-O-P stretching vibrations. The time-resolved pump-probe spectra obviously do not resolve the individual $v = 1$ to 2 transitions due to the overlap with the bleaching contributions. Since the 2D spectra show a similar time-dependent behavior of the $v = 0$ to 1 and the $v = 1$ to 2 signals, the use of the negative absorbance change to extract excited state lifetimes is appropriate.

The corresponding transients are shown as solid squares in Fig. 3.10b, d. For comparison, the inverted maximum 2D signals of those peaks are plotted as open squares. The similarity of the results measured with two different techniques justifies the use of pump-probe data to extract vibrational lifetimes. At both values of w_0 , there is a spike around zero delay time caused by coherent pump-probe coupling. In order to avoid artifacts in the data analysis, fitting is performed for data points after delay times of 300 fs only. Single exponential fits of the transients show symmetric phosphate stretching vibrational lifetimes of 1.5 and 1.0 ps for $w_0 = 1$ and 16, respectively. Note that the long-term signals at both hydration levels show a slight offset with respect to zero that is higher for the case of $w_0 = 1$. Such signals typically arise from anharmonic coupling to low-frequency modes that are populated during vibrational energy redistribution. Moreover, cross peaks that obviously contribute to the 2D spectra at long population times (cf. Fig. 3.4) may affect the pump-probe data at long delay times due to the lack of excitation-frequency resolution. The shorter $v = 1$ lifetime of $\nu_S(PO_2^-)$ at $w_0 = 16$ as well as the weaker signal due to anharmonic coupling at long delay times suggest that water mediates a faster and more efficient energy relaxation of symmetric phosphate stretching excitations.

A more detailed picture is obtained from time-resolved pump-probe measurements of the antisymmetric phosphate stretching vibration. Pump-probe spectra recorded with pump pulses centered at 1250 cm^{-1} and a spectral bandwidth of

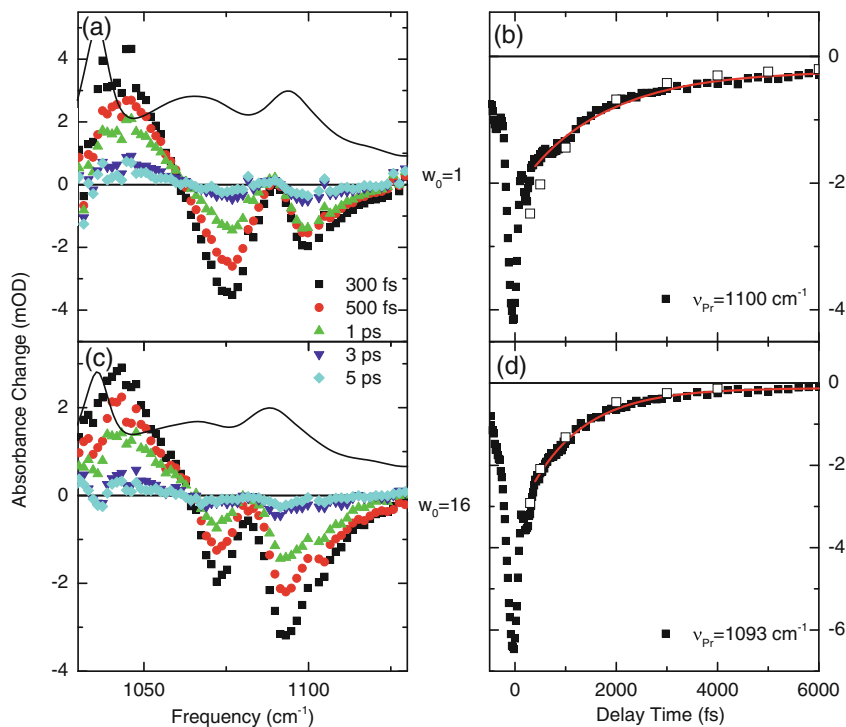


Fig. 3.10 **a, c** Pump-probe spectra and **b, d** time-resolved absorbance change at the fundamental of the symmetric phosphate stretching vibration. Linear absorption spectra are included in **a, c** indicating that the negative absorbance-change features arise from the CO-O-C ester stretching, C-O-P stretching and symmetric phosphate stretching vibration. The decay of these signals monitoring the $v = 0$ to 1 transition of $\nu_S(PO_2^-)$ (solid squares in **b, d**) fit well to exponential decays with time constants of 1.5 and 1.0 ps for $w_0 = 1$ and 16, respectively (red lines). For comparison, the inverted 2D IR signal amplitude of the corresponding peaks in Fig. 3.4 are included as open squares (color figure online)

$\approx 180 \text{ cm}^{-1}$ are shown in Fig. 3.11 a–d (parallel linear polarization of pump and probe pulses). Such conditions lead to a negligible excitation of the symmetric phosphate stretching vibrations and the pump-probe data are thus dominated by the vibrational energy relaxation pathway of the excited $\nu_{AS}(PO_2^-)$ mode. At early delay times, the transient spectra show the usual negative contributions of the $v = 0$ to 1 bleach and stimulated emission as well as the positive excited state absorption signal. For comparison, we include the respective linear spectra as dashed lines in Fig. 3.11 a–d illustrating that the hydration-dependent shift is reproduced in the pump-probe spectra. Note that the width of the transient spectra increases with hydration. In contrast, the spectral shapes are similar, i.e., a lineshape analysis would be much less unique than it is for the 2D spectra. The transient absorbance change decays with increasing delay times and shows a more efficient relaxation at high hydration levels. At a 5 ps

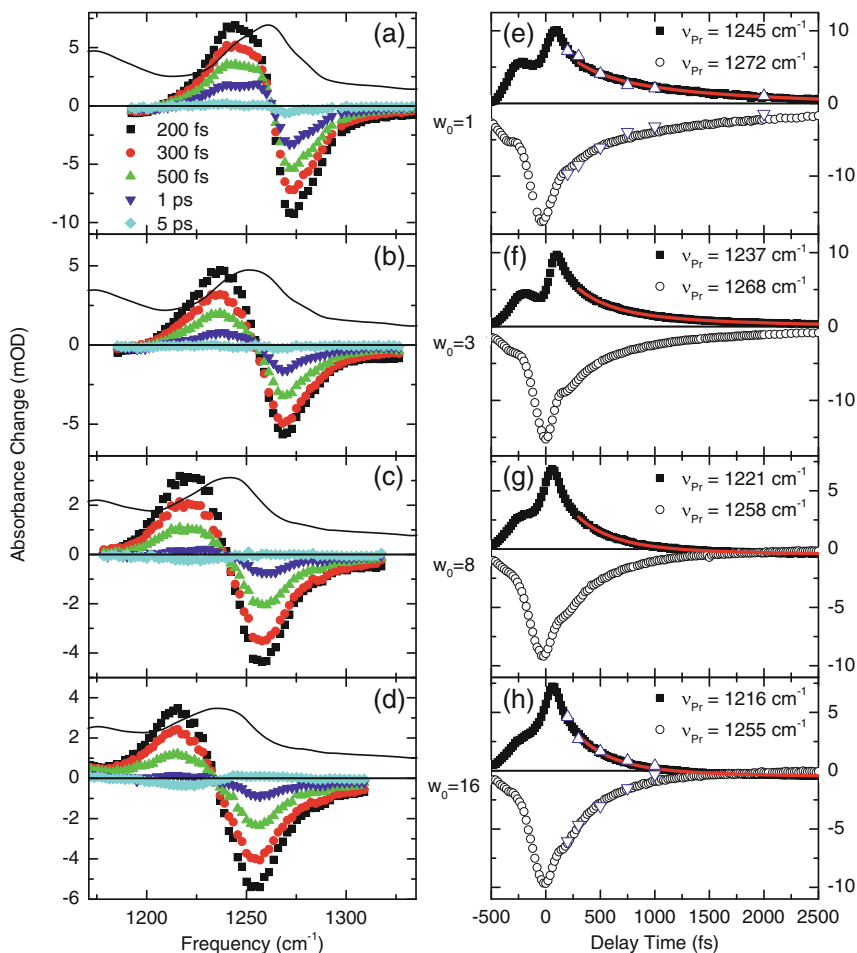


Fig. 3.11 Pump-probe data of the antisymmetric phosphate stretching vibration for hydration levels $w_0 = 1$ to 16 (top to bottom) obtained with pump pulses centered at 1250 cm^{-1} . **a–d** Pump-probe spectra measured with parallel linear polarization of pump and probe pulses. The redshift of the linear spectra (lines) with increasing hydration is reproduced in the time-resolved data. Transient spectra for high hydration levels show a more efficient energy relaxation and a sign reversal at late delay times due to energy transfer to the water pool. **e–h** Isotropic transient absorbance change at the fixed probe frequencies corresponding to the maximum and minimum signal of the spectra **a–d**. The red lines indicate biexponential decay fits with time constants of 300 fs and ≈ 1000 fs. Exact parameters are given in Table 3.2. Blue triangles in **e, h** indicate the inverted 2D IR signal amplitudes (Fig. 3.3) (color figure online)

delay, there is a slight inverted residual signal for $w_0 = 8$ and 16, i.e., the enhanced absorption at early delay times turns into a bleach and vice versa.

The transient spectra are understood by fitting their time evolution. Figure 3.11 e–h show the time evolution at frequency positions corresponding to the maxi-

Table 3.2 Fit parameters for the antisymmetric phosphate stretching vibration dynamics (red lines in Fig. 3.11e–h) assuming a biexponential signal decay
 $\Delta A(t) = A_1 e^{-t/\tau_1} + A_2 e^{-t/\tau_2}$

w_0	τ_1 (fs)	τ_2 (fs)	A_1/A_2
1	300	1300	1.2
3	300	1100	3.0
5	300	1100	4.4
8	300	1000	5.3
16	300	1100	6.9

imum and minimum positions of the transient spectra. Isotropic signals $\Delta A_{iso} = (\Delta A_{||} + 2 \cdot \Delta A_{\perp})/3$ are plotted. Such traces are free of reorientational effects due to orientational fluctuations and rotations of the head groups or energy transfer to neighboring phosphate groups. Inverted maximum 2D IR signals are plotted as blue triangles in Fig. 3.11e, h and the data points are in good agreement with the pump-probe results. As before data fitting is restricted to delay times longer than 300 fs to avoid the influence of coherent pump-probe coupling. The data fit well to biexponential decays with a fast component of 300 fs and a slow component of about 1 ps (cf. Table 3.2). These values were obtained by fixing the short decay time and using the two amplitudes and the longer decay time as free parameters. Within the error margin of approximately 10%, the decay constants are similar for all hydration levels whereas the relative amplitudes of the two components clearly change. While fast and slow components have similar amplitudes for $w_0 = 1$, the fast component dominates in the $w_0 = 16$ case. Furthermore, the sign reversal of the transient absorption change visible for $w_0 = 8$ and 16 at delay times of 2500 fs is another indicator of an influence of water pools on the vibrational relaxation of $\nu_{AS}(PO_2^-)$.

Pump-probe measurements of the antisymmetric phosphate stretching vibration of phosphate groups in DNA-oligomer backbones exhibit lifetimes of 340 fs independent of the hydration level [6]. Since the DOPC data show a similar fast component with a 300 fs time constant which is again independent of the hydration level, this decay is attributed to the lifetime of phosphate stretching vibrations in DOPC reverse micelles. The similarity of lifetimes for two different systems and for different degrees of hydration suggests a similar first step of vibrational energy redistribution that must involve modes of the initially excited phosphate group. Combination bands of different in-chain dialkyl phosphate vibrations such as the diester stretching modes around 800 cm^{-1} with the wagging and twisting modes at 476 and 367 cm^{-1} [9, 10] would have a similar frequency as $\nu_{AS}(PO_2^-)$ so that efficient energy relaxation into those low-frequency modes could occur.

Keeping in mind that the excited-state population decays with the T_1 lifetime of 300 fs, the residual signals at delay times longer than the vibrational lifetime must consist of the bleaching of the originally excited transition and an extra signal arising due to anharmonic coupling to the low-frequency modes that serve as energy acceptors. The transient absorbance change at long delay times is therefore a sensitive probe for monitoring energy redistribution into the vibrational manifold. At a hydration level of $w_0 = 16$, the slow component is almost absent indicating a fast

transfer of vibrational energy into accepting modes of the water pool. Such modes are removed at a low water content so that the energy has to be redistributed within the phospholipid and finally dissipated into the benzene solvent. The time scale of this process should depend on the environment of the phosphate group. We point out that the slow component of 1 ps measured here is much faster than the 5.5 ps component found for DNA [6] indicating that energy redistribution is faster in phospholipids, e.g., due to more efficient energy transfer to surrounding head groups or to the glycerol/hydrocarbon chain region.

The sign reversal of the transient signals at long times for high hydration levels is rationalized with the heating effect caused by energy disposal into the water pools. A simple calculation yields the temperature jump caused by the vibrational excitation: We excite $\nu_{AS}(PO_2^-)$ by using $2\ \mu\text{J}$ pulses at a frequency of $1250\ \text{cm}^{-1}$ and a spectral bandwidth of $180\ \text{cm}^{-1}$. The pulses are focussed to a diameter of $\approx 100\ \mu\text{m}$ (FWHM). Taking into account that the optical density and the spectral width of the phosphate stretching vibration are 0.5 and $40\ \text{cm}^{-1}$, respectively, we find that $\approx 0.14\ \mu\text{J}$ of energy are absorbed in the central excitation volume of $\approx 1.9 \cdot 10^{-7}\ \text{cm}^{-3}$. Assuming that the whole energy absorbed by $\nu_{AS}(PO_2^-)$ is accepted by the water pool (concentration = 2 M at $w_0 = 8$), the calculated temperature increase is about 5 K. Such a temperature change is expected to modify the hydrogen-bond strengths between water and phospholipid head groups, resulting in a change of the vibrational frequencies of characteristic marker bands of the phosphate groups as well as the water.

Figure 3.12 shows the effect of heating DOPC reverse micelles ($w_0 = 8$) with three different methods. Heating the sample in a temperature-controlled cuvette leads to a blueshift of the transition frequency of the antisymmetric phosphate stretching vibration (Fig. 3.12a). The differential spectrum (solid line in Fig. 3.12b) consists of a positive contribution at high frequencies and a negative one at low frequencies just like the transient behavior of $\nu_{AS}(PO_2^-)$ measured at a pump-probe delay time of 10 ps (solid symbols in Fig. 3.12b). It should be emphasized that the character of temperature increase is different for the two methods. While the first method increases the temperature of the sample as a whole, remaining in a thermal equilibrium that is slightly changed compared to the cold sample, heating with ultrashort pulses creates temperature jumps at well-defined microscopic positions, e.g., heating of the water pool inside the reverse micelle while most of the benzene solvent remains unaffected. However, in both cases the spectral shift can be explained with the same qualitative picture of weakened phosphate-water hydrogen bonds due to the increased temperature.

It should be mentioned that temperature jumps can also be induced by a direct excitation of the water OH stretching vibrations (open symbols in Fig. 3.12b, measured at a delay time of 10 ps). The width of the linear OH stretching spectra is similar to the bandwidth of the pump pulse, leading to a higher absorption of $\approx 0.5\text{--}1.0\ \mu\text{J}$

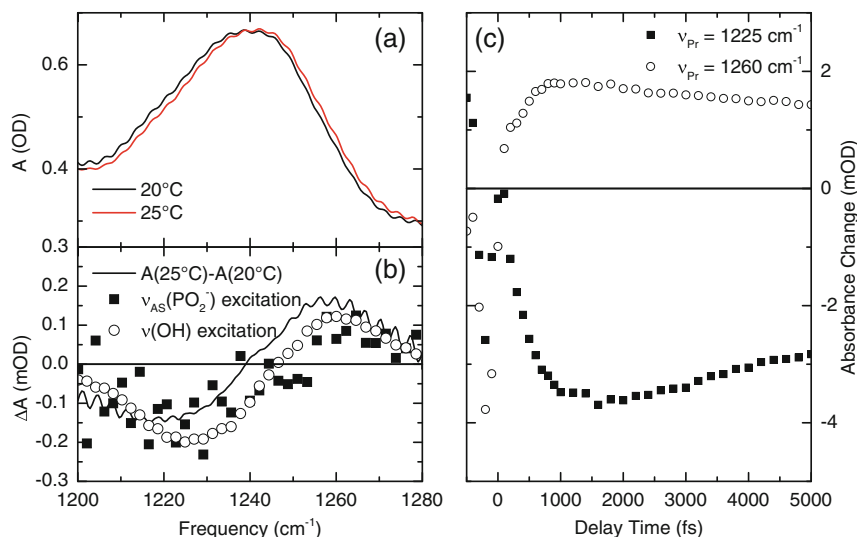


Fig. 3.12 Response of $\nu_{AS}(PO_2^-)$ to heating. **a** Temperature-dependent linear spectra for $w_0 = 8$ at $T_{sample} = 20^\circ\text{C}$ and 25°C . The temperature increase causes a blueshift of the vibrational absorption band represented by the scaled differential spectrum in **b**. For comparison, the transient spectra of $\nu_{AS}(PO_2^-)$ 10 ps after phosphate or OH stretch excitation are plotted as symbols where the data for the OH stretch excitation is scaled down by a factor of 8. The time evolution of the transient phosphate stretching response after OH stretching excitation is shown in **c**

per pulse. Correspondingly, the temperature increase is about 5 times higher than after phosphate excitation. As a result, the phosphate response under these conditions is higher, evident in the data of Fig. 3.12b which is downscaled by a factor of 8. Following the transient absorbance change reveals that a maximum signal is reached after 1 ps (Fig. 3.12c). The time scale of the delayed signal rise directly reflects the energy redistribution in phospholipid hydration shells as discussed in Chap. 4.

In summary, the pump-probe kinetics presented in this work demonstrate the prominent role of water in dissipating vibrational energy of phosphate stretching excitations. Nanoscopic water pools act as efficient heat sinks ensuring ultrafast vibrational energy redistribution on a sub-ps time scale. In this way, damage due to thermal heating of phospholipids, e.g., by absorption of UV photons may be prevented.

As pointed out in Sect. 1.1, the phosphate groups are hydrated by up to 6 water molecules. Other hydration sites are the carbonyl groups that on average form strong hydrogen bonds to approximately one water molecule even at low hydration. In the following, the influence of increasing the water pool size on the carbonyl vibrational dynamics will be investigated.

3.3 Hydration-Insensitivity of Carbonyl Dynamics

Figure 3.13 summarizes pump-probe data of the carbonyl stretching vibration centered around 1740 cm^{-1} . Both linear and transient spectra (cf. Fig. 3.13a, c) have similar lineshapes for $w_0 = 1$ and 16 with a slightly increasing spectral width at high hydration levels. A minor redshift of the carbonyl stretching vibration of 2 cm^{-1} with increasing w_0 that may be seen in the linear spectra is caused by the overlap with the OH bending vibration of the hydration at a frequency of 1650 cm^{-1} . The decays of the transient signals caused by the $\nu = 0$ to 1 bleach and stimulated emission at 1719 cm^{-1} as well as the $\nu = 1$ to 2 excited state absorption at 1748 cm^{-1} are virtually indistinguishable for the two different hydration levels (Fig. 3.13b, d). Table 3.3 contains fit parameters of a biexponential model showing very similar decay con-

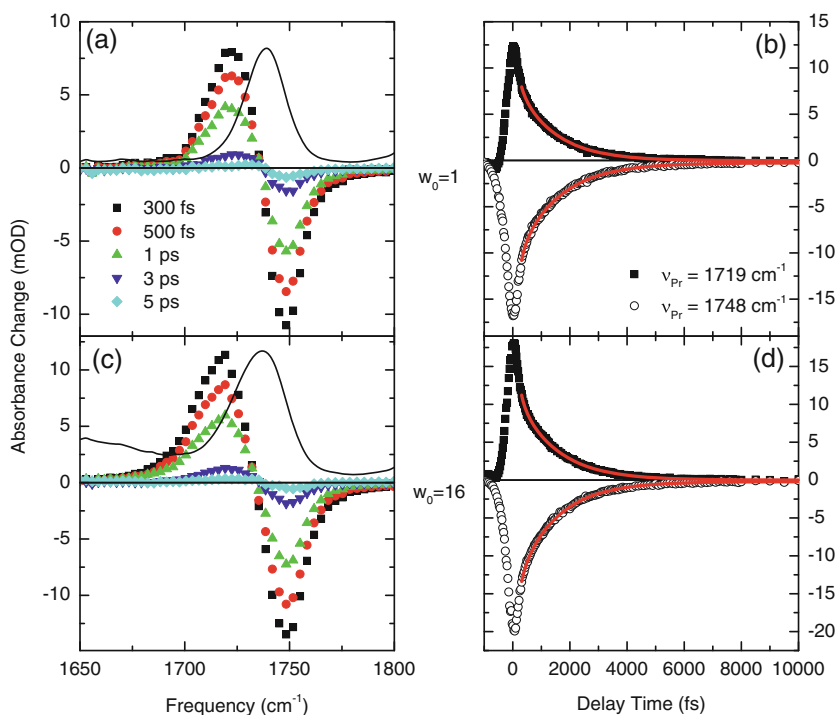


Fig. 3.13 Vibrational dynamics of the carbonyl stretching vibration. **a, c** Transient spectra (symbols) for $w_0 = 1$ and 16 are similar to each other with a slightly higher spectral width at $w_0 = 16$. This result is in line with the behavior of linear spectra (*solid lines*, the extra absorption at $w_0 = 16$ is caused by the OH bending vibration of water centered at 1650 cm^{-1}). **b, d** Transient absorbance change of the $\nu = 0$ to 1 and $\nu = 1$ to 2 transition at the frequency positions indicated. All transients fit to a biexponential decay with time constants of 150 fs and 1300 fs (*red lines*, cf. Table 3.3) (color figure online)

Table 3.3 Fit parameters for the transient signal of the carbonyl stretching mode (red lines in Fig. 3.13b, d) assuming a biexponential signal decay $\Delta A(t) = A_1 e^{-t/\tau_1} + A_2 e^{-t/\tau_2}$ for both, the $\nu = 1$ to 2 and $\nu = 0$ to 1 contributions

ν (cm ⁻¹)	w_0	τ_1 (fs)	τ_2 (fs)	A_1/A_2
1719	1	150	1300	0.73
	16	150	1400	0.95
1748	1	150	1400	0.96
	16	150	1300	0.77

stants of 150 fs and 1300–1400 fs. The relative amplitude of both components does not depend on the water content.

There are several possible reasons for the biexponential decay: (i) The carbonyl lifetime is 150 fs and the longer relaxation time maps the energy redistribution within the phospholipid similar to the characteristic decay of antisymmetric phosphate stretching vibrations. (ii) It was shown that the carbonyl stretching band consists of at least two individual peaks that are assigned to hydrated and non-hydrated C=O groups [11] and the two relaxation times might be attributed to the two chemically inequivalent carbonyl moieties. (iii) The fast component is due to coherent pump-probe coupling and the slow component is a measure of the carbonyl stretching lifetime.

If the carbonyl lifetime was 150 fs, a significant lifetime-broadening contribution to the homogeneous linewidth would be expected. Assuming that the homogeneous dephasing time is dominated by vibrational relaxation ($T_2 = 2T_1$, cf. Eq. 2.37), a homogeneous linewidth of 35 cm⁻¹ (cf. Eq. 2.22) is obtained. This value clearly exceeds the bandwidth of the linear absorption spectra that increases from 22 cm⁻¹ at $w_0 = 1$ to 26 cm⁻¹ at $w_0 = 16$. Therefore, possibility (i) is ruled out. The same argument is used to dismiss possibility (ii). Further support is provided by the transient spectra. If two differently hydrated carbonyl groups had different vibrational lifetimes, the broad spectral component due to the short lifetime should decay quickly. As a result, one would observe a transient reshaping of the pump-probe spectra that is clearly absent in the data (Fig. 3.13a, c). Thus, the fast component can only be explained by mechanism (iii), coherent pump-probe coupling.

The 1300–1400 fs time constant is therefore attributed to the lifetime of the carbonyl stretching vibration. The fact that the dynamics are similar for $w_0 = 1$ and 16 is in striking contrast to the phosphate stretching dynamics discussed above. Apparently, intracellular water pools do not act as heat sinks for carbonyl stretching vibrations. Such behavior might be caused by the different hydration structures of phosphate and carbonyl groups. While the phosphate groups are located well in the hydrophilic region of the phospholipid head groups exhibiting a large area for hydrogen-bond acceptance, the carbonyl groups represent a boundary between the hydrophilic and hydrophobic parts of the lipid and accept only one hydrogen bond. An increase of w_0 does not alter the hydration of the carbonyl groups significantly so that a minor influence of carbonyl vibrational dynamics appears reasonable.

References

1. U.P. Fringeli, H.H. Günthard, Infrared membrane spectroscopy, in *Molecular Biology, Biochemistry and Biophysics*, ed. by E. Grell (Springer, Berlin, 1981), pp. 270–332
2. M. Jackson, H.H. Mantsch, Biomembrane structure from FT-IR spectroscopy. *Spectrochim. Acta Rev.* **15**, 53–69 (1993)
3. R.N.A.H. Lewis, R.N. McElhaney, Fourier transform infrared spectroscopy in the study of hydrated lipids and lipid bilayer membranes, in *Infrared Spectroscopy of Biomolecules*, ed. by H.H. Mantsch, D. Chapman (Wiley-Liss, Inc., New York, 1996), pp. 195–202
4. W.R. Angus, C.R. Bailey, J.B. Hale, C.K. Ingold, A.H. Leckie, C.G. Raisin, J.W. Thompson, C.L. Wilson, Structure of benzene. Part VIII. Assignment of vibration frequencies of benzene and hexadeuterobenzene. *J. Chem. Soc.* 971–987 (1936)
5. V.V. Volkov, R. Chelli, W. Zhuang, F. Nuti, Y. Takaoka, A.M. Papini, S. Mukamel, R. Righini, Electrostatic interactions in phospholipid membranes revealed by coherent 2D IR spectroscopy. *Proc. Natl. Acad. Sci. USA* **104**, 15323–15327 (2007)
6. Ł. Szyc, M. Yang, T. Elsaesser, Ultrafast energy exchange via water-phosphate interactions in hydrated DNA. *J. Phys. Chem. B* **114**, 7951–7957 (2010)
7. M. Pasenkiewicz-Gierula, Y. Takaoka, H. Miyagawa, K. Kitamura, A. Kusumi, Charge pairing of headgroups in phosphatidylcholine membranes: a molecular dynamics simulation study. *Biophys. J.* **76**, 1228–1240 (1999)
8. R. Hielscher, P. Hellwig, Specific far infrared spectroscopic properties of phospholipids. *Spectrosc. Int. J.* **27**, 525–532 (2012)
9. Y. Guan, C.J. Wurrey, G.J. Thomas Jr., Vibrational analysis of nucleic acids. I. The phosphodiester group in dimethyl phosphate model compounds: $(\text{CH}_3\text{O})_2\text{PO}_2^-$, $(\text{CD}_3\text{O})_2\text{PO}_2^-$, and $(^{13}\text{CH}_3\text{O})_2\text{PO}_2^-$. *Biophys. J.* **66**, 225–235 (1994)
10. H. Binder, W. Pohle, Structural aspects of lyotropic solvation-induced transitions in phosphatidylcholine and phosphatidylethanolamine assemblies revealed by infrared spectroscopy. *J. Phys. Chem. B* **104**, 12039–12048 (2000)
11. A. Blume, W. Huebner, G. Messner, Fourier transform infrared spectroscopy of $^{13}\text{C}=\text{O}$ labeled phospholipids hydrogen bonding to carbonyl groups. *Biochemistry* **27**, 8239–8249 (1988)

Chapter 4

Ultrafast Vibrational Dynamics of Phospholipid Hydration Shells

Ultrafast vibrational dynamics of bulk water have been studied intensively since the advent of ultrashort mid-infrared pulses with pulse energies in the microjoule regime. First experiments focussed on the local OH stretching vibration of isotopically diluted water, i.e., HOD in D₂O. Pump-probe data, partly measured with insufficient time resolution, found OH stretching decays on a 700 fs time scale that depends slightly on the temperature and OH stretching frequency. This is complemented by a spectral reshaping on a picosecond time scale [1–7]. It has been debated whether energy relaxation proceeds via the water bending vibration or through predissociation of hydrogen bonds. Molecular dynamics simulations mainly addressed the former mechanism to explain the vibrational lifetimes [8–11].

Another goal of the pump-probe studies was to investigate structural dynamics of water molecules that are embedded in a tetrahedral structure establishing hydrogen bonds with their four nearest neighbors. Different explanations for the spectral shape of OH stretching excitations assume either a heterogeneous multicomponent structure caused by different discrete hydrogen-bond geometries or a continuous distribution of hydrogen-bond lengths leading to different OH stretching frequencies. The issue of line broadening mechanisms was solved by the development of integrated two-pulse photon echo [12], heterodyne-detected two-pulse photon echo [13] and heterodyne detected three-pulse photon echo techniques [14, 15]. With the help of molecular dynamics simulations, fast dephasing times on the order of 100 fs were assigned to the effect of a fluctuating electric force originating from hindered translations and rotations that acts on a single hydrogen bond while a slower picosecond component is due to the reorganization of the whole hydrogen-bond network [16–18]. It should be noted that similar results were found for the OD stretching vibration of HOD in H₂O with a somewhat longer vibrational lifetime of 1.4 ps [19].

The vibrational structure of neat H₂O is distinctly different from the one of isotopically diluted water. Due to the similar frequency of the two OH stretching oscillators of one water molecule, a local mode representation for the OH stretching vibrations is no longer appropriate and mechanical coupling leads to mode splitting. As a result, the absorption band is broadened further compared to isotopically diluted water. The water bending vibration is located at about half the stretching frequency. A Fermi

resonance between the $\nu = 2$ of the bending and the red part of the broad ($\nu = 1$) stretching absorption band facilitates efficient OH stretching energy relaxation to the bending vibration on a time scale of 200–260 fs at room temperature [20–23]. Shorter 170 fs lifetimes were measured for the OH bending vibration [21, 24]. Here, energy transfer to intermolecular librational modes is the dominant decay channel [25–27]. Randomization of librational excitation occurs with a very fast sub-100 fs time constant [28, 29].

OH stretching frequencies are sensitive probes for hydrogen-bonding configurations and 2D IR spectroscopy demonstrated rapid spectral diffusion on a 50 fs time scale sampling the whole absorption spectrum [30, 31]. Such a fast dephasing was attributed to ultrafast structural fluctuations of the hydrogen-bond network, in particular caused by the librations. An additional contribution arises from resonant OH stretching excitation transfer where strong dipole-dipole and higher-order multipole coupling of adjacent OH stretching oscillators lead to energy transfer between water molecules. This process is also reflected in an ultrafast pump-probe anisotropy decay on the time scale of 100 fs [32].

It is important to emphasize that structural dynamics and energy dissipation depend decisively on the presence and nature of hydrogen bonds. Hydrogen bonding induces a redshift of the stretching and a blueshift of the bending modes thereby allowing efficient OH stretching relaxation by minimizing the energy mismatch with the bend overtone. Additionally, intermolecular vibrations caused by the presence of hydrogen bonds act as acceptors of vibrational excess energy, e.g., for fast OH bending relaxation to the librations. Naturally, much longer vibrational lifetimes in the range of tens of picoseconds were found for water monomers dissolved in nonpolar solvents where water cannot form hydrogen bonds [33, 34].

Reverse micelles with variable water content are systems ideally suited to probe water dynamics at charged interfaces and study the transition to bulk-like behavior as w_0 is increased. The OH stretching lifetime of H₂O in AOT reverse micelles at $w_0 = 1$ is 850 fs [35–37], i.e., significantly longer than the one for bulk water but shorter than the one for water monomers. A core/shell model was applied to fit pump-probe dynamics for both H₂O and HOD in H₂O modeling water as two independent species one of which interacts with the AOT head groups and the other exhibiting a bulk-like behavior [37, 38]. While increased vibrational lifetimes of water in the vicinity of charged interfaces were observed, the exact energy relaxation pathway has remained unclear. Photon echo measurements revealed a pronounced inhomogeneity of the OH/OD stretching bands at low hydration levels that persists at least one order of magnitude longer than for bulk water pointing to reduced structural dynamics of surface-bound water molecules [39–41]. Time-resolved data of the bending mode of confined water have not been published.

Less information is available about dynamics of water interacting with phospholipid head groups or phosphate groups in other biomolecular systems. It was shown that the OD stretching absorption band of D₂O in weakly hydrated phospholipid multibilayers is inhomogeneously broadened and a tentative assignment of OD stretching frequencies to different water species was made. Generally, vibrational lifetimes decrease with increasing w_0 [42–44]. Anisotropy decays of the OD

stretching vibration of isotopically diluted water suggest reduced orientational relaxation of water molecules interacting with the phospholipid head group. The data was interpreted as a ‘wobbling in a cone’ that leaves hydrogen bonds intact during the experimental time window of 5 ps [45]. Recent advances in the field of time-resolved vibrational sum frequency generation may lead to additional information about structural dynamics of the hydration shell of fully hydrated phospholipids [46–48]. 2D IR spectroscopy of DNA hydration shells found structural fluctuations that are a factor of 3–5 slower than in bulk water [49] which is in agreement with molecular dynamics simulations [50].

In the following we will present the vibrational dynamics of the stretching and bending vibration of biologically relevant neat H_2O interacting with phospholipids. The use of reverse micelles allows for a precise control of the water content in order to study hydration shells of different size. Section 4.1 gives insight into the dynamic lineshape of the OH stretching vibration demonstrating an inhomogeneous distribution of water molecules up to hydration levels of $w_0 = 16$. Energy relaxation at all hydration levels proceeds via the OH bending vibration and further vibrational energy redistribution into small water pools occurs for $w_0 \geq 3$. In Sect. 4.2, we show the importance of librational modes as energy acceptors for OH bending vibrations and demonstrate how inter- and intramolecular energy relaxation are affected by the size of phospholipid hydration shells. The heat transport out of reverse micelles is briefly discussed in Sect. 4.3.

4.1 OH Stretching Dynamics: Energy Redistribution into Small Water Pools

Linear spectra of the OH stretching mode of water confined in DOPC reverse micelles are shown in Fig. 4.1. A significant broadening of the absorption band from $<300\text{ cm}^{-1}$ to 400 cm^{-1} (FWHM) is observed when w_0 increases from 1 to 16 with the spectrum for $w_0 = 16$ being similar to the one for bulk water. The maximum absorption frequency at low hydration levels is slightly red-shifted compared to the bulk-water case. Such shifts have been observed for neat and isotopically diluted (HOD in H_2O) water interacting with phospholipid multibilayers and assigned to the increasing relative amount of strong phosphate-water hydrogen bonds [45, 51]. Again, from linear spectroscopy the physical origin of the shape of the linear spectra, i.e., the underlying line broadening mechanisms, remain unclear and nonlinear spectroscopy is required for unraveling different contributions to the infrared lineshapes.

2D IR OH stretching spectra of water confined inside DOPC reverse micelles are presented in Fig. 4.2. At $T = 125\text{ fs}$ all spectra are dominated by a positive signal centered around a detection frequency of 3400 cm^{-1} caused by the $\nu = 0$ to 1 bleaching and stimulated emission contributions. A smaller red-shifted negative signal caused by the $\nu = 1$ to 2 excited state absorption appears to be weaker and is only partially detected due to the strong anharmonicity. At $w_0 = 1$ and 3, both

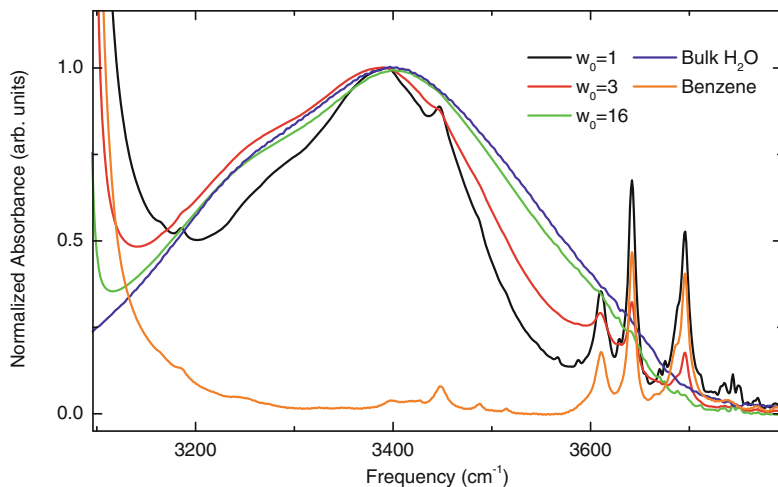


Fig. 4.1 Linear OH stretching absorption spectra of water confined inside DOPC reverse micelles for $w_0 = 1, 3$ and 16 . For comparison, the linear spectrum of bulk water is shown. The OH stretching absorption becomes narrower with decreasing water content and a slight redshift of the maximum absorption frequency is observed. Substructures in the case of $w_0 = 1$ and 3 are caused by the benzene solvent (*orange line*) (color figure online)

contributions decay with increasing population time. For $w_0 = 16$, in contrast, the positive signal rises after 300 fs accompanied with the growth of a new negative signal at a detection frequency around 3600 cm^{-1} .

Blue lines in Fig. 4.2 represent center lines as a measure of the current 2D spectral shape. Population time-dependent center line slopes suggest a strong w_0 -dependence of spectral-diffusion time constants. As is obvious from the 2D spectra, the correlation between excitation and detection frequencies is largely preserved at $w_0 = 1$ up to $T = 1500$ fs whereas such memory effects are absent for spectra measured for $w_0 = 16$ at $T = 500$ fs. It should be noted that spectral diffusion in neat water caused by the highly fluctuating nature of the hydrogen-bond network (bottom row of Fig. 4.2, reproduced from [31]) is significantly faster than for water confined in DOPC reverse micelles at all hydration levels presented here.

In order to extract spectral diffusion rates, the center line slope (CLS) as a function of population time is plotted in Fig. 4.3. The CLS for all hydration levels is 0.7 ± 0.1 at $T = 125$ fs. After a moderate decay, the value for $w_0 = 1$ levels off at a value of approximately 0.6. Contrarily, the slopes for $w_0 = 3-8$ decay on a time scale of 400–500 fs (cf. Table 4.1). The uncertainty of such decay times is in the range of 20 % due to the limited number of points to be used for the fits. Within our experimental accuracy, the spectral reshaping rates of the OH stretching band are constant in the range of $w_0 = 3-8$. Faster spectral diffusion at $w_0 = 16$ as observed in the 2D spectra (Fig. 4.2) is manifested in a quick CLS decay with a time constant of 250 fs. The reshaping dynamics at all hydration levels differ significantly from the behavior of bulk water for which the CLS has a value of 0.25 at $T = 100$ fs indicating much

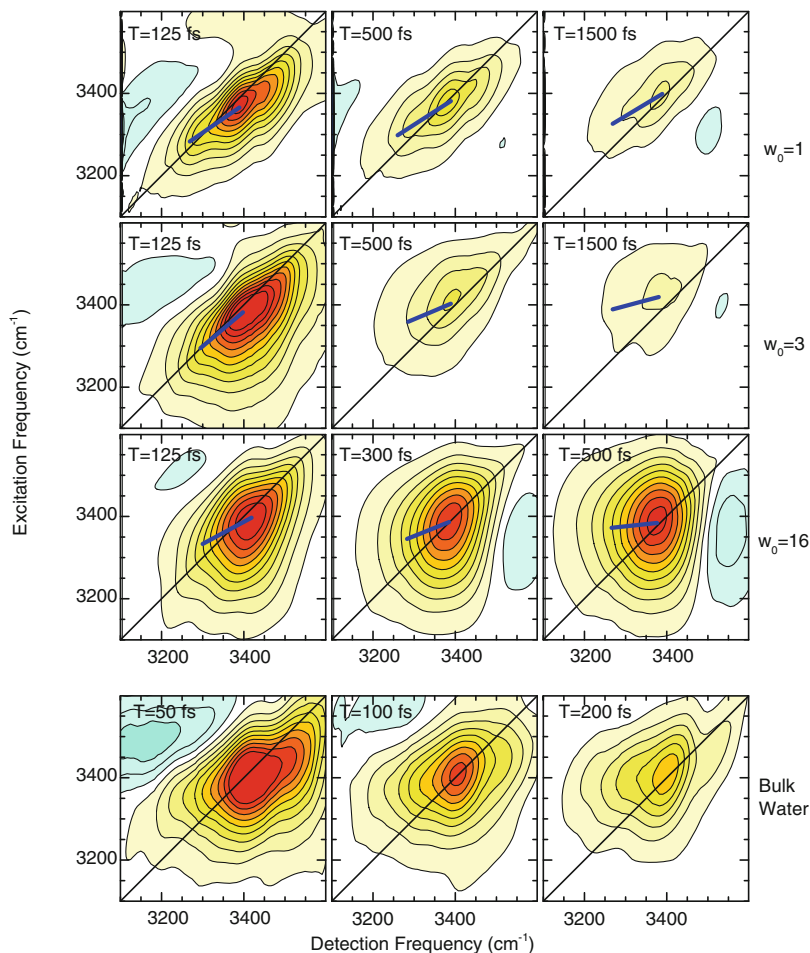


Fig. 4.2 2D IR spectra of the OH stretching vibration of water confined inside DOPC reverse micelles. The spectra for a range of w_0 between 1 and 16 are shown for the population times T indicated. *Blue lines* represent the center lines whose slopes are used to trace the dynamics of spectral reshaping. For comparison, the last row shows 2D IR spectra of the OH stretching vibration of neat water (reproduced from [31]). All spectra were measured with pulses of parallel linear polarization. Minor reshaping occurs in the case of $w_0 = 1$ whereas spectra at $w_0 = 16$ experience a quick loss of the correlation between excitation and detection frequencies on a 300 fs time scale. Such spectral diffusion is accompanied by the rise of a homogeneous signal at detection frequencies in a range around 3600 cm^{-1}

higher spectral-diffusion rates when a water molecule is embedded in an extended water hydrogen-bond network.

Broad band pump-probe spectra for population times up to 3 ps are plotted in Fig. 4.4. Such spectra clearly show an enhanced absorption at low frequencies around 3000 cm^{-1} indicating the existence of a very broad $v = 1$ to 2 excited state absorption.

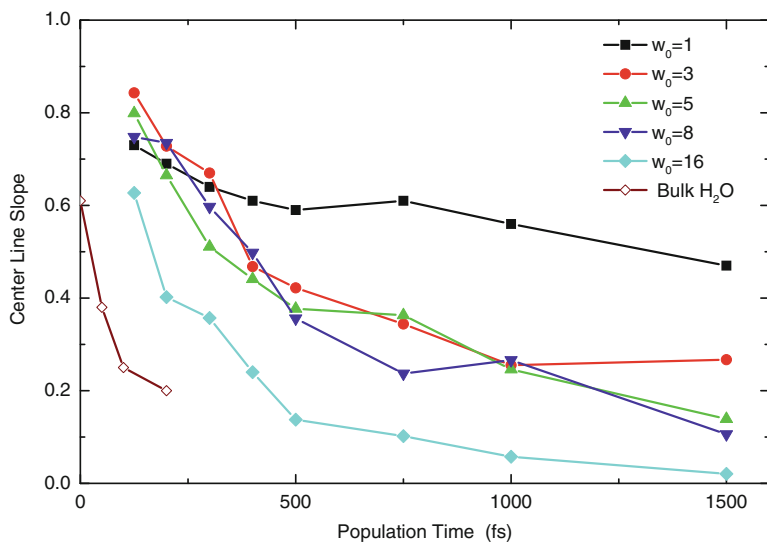


Fig. 4.3 Center line slope of the *blue lines* in Fig. 4.2 as a function of population time (color figure online)

Table 4.1 Exponential decay times of fits to the spectral reshaping of the OH stretching band as measured by decays of center line slopes of 2D spectra (T_{CLS}) and first moments of pump-probe spectra (T_{FM}). T_1 lifetimes were determined by pump-probe measurements mapping the decay of the excited state absorption

w_0	T_{CLS} (fs)	T_{FM} (fs)	T_1 (fs)
1	>1500ps	>1000	530
3	400		420
5	380		
8	460	530	
16	250	310	330

Note that the decay of this contribution becomes significantly faster with increasing w_0 . At $w_0 = 1$ and 3, negative absorbance change signals at 3400 cm^{-1} decay slower than the excited state absorption and a rise is observed for $w_0 = 16$ indicating that the time evolution at this frequency position is influenced by vibrational energy redistribution of the initial OH stretching excitation. This picture is further supported by a rising positive signal contribution at high probe frequencies of about 3600 cm^{-1} similar to the one in the 2D spectra.

The negative absorbance-change contribution of the pump-probe spectra exhibits a significant reshaping with population time. In order to follow the corresponding dynamics, the first moment of the transient spectra

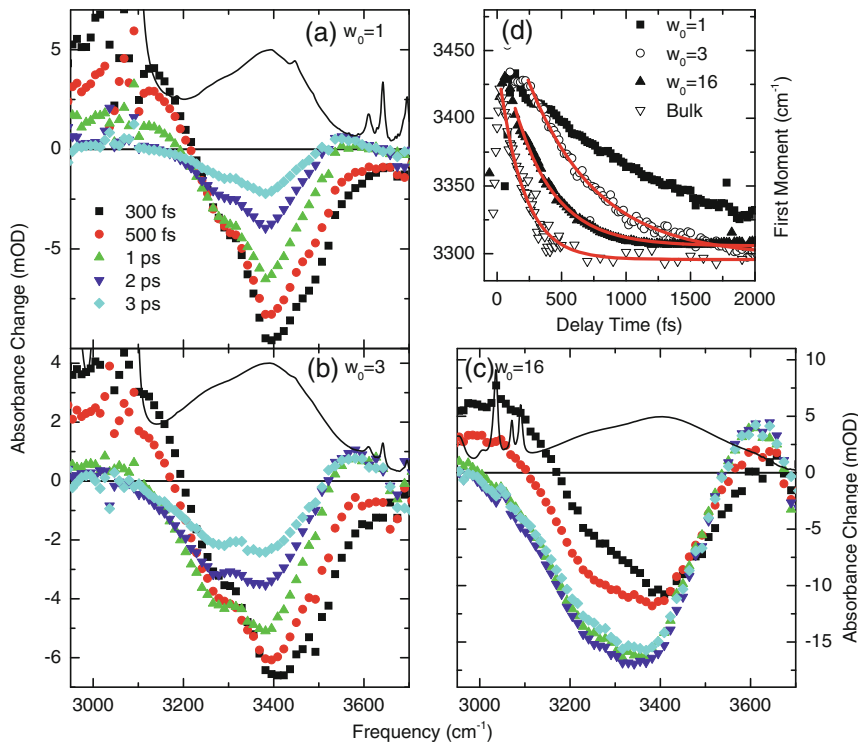


Fig. 4.4 a–c Transient pump-probe spectra of the OH stretching vibration of water confined in DOPC reverse micelles for $w_0 = 1, 3$ and 16 . Linear spectra are indicated with *solid lines*. All transients were measured with parallel linear polarizations of pump and probe pulses and a weak benzene response was subtracted for $w_0 = 1$ and 3 . The decay of the enhanced-absorption signal at 3000 cm^{-1} demonstrates increased relaxation rates with increasing w_0 . The decays are accompanied by a rise of a positive signal at 3600 cm^{-1} for $w_0 = 3$ and 16 . As in the 2D spectra the bleaching contribution is subject to a reshaping that is quantified by calculating its first moment **d**. Single exponential fits (*red lines*) with time constants of $530, 310$ and 200 fs for $w_0 = 3, 16$ and bulk water indicate similar time scales of reshaping as the CLS decays do for the 2D spectra (color figure online)

$$\text{FM}(T) = \frac{\int \nu_{Pr} \Delta A(T, \nu_{Pr}) d\nu_{Pr}}{\int \Delta A(T, \nu_{Pr}) d\nu_{Pr}} \quad (4.1)$$

as a function of the population time T was extracted. The first moment was calculated between 3220 and 3610 cm^{-1} for $w_0 = 1$ and between 3180 and 3640 cm^{-1} for $w_0 = 3$ to observe the reshaping of the $\nu = 0$ to 1 transition only. At $w_0 = 16$ we chose a variable lower frequency boundary corresponding to the zero-crossing points of the absorbance change to avoid cutting of large parts of the bleaching contribution. The upper boundary was kept fixed at 3520 cm^{-1} so that the influence of the rising enhanced-absorption signal was minimized. The result of the calculations presented in Fig. 4.4d suggests a redshift of the bleaching component from >3400 to

3300 cm^{-1} . The time scale of such shifts depends on the water content in the system. While reliable fitting for the FM of $w_0 = 1$ is impossible because of the unknown limiting value ($T \rightarrow \infty$), the other traces fit well to single exponential decays of 530 fs ($w_0 = 3$), 310 fs ($w_0 = 16$) and 200 fs (bulk). Those constants are slightly higher than the ones obtained by the CLS analysis of the 2D spectra (cf. Table 4.1) but show a similar decrease with hydration. It should be emphasized that the origin of the reshaping may be the same for both techniques but only 2D IR spectroscopy allows insight into the underlying lineshape dynamics. Pump-probe spectra could simply be interpreted as shifts of transient signals whereas 2D spectra clearly demonstrate a transition from inhomogeneous to homogeneous lineshapes.

Further information about OH stretching dynamics is revealed by a kinetic analysis of polarization-resolved pump-probe data at fixed frequency positions presented in Fig. 4.5. The $v = 1$ lifetimes are extracted from the isotropic excited state absorption decay measured at 3005 cm^{-1} (cf. Fig. 4.5a). Single exponential fits of the transients starting at $T = 260$ fs to avoid the influence of coherent pump-probe coupling give lifetimes of 530, 420 and 330 fs for $w_0 = 1, 3$ and 16, respectively, confirming the impression of enhanced relaxation at high hydration levels obtained by the 2D and pump-probe spectra. The negative component at 3395 cm^{-1} (cf. Fig. 4.5b) decays on a slower 1.5–2 ps time scale for $w_0 = 1$ and 3 whereas an increase occurs for $w_0 = 16$ up to 1.5 ps followed by a decay that is significantly slower than the one for low hydration levels. Note that this increase correlates with the rise of the enhanced absorption signal at 3636 cm^{-1} presented in Fig. 4.5d pointing to the fact that transient spectra measured at $w_0 = 16$ are strongly dominated by energy redistribution in the system. Transients for $w_0 = 1$ and 3 indicate that the signal rise becomes slower and less pronounced with decreasing water content.

The anisotropies plotted in Fig. 4.5c are distorted by the coherent artifacts around zero delay time. However, a clear deviation from the value of 0.4 at $T = 500$ fs suggests a partial depolarization of the signals on an ultrafast time scale of <300 fs. The asymptotic anisotropy values decrease with increasing hydration, i.e., they reach a value of ≈ 0.25 for $w_0 = 1$, 0.15 for $w_0 = 3$ and 0.05 for $w_0 = 16$. The uncertainty for these values is 0.1 so that within the accuracy of the measurement, one finds a total loss of anisotropy for $w_0 = 16$.

4.1.1 Vibrational Relaxation to the Bending Mode

The kinetic analysis proves that OH stretching relaxation rates decrease for decreasing values of w_0 . This finding is in agreement with previous studies of water at charged interfaces of AOT reverse micelles [35–37]. It is known for bulk water that the stretching vibration relaxes via the OH bending overtone [28]. Increased lifetimes at low values of w_0 in AOT reverse micelles were assumed to arise from an exclusion of the bending vibration from the energy relaxation pathway due to a shift of the OH stretching absorption spectrum, resulting in a slower energy transfer to hydrogen-bond or AOT modes [35, 37]. The OH bending overtone ($v = 0$ to 2 transition) has a frequency position of $\approx 3250\text{ cm}^{-1}$. Note that the linear absorption

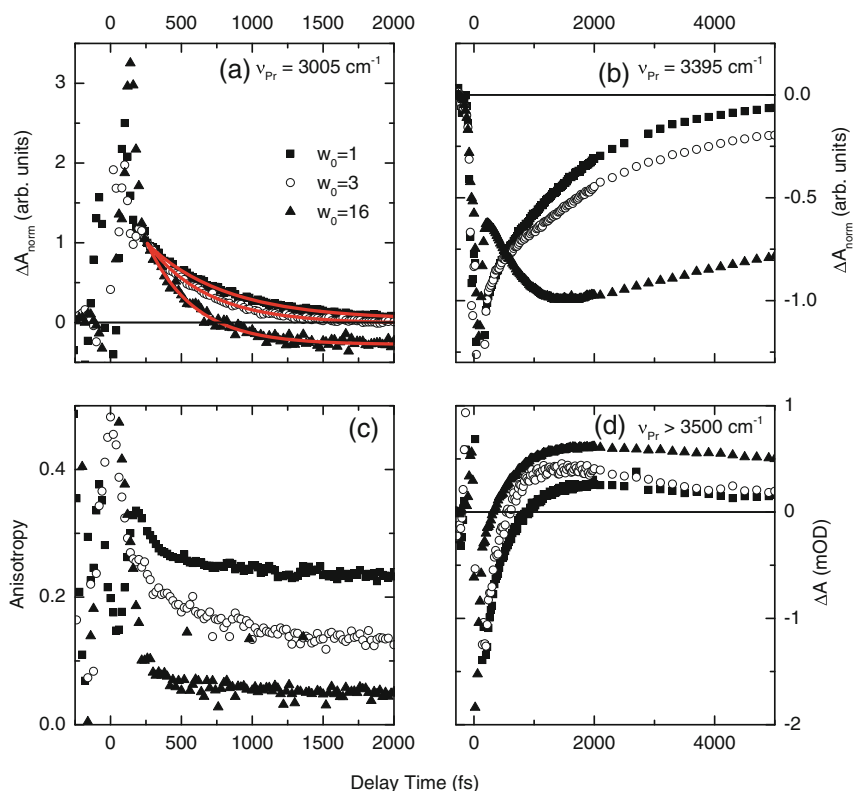


Fig. 4.5 Pump-probe kinetics of the OH stretching vibration of water confined in DOPC reverse micelles for $w_0 = 1, 3$ and 16 . **a** Normalized isotropic transient absorbance change mapping the excited state absorption decay at a probe frequency of 3005 cm^{-1} (symbols). Monoexponential fits (red lines) with time constants of 530 fs ($w_0 = 1$), 420 fs ($w_0 = 3$) and 330 fs ($w_0 = 16$) demonstrate the hydration dependence of the vibrational lifetime. **b** Transients taken at the maximum of the bleach signals at 3395 cm^{-1} . Signals for $w_0 = 1$ and 3 decay monotonically while a delayed rise occurs at $w_0 = 16$ after a fast initial decay. **c** Anisotropy decays at $\nu_{Pr} = 3395\text{ cm}^{-1}$: An almost constant level of 0.25 and 0.15 are found for $w_0 = 1$ and 3 after 500 fs . Anisotropies of $w_0 = 16$ are close to zero for $T > 300\text{ fs}$. **d** Transients taken at high frequencies ($w_0 = 1$: 3535 cm^{-1} , $w_0 = 3$: 3550 cm^{-1} , $w_0 = 16$: 3636 cm^{-1}) monitor the rise of the hot ground state signal. Data for $w_0 = 16$ are divided by 8 for better comparison (color figure online)

spectra at all hydration levels in DOPC reverse micelles (cf. Fig. 4.1) have a shoulder at this frequency position that indicates a significant spectral overlap opening the opportunity for efficient energy relaxation.

Figure 4.6 shows the transient OH bending response around 1650 cm^{-1} after OH stretching excitation with pump pulses centered at 3400 cm^{-1} for $w_0 = 1$. In this case, the weakest overlap between the OH stretching mode and the OH bending overtone would be expected from an inspection of the linear spectra. Transient spectra (Fig. 4.6a) are comprised of negative and positive signal contributions around

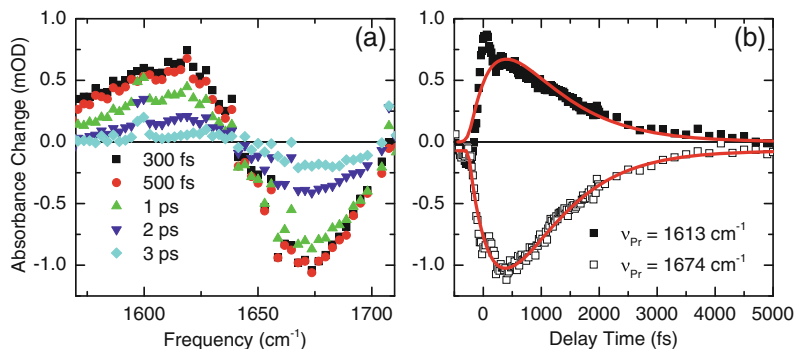


Fig. 4.6 Two-color pump-probe data of the $w_0 = 1$ OH bend response after OH stretching excitation with pump pulses centered at 3400 cm^{-1} . **a** Transient spectra are similar at delays of 300 and 500 fs and show a slow decay at longer delay times. **b** The time evolution at 1613 and 1674 cm^{-1} demonstrates that such a behavior is caused by a delayed rise of the OH bending response. Biexponential fits convoluted with the 150 fs time resolution yield rise and decay times of 500 and 800 fs, respectively, that are assigned to the OH stretching and OH bending lifetimes at this hydration level

1675 and 1615 cm^{-1} caused by the usual $\nu = 0$ to 1 and 1 to 2 transitions, respectively. Obviously, the data at $T = 300$ and 500 fs are almost identical in terms of amplitude. The time-dependent transient absorbance change taken at fixed probe frequency positions of 1613 and 1674 cm^{-1} (Fig. 4.6b) illustrates that the bending response shows a delayed rise. Coherent pump-probe couplings in the time traces are less pronounced than in the data shown before due to the use of 500 nm thick silicon nitride windows with a negligible signal contribution. Therefore, fitting of the transients around zero delay time becomes feasible. Results of a biexponential fitting model convoluted with the finite 150 fs time resolution of the experiment reveal that the transient bending response consists of a delayed rise with a 500 fs time constant and a subsequent decay on an 800 fs time scale. The rise time exactly matches the OH stretching lifetime at $w_0 = 1$ and proves that the initial OH stretching excitation is predominantly transferred to the OH bending mode at this hydration level. The decay with an 800 fs time constant is due to the following de-excitation of the bending vibration with intermolecular librations serving as energy acceptors. Note that the bulk water bending lifetime of 170 fs is significantly shorter. This issue will be discussed in detail in Sect. 4.2.

Increasing the water content leads to a reshaping of the OH stretching absorption band toward the bulk water spectrum (cf. Fig. 4.1) so that an enhanced overlap of the bending overtone with the OH stretching fundamental leads to more efficient energy relaxation. Additionally, spectral diffusion can bridge the frequency gap between the $\nu = 1$ of the OH stretching and the $\nu = 2$ of the OH bending mode for oscillators in the blue part of the OH stretching absorption spectrum. Therefore, increasing structural fluctuations with increasing water pool size are another source for the concomitant increased OH stretching relaxation rates.

4.1.2 2D Lineshapes as Probes for Energy Redistribution

Despite the lack of spectral diffusion in the case of $w_0 = 1$, the corresponding 2D spectra are not purely inhomogeneously broadened. The initial ($T = 125$ fs) CLS value of approximately 0.7 points to a significant homogeneous contribution to the total lineshape, caused e.g., by lifetime broadening. If the dephasing rates were dominated by lifetime broadening, one would obtain $1/T_2 = 1/(2T_1) \approx 1 \text{ ps}^{-1}$ causing a homogeneous linewidth of $\Delta\nu_{hom} = 1/(\pi c T_2) \approx 10 \text{ cm}^{-1}$ which is clearly smaller than the antidiagonal line width of 70 cm^{-1} . Hence, there must be other contributions to the homogeneous linewidth such as anharmonic coupling and energy transfer between the OH stretching oscillators. Moreover, due to the spectral bandwidth of the pulses, a coherent superposition of both oscillators can be prepared. Intramolecular energy transfer between the OH stretching modes would cause a dephasing of the initially excited vibration. This process must be accompanied by a depolarization of the emitted electric field due to the different orientation of the two oscillators involved (the angle between the dipoles of symmetric and antisymmetric stretching vibrations in a normal mode picture is 90°). Such an expectation is supported by the ultrafast anisotropy decay observed for $w_0 = 1$ to a finite value of approximately 0.2 (Fig. 4.5c). Similar anisotropy decays were found for water forming weaker hydrogen bonds with acetonitrile where the splitting of the OH stretching absorption band into symmetric and antisymmetric modes is clearly visible [52, 53]. The corresponding ultrafast change of the mode character on a roughly 250 fs time scale contributes to the dephasing time with $1/T_2 = 1/T_2^* + 1/2T_1 = 1/200 \text{ fs}^{-1}$ resulting in a homogeneous linewidth of $\approx 53 \text{ cm}^{-1}$. This value is similar to the antidiagonal linewidth observed in the 2D spectra. A more appropriate lineshape analysis as presented in Sect. 3.1 requires knowledge about the frequency fluctuation correlation function including effects of anharmonic couplings and dephasing as well as structural fluctuations of lipid head groups. Such a detailed theoretical treatment is out of the scope of this thesis. However, molecular dynamics simulations combined with density functional theory can use the experimental results described here as a benchmark to obtain a more complete picture of water-lipid interactions on ultrafast time scales.

It is known e.g., for bulk water that energy of OH stretching excitations is quickly redistributed to low-frequency intermolecular hydrogen-bond modes ultimately resulting in a macroscopic sample heating. Microscopically, hydrogen bonds become weaker and/or break leading to a characteristic blueshift of the linear OH stretching spectra [20]. Time-resolved vibrational spectroscopy detects such shifts as differential absorption that is observed at late population times. Signal contributions at high probe frequencies as shown in Fig. 4.5d are helpful in mapping the energy redistribution as they are not masked by signals of the initial OH stretching excitation. While the OH stretching mode gets de-excited during the vibrational lifetime, elevated temperatures in the excited sample volume persist for longer time scales until cooling due to heat diffusion is completed. The long-lived transient signals are therefore often referred to as *hot ground state* signals.

2D spectra of the OH stretching vibration and the associated CLS analysis demonstrate that the spectral diffusion rates for values of w_0 between 3 and 8 are similar to the vibrational lifetimes, i.e., there is a correlation between energy relaxation and the spectral reshaping. Energy deposited in the OH stretching vibration quickly relaxes to the bending modes followed by energy redistribution into intermolecular modes. As such, water molecules in the proximity of the initial OH stretching vibration get affected and contribute to the hot ground state. That is, the correlation between the excitation and detection frequencies is lost because the hot ground state is associated to a large number of molecules that were not excited initially. As a result, this signal is expected to have a homogeneous lineshape which is clearly true for the rising 2D signal at detection frequencies around 3600 cm^{-1} (blue contours). Spectral diffusion observed on the $\nu = 0$ to 1 transition is therefore attributed to the rise of the hot water ground state.

Spectral diffusion is negligible at $w_0 = 1$ where single water molecules are hydrogen bonded to the phosphate or carbonyl groups of the phospholipid head groups. In such a case, excess energy of the OH stretching excitation has to be accepted by phospholipid vibrations. Large water-water distances prevent the formation of water hydrogen bonds so that a collective hot ground state is not expected. The observation of spectral diffusion for $w_0 \geq 3$ suggests that very small water pools are formed already at low hydration levels of $w_0 = 3$. Such small water pools act as efficient heat sinks for OH stretching excitations in a similar way as for phosphate excitations. Up to a value of $w_0 = 8$, the spectral diffusion rates remain almost constant indicating that increased hydration levels increase the pool size without introducing significant changes of the hydrogen-bond dynamics. This behavior is in line with the phosphate and carbonyl groups being hydrated by 6–8 water molecules (cf. Sect. 1.1).

A further increase of w_0 leads to faster spectral diffusion. This is partly caused by the shorter vibrational lifetimes at high hydration levels resulting in faster energy redistribution and a faster formation of the hot ground state signature. Remarkably, $w_0 = 16$ is the only hydration level for which the CLS decay is faster than vibrational relaxation (cf. Table 4.1) pointing to other dynamic processes such as structural fluctuations of the hydrogen-bond network. It should be emphasized that the OH stretching dynamics represent an ensemble average of water molecules interacting with the head groups and a more bulk-like part in the interior of the reverse micelles. Phosphate vibrational dynamics discussed in Sect. 3.1 are true interfacial probes and have shown that the phosphate-water hydrogen-bond geometry, i.e., the first layer of hydration, is rigid on a time scale of 10 ps. Therefore, structural fluctuations of water must be assigned to molecules in the intramicellar pool not directly interacting with the phospholipid head groups.

Structural fluctuations of the hydrogen-bond network on a 100 fs time scale are the major source for spectral diffusion in bulk water [30, 31]. Such an ultrafast memory loss is absent for hydration shells of phospholipids up to a value of $w_0 = 16$ demonstrating that the embedding of water molecules in the strong electrostatic potential of lipid head groups leads to a significant change of structure and dynamics of the hydrogen-bond network. While structural fluctuations are only of little importance for the interpretation of the 2D OH stretching spectra they cannot be excluded

categorically. In fact, the pump-probe kinetics (and the CLS decays at $w_0 = 16$) suggest that the spectral diffusion rates caused by such fluctuations increase with the hydration level.

In conclusion, a detailed analysis of 2D IR and pump-probe data reveals that the OH stretching vibration relaxes via the OH bending vibration for hydration shell water of phospholipids. Small water pools around the lipid head groups form already at hydration levels as small as $w_0 = 3$. Such water pools act as efficient heat sink modifying the energy relaxation pathway in a way that energy acceptance by the lipids is less probable. A similar result was obtained from the phosphate dynamics where the ratio of the biexponential decay amplitudes (cf. Table 3.2) increases most significantly when w_0 is raised from 1 to 3. If the vibrational energy of phosphate excitation was accepted by the water pool as claimed before, a clear experimental signature of a hot water ground state must be observable.

4.1.3 Small Water Pools as Heat Sinks for Intramolecular Vibrations

A proof for the existence of such signals at a value of $w_0 = 3$ is given in Fig. 4.7 that shows hot ground state signals in analogy to the ones of the antisymmetric phosphate stretching vibration shown in Fig. 3.12 (p. 63). Again, the differential absorption of temperature-dependent linear spectra as well as long-term signals after excitation of the antisymmetric phosphate stretching and OH stretching vibration appear to be similar (Fig. 4.7b). The comparison verifies that small water pools are the primary energy acceptors for water and phosphate stretching excitations, i.e., vibrational energy deposited in intramolecular modes of water and the phosphate groups is quickly redistributed into intermolecular modes of the water pool. This process is manifested in the delayed rise of the hot ground state signals as shown in Figs. 4.5d and 4.7c on a time scale that directly reflects the lifetimes of modes involved in the energy relaxation pathway.

There is another mechanism for direct intermolecular OH stretching energy redistribution within the water pool as is evident from the anisotropy decays that become more efficient with increasing hydration. It is known for bulk water that the strong transition dipole moments lead to resonant excitation transfer between adjacent water molecules [32]. Such an intermolecular energy transfer should also occur as soon as water pools form around the phospholipid head groups. This hopping of excitation results in a depolarization of pump-probe signals, i.e., an anisotropy decay, according to the relative orientation of OH stretching dipoles. As discussed before for $w_0 = 1$, the anisotropies (Fig. 4.5c) show an initial fast decay due to energy transfer between the two OH stretching modes of one water molecule. Since structural fluctuations are of minor importance, the additional anisotropy decay for $w_0 \geq 3$ is assigned to resonant energy transfer between water molecules. As such, the anisotropy decays represent another indication of small water pools around phospholipid polar head

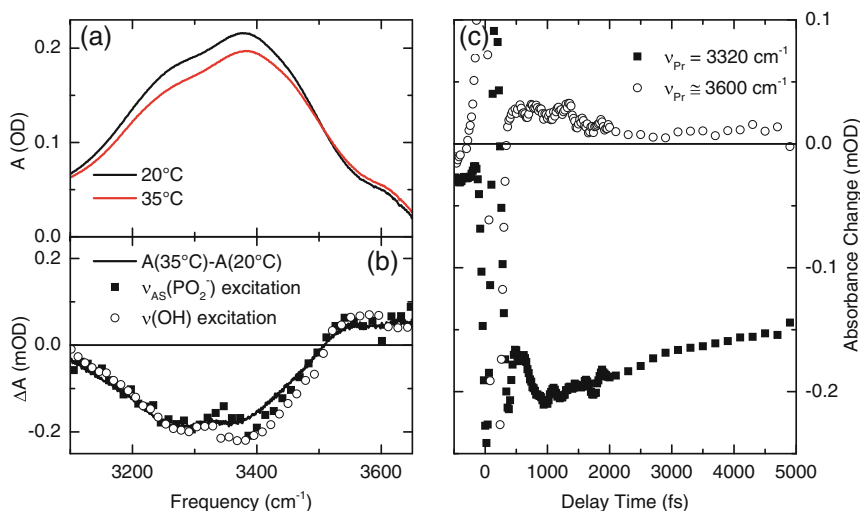


Fig. 4.7 Response of the OH stretching vibration to heating. **a** Temperature-dependent linear spectra for $w_0 = 3$ at $T_{sample} = 20^\circ\text{C}$ and 35°C . A temperature increase leads to weakening of hydrogen bonds that causes a blueshift of the OH stretching vibration as represented by the scaled differential spectrum in **b**. Additionally, transient spectra 1 ps after excitation of $\nu_{AS}(\text{PO}_2^-)$ (solid squares) and 3 ps after excitation of the OH stretching vibration (divided by 10, open circles) are shown. **c** The transient hot ground state signal rises during the first picosecond after $\nu_{AS}(\text{PO}_2^-)$ excitation. Transients between 3550 and 3650 cm^{-1} were averaged for the positive contribution to obtain a better signal-to-noise ratio

groups that form as soon as 3 water molecules per lipid are present. An increase of the pool size results in a larger variety of water orientations so that a randomization of the initial polarization becomes more probable. This is demonstrated by the total anisotropy loss at $w_0 = 16$.

In the case of water, the intramolecular energy redistribution pathway is known. The two-color data presented in Fig. 4.6 demonstrates energy redistribution from the stretching to the bending mode from where it is expected to relax via the librations. Interestingly, the vibrational lifetime of the bending mode at a level of $w_0 = 1$ was determined to have a value of 800 fs, i.e., the vibrational relaxation rate is 4 times smaller than for bulk water. The bending vibration is the lowest-energy intramolecular vibration of water. Hence, vibrational energy has to be accepted by intermolecular modes that are intimately connected with the hydrogen-bond structure. Time-resolved pump-probe measurements of the OH bending vibration in different reverse micellar systems are helpful in deciphering different contributions to the OH bending relaxation rate. In this way, the next section will explain the strong hydration dependence of the corresponding vibrational lifetime.

4.2 OH Bending Dynamics: Energy Relaxation into Intermolecular Modes

Figure 4.8 summarizes pump-probe data of the OH bending vibration of water in DOPC reverse micelles obtained by pumping the fundamental transition with pulses centered around 1650 cm^{-1} . The bleach and stimulated emission on the $\nu = 0$ to 1 transition results in a negative absorbance change around this frequency position whereas the positive signal caused by the anharmonically red-shifted $\nu = 1$ to 2

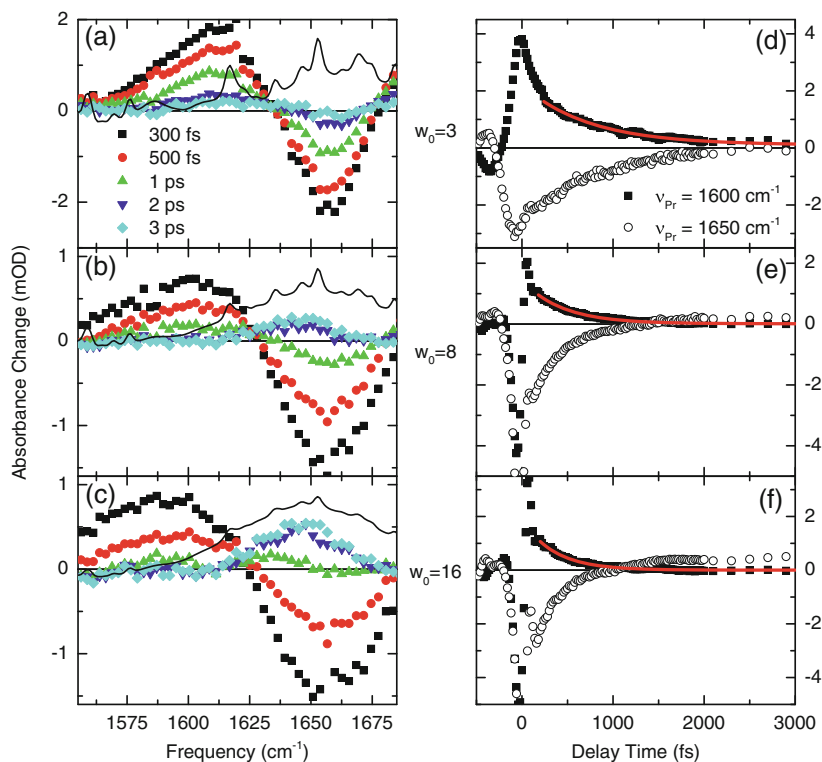


Fig. 4.8 Pump-probe data of the OH bending vibration of water confined in DOPC reverse micelles measured with parallel linear polarizations of pump and probe pulses centered around the maximum of the OH bending absorption spectrum at 1650 cm^{-1} . **a–c** Transient spectra for $w_0 = 3, 8$ and 16 (symbols) and the corresponding linear absorption (lines). Substructures in the steady state spectra are caused by benzene. The weak benzene response was subtracted from the time-resolved data for $w_0 = 3$. At early delay times, spectra at all hydration levels show the typical shape consisting of a negative contribution on the fundamental transition and an anharmonically red-shifted positive signal on the $\nu = 1$ to 2 transition. At $T > 1$ ps, a positive signal grows in around 1650 cm^{-1} indicating the rise of a hot ground state that gains in importance with increasing w_0 . **d–f** Corresponding time evolution at the two frequency positions of maximum (1600 cm^{-1}) and minimum (1650 cm^{-1}) absorbance change

Table 4.2 Monoexponential decay times from fits of the positive absorbance change signal of the water bending vibration in DOPC, AOT and Brij-30 reverse micelles (red lines in Figs. 4.8, 4.10 and 4.11). The value for $w_0 = 1$ was determined indirectly through the OH bend response after OH stretching excitation (cf. Sect. 4.1.1)

w_0	τ_{DOPC} (fs)	τ_{AOT} (fs)	$\tau_{Brij-30}$ (fs)
1	800		
2			400
3	730	615	
8	440	440	250
16	345	345	

absorption is found at 1600 cm^{-1} (Fig. 4.8a–c). A significant broadening is observed with increasing w_0 and a slight redshift of the order of 10 cm^{-1} occurs for the zero-point between the two signal contributions. Such shifts may result from the increased fraction of weaker water-water hydrogen bonds compared to the low-hydration case when water is preferentially hydrogen bonded to the lipid’s phosphate and carbonyl groups. At late delay times ($T > 1\text{ ps}$) an enhanced absorption feature around 1650 cm^{-1} builds up for $w_0 = 8$ and 16. The amplitude of the delayed rise increases with w_0 , a behavior reminiscent of the OH stretching hot ground state discussed before. The hot ground state signature of the OH bending vibration is known from pump-probe data of bulk water [24] and matches the shape observed at high hydration levels in the DOPC reverse micelles. We conclude that energy deposited in the OH bending vibration is redistributed among intermolecular modes in the water pool in consistence with the conclusions drawn in the previous section.

The time-dependent absorbance change at two fixed frequency positions is plotted in Fig. 4.8d–f. Transients taken at 1600 cm^{-1} (solid squares) monitor $v = 1$ population decay and monoexponential fits (red lines) give the corresponding T_1 lifetimes of the OH bending vibration. The results summarized in Table 4.2 show a clear increase of the OH bending lifetime from $\approx 350\text{ fs}$ at $w_0 = 16$ to $\approx 700\text{ fs}$ at $w_0 = 3$ with the latter approaching the 800 fs lifetime for $w_0 = 1$ as determined by the transient bending response after stretching excitation. Note that the value determined for high hydration levels of $w_0 = 16$ is longer than the $170\text{--}260\text{ fs}$ lifetime reported for bulk water [21, 22, 24].

MD simulations found a prominent role of the librational water modes as energy acceptors of OH bending excitations [25, 26]. They determined a lifetime of 270 fs with $2/3$ of the relaxation rate arising from energy relaxation to librational modes of the same water molecule. $1/3$ of the relaxation rate originates from intermolecular energy transfer to the water’s first hydration shell, i.e., the 4 nearest neighbors. Intramolecular energy relaxation depends in a decisive way on the fluctuating force $f(t)$ the librations exert on the axis of the bending vibration. The intramolecular vibrational relaxation rate at the fundamental bending frequency $W_{intra}(\nu_{01})$ is connected to the time correlation function of the fluctuating force by:

$$W_{intra}(\nu_{01}) \propto |H_{cen}|^2 \int_{-\infty}^{\infty} dt \langle f(t)f(0) \rangle e^{-i2\pi\nu_{01}t} \quad (4.2)$$

Here, H_{cen} is the centrifugal coupling matrix element taken between the $\nu = 1$ and $\nu = 0$ states of the bending vibration. According to Eq. 4.2, the relaxation rate is determined by the Fourier amplitude of the fluctuating force at the fundamental frequency if one assumes the coupling matrix element to be constant.

The L2 band of water librations causes a broad infrared absorption centered at $\nu_{L2} \approx 670 \text{ cm}^{-1}$ significantly lower than the bending fundamental frequency. However, there are librational over- and combination tones at around $2\nu_{L2}$. The overtone of high frequency librations at 800 cm^{-1} corresponding to hindered vibrations around the axis with the lowest moment of inertia (x -axis in Fig. 4.9b) participates in a Fermi resonance with the bending mode thereby establishing an efficient energy relaxation pathway of bending excitations. Hydrogen bonding is responsible for the existence of librational modes of water in the condensed phase. Thus, modifications of the hydrogen-bond geometry of a water molecule can be expected to cause changes in the librational frequencies [54]. Bending relaxation rates are strongly determined by those frequency positions and are therefore sensitive probes for local hydrogen-bond geometries.

The increasing OH bending relaxation rates at low hydration levels in DOPC reverse micelles may be caused by a shift of librational frequencies. Unfortunately, there is no information about low-frequency vibrations of phospholipid hydration-shell water. However, THz absorption spectra of the related AOT reverse micelles are available [55, 56] (cf. Fig. 4.9a). While reverse micelles with $w_0 = 40$ resemble

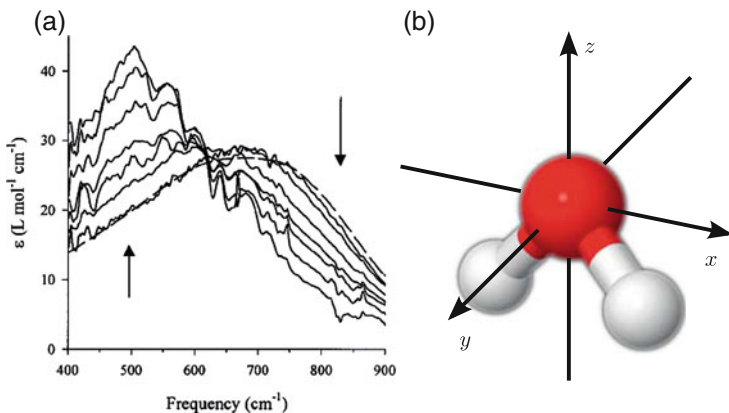


Fig. 4.9 **a** Molar extinction coefficient ϵ of bulk water (*dashed line*) and water confined in AOT reverse micelles (*solid lines*, the arrows indicate the progression of spectra measured for $w_0 = 40, 20, 10, 6, 4, 2, 1$) taken from [55]. The spectral redshift illustrates decreasing librational frequencies when water is removed from the reverse micelles. **b** Water molecule with the principle axes around which librations occur. The x -axis librations are the main energy acceptors for OH bending excitations (color figure online)

the bulk water spectrum with a maximum at 670 cm^{-1} , a gradual redshift of the peak towards 500 cm^{-1} at a value of $w_0 = 1$ is observed. Decreasing transition frequencies are a sign for a softening of the librational potential due to a reduced restoring force, i.e., rotations of the water molecules become less restricted compared to the bulk. Such a behavior has been assigned to the highly perturbed hydrogen-bond network structure of head-group bound water molecules that is determined by electrostatic interactions of water with the ionic head groups and reduced water-water hydrogen bonding [57]. Due to a similar molecular structure, one expects very similar changes in the librational absorption of water in DOPC reverse micelles. A markedly different situation occurs for non-ionic surfactant molecules in which electrostatic interactions play a minor role. THz absorption spectra of reverse micelles containing the non-ionic surfactant Brij-30 remain similar to the librational absorption of bulk H_2O at all hydration levels [56]—a result that is confirmed by molecular dynamics simulations [58]. It is instructive to use the two extreme cases with the known L2 absorption band as a benchmark for comparison with OH bending relaxation in DOPC reverse micelles described above.

Figure 4.10 shows pump-probe data of the water bending vibration in AOT reverse micelles (dispersed in the solvent CCl_4) measured under the same conditions as for

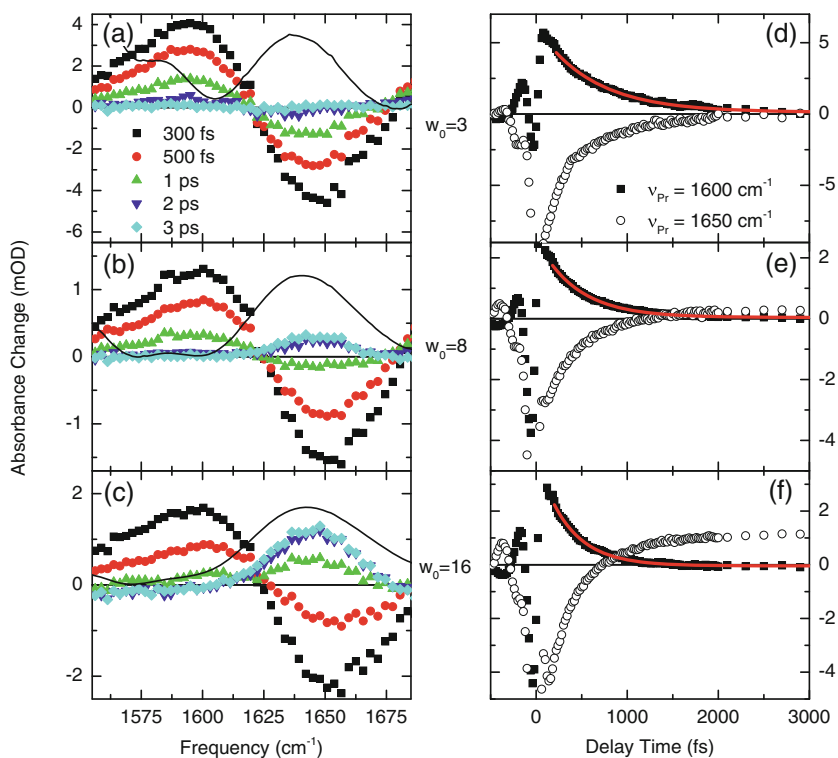


Fig. 4.10 Same as in Fig. 4.8 for the bending vibration of water confined in AOT reverse micelles (solvent CCl_4). The similarities of the transients in both cases point to identical relaxation pathways

DOPC (Fig. 4.8). Generally, a strong similarity between the two cases is found for both spectral shape and decay of the time-resolved data. As is evident from Table 4.2, the relaxation rates at $w_0 = 8$ and 16 are identical in DOPC and AOT reverse micelles. Increasing lifetimes with decreasing w_0 are also found for AOT with the value at $w_0 = 3$ being slightly smaller than for DOPC. Care must be taken not to overinterpret the different time constants since the uncertainty for w_0 is $\Delta w_0 \approx 1$. Infrared absorption spectra of the OH stretching vibration indicate a slightly larger water content for AOT. Hence, it is concluded that the OH bending lifetimes for similar water content in the two different systems agree within the accuracy of the measurement.

OH bending pump-probe data for water in Brij-30 reverse micelles (dispersed in the solvent cyclohexane) are presented in Fig. 4.11. Note the different time scaling of the transient spectra compared to Figs. 4.8 and 4.10. At both hydration levels shown ($w_0 = 2$ and 8), the enhanced absorbance change due to the excited state absorption is broader and decays faster than at comparable values of w_0 in DOPC and AOT reverse micelles. An inspection of Table 4.2 verifies this impression. Vibrational relaxation of the bending mode in Brij-30 reverse micelles at $w_0 = 2$ happens on a 400 fs time scale and is faster than at a value of $w_0 = 8$ in the ionic reverse micelles. Increasing the hydration level up to $w_0 = 8$ further enhances the relaxation rate resulting in a 250 fs lifetime close to the value observed for bulk water.

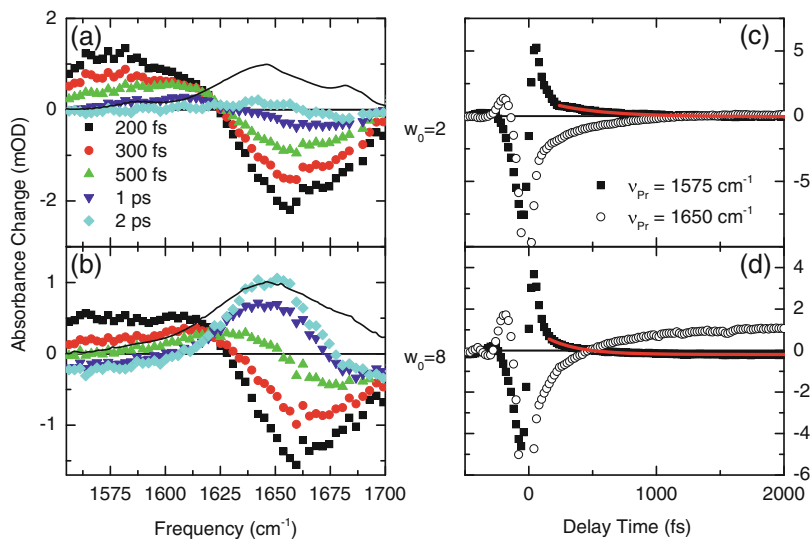


Fig. 4.11 Pump-probe data of the OH bending vibration of water in Brij-30 reverse micelles for $w_0 = 2$ and 8. The corresponding linear spectra are shown as *lines*, a shoulder at $w_0 = 3$ is due to the cyclohexane solvent. Note the different time scaling of the transient spectra compared to the ones of DOPC and AOT (Figs. 4.8 and 4.10) indicating shorter bending lifetimes in the case of Brij-30

The OH bending relaxation of water in the ionic and non-ionic reverse micelles is consistent with the results of bulk water molecular dynamics simulations. As described above, the calculations yield a 270 fs OH bending lifetime with intramolecular energy transfer to the librational modes causing 2/3 and intermolecular energy transfer to water molecules in the first hydration shell accounting for 1/3 of the relaxation rate. The intramolecular relaxation pathway via librations of the bend-excited water molecule remains unaltered in Brij-30 reverse micelles due to the similar librational structure of bulk and confined water. At $w_0 = 2$, a hydration shell around head-group bound water molecules does not exist so that only the intramolecular channel contributes to the relaxation rate of $2/3 \cdot (270 \text{ fs})^{-1}$ corresponding to a 405 fs lifetime. This value is in excellent agreement with the experimental result. The intermolecular decay channel is opened upon raising the H₂O concentration so that water-water hydrogen bonds between nearest neighbors can form. Accordingly, the OH bending lifetime decreases as is evident by the value of 250 fs observed for Brij-30 reverse micelles at $w_0 = 8$.

In the ionic reverse micelles, both inter- and intramolecular energy relaxation are affected when w_0 is decreased. In addition to the removal of closest neighbors, the librational L2 band downshifts by $\Delta\nu_{L2} = 170 \text{ cm}^{-1}$ when going from bulk water to an AOT reverse micelle with $w_0 = 1$. Overtones must therefore be expected to downshift by $\approx 2\Delta\nu_{L2} = 340 \text{ cm}^{-1}$ leading to a strongly reduced probability of establishing a Fermi resonance with the bending fundamental and a concomitant increase of the relaxation rates. In the classical molecular dynamics simulations mentioned above [26], the Fourier spectrum of the rotational kinetic energy time correlation function is used to estimate the relevance of rotations around different molecular axes for bend de-excitation. Only the overtone of the rotation around the axis with the lowest moment of inertia has a substantial Fourier amplitude at the bending fundamental frequency. The corresponding spectrum displaying a $>500 \text{ cm}^{-1}$ width is centered at 1400 cm^{-1} . A downshift of $2\Delta\nu_{L2}$ to $< 1100 \text{ cm}^{-1}$ would diminish the Fourier amplitude at the bending frequency of 1650 cm^{-1} almost completely which makes intramolecular energy transfer to the librations much less efficient. As a result, we see the 800 fs lifetime of the OH bending vibration in DOPC reverse micelles at $w_0 = 1$ that is 5 times longer than the one for bulk H₂O reported in [21]. Similar dynamics in DOPC and AOT reverse micelles suggest similar librational potentials in both cases.

After OH bend relaxation, excess energy deposited in the librations must be redistributed to low-frequency modes in order to reach a thermally equilibrated state. It has been shown that the equilibration occurs on a sub-100 fs time scale for bulk water [25, 28, 29, 59]. Vibrational energy is mainly transferred to librations of the first and second hydration shell in a first step followed by population of other low-frequency modes such as hydrogen-bond vibrations. Consequently, the macroscopic sample temperature rises and the hydrogen-bond structure is modified. This modification is observed by the hot ground state pump-probe signals that are dominated by the enhanced absorption around 1650 cm^{-1} . As explained for OH stretching excitations before, this hot ground state directly reflects vibrational energy redistribution in intracellular water pools.

In conclusion, the use of reverse micelles with variable water content allows for a selective control of the OH bending relaxation pathway. Non-ionic reverse micelles display hydration-independent librational spectra so that the influence of the intermolecular energy transfer to nearest neighbors can be studied by decreasing the size of the first hydration shell of the bend-excited water molecule. In contrast, the redshift of the L2 band for ionic reverse micelles enables the possibility to investigate its influence on the intramolecular bend relaxation via librations. It should be noted that the temperature-dependent bulk-water bending lifetimes were found to increase from 170 to 250 fs upon heating from 195 to 348 K [60]. The concomitant decrease of hydrogen-bond strength leads to a shift of the L2 band from 670 to 635 cm^{-1} [61]. This is clearly smaller than the one found for reverse micelles explaining the only moderate increase of temperature-dependent lifetimes.

We note that, in principle, another relaxation pathway exists in reverse micelles, namely intermolecular energy transfer from water to the surfactant molecules. For DOPC and AOT, the carbonyl stretching as well as the phosphate and sulfonate stretching modes are potential candidates. The energy difference between carbonyl stretching at 1740 cm^{-1} and OH bending vibrations at 1650 cm^{-1} is less than $kT = 200 \text{ cm}^{-1}$ (with k being the Boltzmann constant) at room temperature so that efficient energy transfer might be expected. However, we already found in Sect. 3.3 that the carbonyl-stretching dynamics do not depend on the water content, i.e., coupling between water and carbonyl vibrations is not sufficient for a substantial amount of energy transfer. This argument is further supported by the lack of a hot water ground state around 1650 cm^{-1} after carbonyl stretch excitation (cf. Fig. 3.13).

An important result of this thesis is that water acts as efficient heat sink for phosphate excitations, i.e., there is an energy flow of phosphate stretching excitations to low-frequency hydrogen-bond modes of intramolecular water pools. It should be emphasized that the heat-sink function is facilitated via low-frequency head-group modes so that direct energy flow from the phosphate stretching to water is negligible. The same applies for OH bend excitations of water that might be accepted by phosphate stretching vibrations. Energy acceptance of the phosphate (or sulfonate) groups is highly unlikely due to the large energy mismatch of 400 cm^{-1} . Lifetimes of water bending vibrations longer than 5 ps were found for water monomers in nonpolar solvents that have accepting modes in a similar frequency range like the phosphate vibrations [34].

A final remark about the polarization dependence of the pump-probe measurements discussed above should be made. In all cases, only data acquired with linear parallel pump and probe pulse polarizations were shown. Ultrafast anisotropy decays for the OH stretching mode (Fig. 4.5c) may suggest that the bending lifetimes should be extracted from isotropic pump-probe data. In order to clarify the polarization dependence of the OH bending pump-probe data, time-dependent anisotropies for water in AOT reverse micelles are displayed in Fig. 4.12. At $w_0 = 3$, a fairly constant anisotropy is found up to delay times of 2 ps for both the enhanced and reduced absorption contributions to the signal measured at 1589 and 1645 cm^{-1} (Fig. 4.12a). Anisotropies taken at frequency positions of the positive absorbance change for $w_0 = 8$ are constant up to 75 fs and a slight decay to a value of 0.3 may be observed

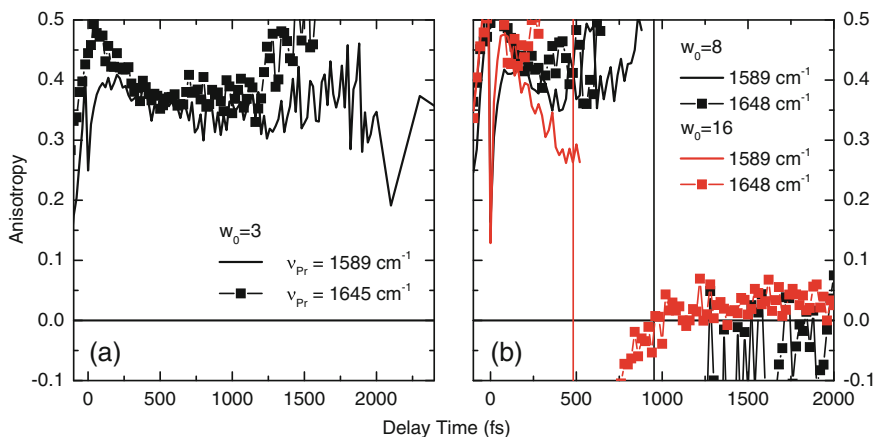


Fig. 4.12 Pump-probe anisotropies of the water bending vibration in AOT reverse micelles for **a** $w_0 = 3$, **b** $w_0 = 8$ and 16. A constant anisotropy for $w_0 = 3$ up to a delay time of 2 ps suggests rigid hydrogen-bond geometries. The anisotropy $w_0 = 8$ and 16 at 1648 cm^{-1} vanishes at long delay times because energy redistribution within the water pool affects all water molecules in a similar way so that any polarization memory gets extinguished

at $w_0 = 16$. The observation times are shorter than in the case of $w_0 = 3$ because of the shorter vibrational lifetimes causing a rapid decay of the isotropic absorbance change which represents the denominator in Eq. 2.62. Note the substantially different anisotropies for $w_0 = 8$ and 16 for the negative absorbance change contribution. Both curves show a rise after 250 and 500 fs, respectively, followed by a change of the sign, eventually levelling off at a value of zero.

In all cases, changes of the anisotropy during the vibrational lifetimes are negligible in agreement with the result of bulk water [21]. Recall that the anisotropy decays found for the OH stretching mode of H_2O are mainly caused by interaction of the two OH stretching modes of one water molecule and resonant energy transfer between OH stretching oscillators of neighboring water molecules. The former contribution cannot exist for the bending mode and the latter is negligible as evident from a back-of-the-envelope calculation: When transition dipole moments are modeled as weakly coupled point dipoles (Förster resonant energy transfer [62]), energy transfer rates depend on the square of the dipole moments. The same dependency applies for linear absorption spectra (cf. Eq. 2.51). As is evident from Fig. 2.2a (p. 18), the amplitude and the spectral width of the OH bending absorption are both about 5 times smaller than the one of the OH stretching absorption suggesting a transition-dipole-moment ratio of 1:25. As a result, bending energy transfer rates are expected to be 25 times slower than the 100 fs constant found for the stretching modes [32]. Therefore, energy transfer is less efficient than vibrational relaxation for the bending mode leading to a negligible anisotropy-decay contribution.

Constant anisotropies for $w_0 = 3$ are a clear sign that large-angle jumps of water orientations do not occur, i.e., the hydrogen-bond geometry between water and the

lipid head groups is preserved on a 1 ps time scale. Zero anisotropies at long times for $w_0 = 8$ and 16 (measured at 1648 cm^{-1}) indicate that there is no correlation between the polarizations of the initially excited molecule and the hot ground state. This result is in agreement with the energy redistribution over all water molecules inside the reverse micelle as discussed several times before.

4.3 Hot Ground States as Local Thermometers, Energy Flow Out of Reverse Micelles

The analysis of energy flow after excitation of phosphate or water vibrations provides strong evidence that water pools accept vibrational excess energy and that the concomitant temperature rise weakens intermolecular water-phosphate and water-water hydrogen bonds. So far we have only considered few-picosecond time scales to observe energy redistribution within the reverse micelles by monitoring hot vibrational ground state signals as hallmarks of increasing temperatures. That is, those signals are effectively used as local thermometers. As such, they should also be able to give insight into the cooling of the micelle's cores on a longer time scale when energy is transferred to the surrounding solvent.

Figure 4.13 summarizes the long-term behavior of different hot ground state signals after OH stretching excitation up to a delay time of 100 ps. Figure 4.13a, b shows the response of the OH stretching vibration at the two different hydration levels $w_0 = 3$ and 16 (corresponding to the traces in Fig. 4.5b, d). The temperature rise of water in both samples directly after energy redistribution to low-frequency hydrogen-bond modes is in the range of 20 K. While most of the signal at $w_0 = 3$ decays within 5 ps, only a partial decay occurs on a 10–20 ps time scale for $w_0 = 16$ leaving a significant absorbance change at 100 ps. This behavior is in agreement with previous investigations of cooling of water droplets inside AOT reverse micelles [63, 64]. There the authors have found that the slower cooling of large reverse micelles ($w_0 > 10$) can be explained by classical heat diffusion across the water pool to the nonpolar solvent whereas faster cooling rates for small reverse micelles ($w_0 = 2$) are due to strong vibrational couplings of the vibrations of water to vibrational modes of the surfactant it is bound to.

It is interesting to compare the hot ground state of the OH stretch to the one of the antisymmetric phosphate stretching vibration (cf. Fig. 4.13b, c). Both traces show similar rise and decay times. While the decay of the phosphate stretching response appears to be slightly slower, an explanation of this result is not straightforward. A careful interpretation would require to model the transient lineshapes, which could, for instance, directly be related to the vibrational temperature. In this way, the phosphate stretching response may be used as an interfacial probe that monitors heat transfer between the water phase and the phospholipid.

We note that the pump energies and the pump-probe overlap are slightly different for the two traces shown in Fig. 4.13b, c. The low frequency of the phosphate

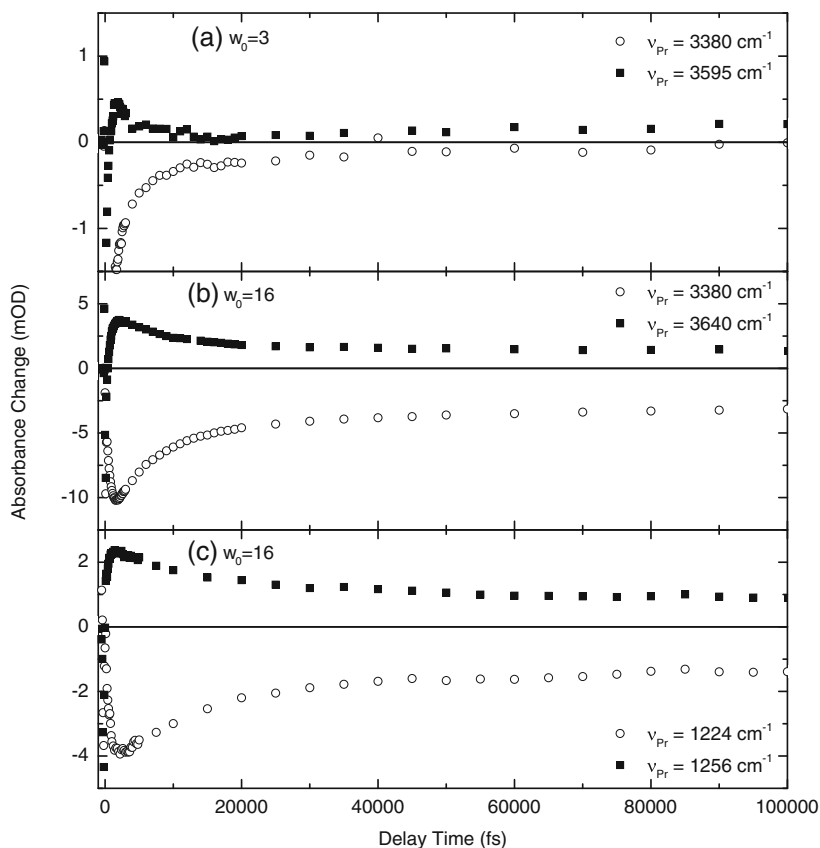


Fig. 4.13 Long-lived hot ground state signals after OH stretching excitation with pump-pulse frequencies around 3400 cm^{-1} . Responses of the OH stretching vibration at **a** $w_0 = 3$ and **b** $w_0 = 16$ as well as the one of the antisymmetric phosphate stretching vibration at **c** $w_0 = 16$

stretching vibration leads to a diffraction-limited probe-beam waist approximately 3 times bigger than by probing the OH stretching response. That is, due to the mismatch of pump- and probe-beam waists, a more inhomogeneous excitation volume is probed by using the antisymmetric phosphate stretching vibration. Accordingly, the results in Fig. 4.13c represent an ensemble average over an inhomogeneous distribution of temperatures. Although a classical heat diffusion model predicts cooling rates that are independent of the initial temperature jump [63], additional measurements, e.g., with tunable pump-pulse energies could help to gain a better understanding of heat dissipation in reverse micelles.

References

1. H. Graener, G. Seifert, A. Laubereau, New spectroscopy of water using tunable picosecond pulses in the infrared. *Phys. Rev. Lett.* **66**, 2092–2095 (1991)
2. R. Laenen, C. Rauscher, A. Laubereau, Dynamics of local substructures in water observed by ultrafast infrared hole burning. *Phys. Rev. Lett.* **80**, 2622–2625 (1998)
3. G.M. Gale, G. Gallot, N. Lascoux, Frequency-dependent vibrational population relaxation time of the OH stretching mode in liquid water. *Chem. Phys. Lett.* **311**, 123–125 (1999)
4. G.M. Gale, G. Gallot, F. Hache, N. Lascoux, S. Bratos, J.-C. Leicknam, Femtosecond dynamics of hydrogen bonds in liquid water: a real time study. *Phys. Rev. Lett.* **82**, 1068–1071 (1999)
5. S. Woutersen, U. Emmerichs, H.J. Bakker, Femtosecond mid-IR pump-probe spectroscopy of liquid water: evidence for a two-component structure. *Science* **278**, 658–660 (1997)
6. S. Woutersen, U. Emmerichs, H.-K. Nienhuys, H.J. Bakker, Anomalous temperature dependence of vibrational lifetimes in water and ice. *Phys. Rev. Lett.* **81**, 1106–1109 (1998)
7. S. Woutersen, H.J. Bakker, Hydrogen bond in liquid water as a Brownian oscillator. *Phys. Rev. Lett.* **83**, 2077–2080 (1999)
8. R. Rey, J.T. Hynes, Vibrational energy relaxation of HOD in liquid D₂O. *J. Chem. Phys.* **104**, 2356–2368 (1996)
9. C.P. Lawrence, J.L. Skinner, Vibrational spectroscopy of HOD in liquid D₂O. I. Vibrational energy relaxation. *J. Chem. Phys.* **117**, 5827–5838 (2002)
10. C.P. Lawrence, J.L. Skinner, Vibrational spectroscopy of HOD in liquid D₂O. VI. Intramolecular and intermolecular vibrational energy flow. *J. Chem. Phys.* **119**, 1623–1633 (2003)
11. R. Rey, K.B. Møller, J.T. Hynes, Ultrafast vibrational population dynamics of water and related systems: a theoretical perspective. *Chem. Rev.* **104**, 1915–1928 (2004)
12. J. Stenger, D. Madsen, P. Hamm, E.T.J. Nibbering, T. Elsaesser, Ultrafast vibrational dephasing of liquid water. *Phys. Rev. Lett.* **87**, 027401 (2001)
13. S. Yermenko, M.S. Pshenichnikov, D.A. Wiersma, Hydrogen-bond dynamics in water explored by heterodyne-detected photon echo. *Chem. Phys. Lett.* **369**, 107–113 (2003)
14. J.J. Loparo, S.T. Roberts, A. Tokmakoff, Multidimensional infrared spectroscopy of water. I. Vibrational dynamics in two-dimensional IR line shapes. *J. Chem. Phys.* **125**, 194521 (2006)
15. J.J. Loparo, S.T. Roberts, A. Tokmakoff, Multidimensional infrared spectroscopy of water. II. Hydrogen bond switching dynamics. *J. Chem. Phys.* **125**, 194522 (2006)
16. C.P. Lawrence, J.L. Skinner, Vibrational spectroscopy of HOD in liquid D₂O. III. Spectral diffusion, and hydrogen-bonding and rotational dynamics. *J. Chem. Phys.* **118**, 264–272 (2003)
17. K.B. Møller, R. Rey, J.T. Hynes, Hydrogen bond dynamics in water and ultrafast infrared spectroscopy: a theoretical study. *J. Phys. Chem. A* **108**, 1275–1289 (2004)
18. C.J. Fecko, J.D. Eaves, J.J. Loparo, A. Tokmakoff, P.L. Geissler, Ultrafast hydrogen-bond dynamics in the infrared spectroscopy of water. *Science* **301**, 1698–1702 (2003)
19. J.B. Asbury, T. Steinell, K. Kwak, S.A. Corcelli, C.P. Lawrence, J.L. Skinner, M.D. Fayer, Dynamics of water probed with vibrational echo correlation spectroscopy. *J. Chem. Phys.* **121**, 12431–12446 (2004)
20. A.J. Lock, H.J. Bakker, Temperature dependence of vibrational relaxation in liquid H₂O. *J. Chem. Phys.* **117**, 1708–1713 (2002)
21. S. Ashihara, N. Huse, A. Espagne, E.T.J. Nibbering, T. Elsaesser, Vibrational couplings and ultrafast relaxation of the O-H bending mode in liquid H₂O. *Chem. Phys. Lett.* **424**, 66–70 (2006)
22. J. Lindner, P. Vöhringer, M.S. Pshenichnikov, D. Cringus, D.A. Wiersma, M. Mostovoy, Vibrational relaxation of pure liquid water. *Chem. Phys. Lett.* **421**, 329–333 (2006)
23. A. Pakoulev, Z. Wang, Y. Pang, D.D. Klott, Vibrational energy relaxation pathways of water. *Chem. Phys. Lett.* **380**, 404–410 (2003)
24. N. Huse, S. Ashihara, E.T.J. Nibbering, T. Elsaesser, Ultrafast vibrational relaxation of O-H bending and librational excitations in liquid H₂O. *Chem. Phys. Lett.* **404**, 389–393 (2005)
25. F. Ingrosso, R. Rey, T. Elsaesser, J.T. Hynes, Ultrafast energy transfer from the intramolecular bending vibration to librations in liquid water. *J. Phys. Chem. A* **113**, 6657–6665 (2009)

26. R. Rey, F. Ingrosso, T. Elsaesser, J.T. Hynes, Pathways for H₂O bend vibrational relaxation in liquid water. *J. Phys. Chem. A* **113**, 8949–8962 (2009)
27. R. Rey, J.T. Hynes, Tracking energy transfer from excited to accepting modes: application to water bend vibrational relaxation. *Phys. Chem. Chem. Phys.* **14**, 6332–6342 (2012)
28. S. Ashihara, N. Huse, A. Espagne, E.T.J. Nibbering, T. Elsaesser, Ultrafast structural dynamics of water induced by dissipation of vibrational energy. *J. Phys. Chem. A* **111**, 743–746 (2007)
29. J. Petersen, K.B. Møller, R. Rey, J.T. Hynes, Ultrafast librational relaxation of H₂O in liquid water. *J. Phys. Chem. B* **117**, 4541–4552 (2013)
30. M.L. Cowan, B.D. Bruner, N. Huse, J.R. Dwyer, B. Chugh, E.T.J. Nibbering, T. Elsaesser, R.J.D. Miller, Ultrafast memory loss and energy redistribution in the hydrogen bond network of liquid H₂O. *Nature* **434**, 199–202 (2005)
31. D. Kraemer, M.L. Cowan, A. Paarmann, N. Huse, E.T.J. Nibbering, T. Elsaesser, R.J.D. Miller, Temperature dependence of the two-dimensional infrared spectrum of liquid H₂O. *Proc. Natl. Acad. Sci. USA* **105**, 437–442 (2008)
32. S. Woutersen, H.J. Bakker, Resonant intermolecular transfer of vibrational energy in liquid water. *Nature* **402**, 507–509 (1999)
33. H. Graener, G. Seifert, Vibrational and orientational relaxation of monomeric water molecules in liquids. *J. Chem. Phys.* **98**, 36–45 (1993)
34. G. Seifert, H. Graener, Solvent dependence of OH bend vibrational relaxation of monomeric water molecules in liquids. *J. Chem. Phys.* **127**, 224505 (2007)
35. A.M. Dokter, S. Woutersen, H.J. Bakker, Anomalous slowing down of the vibrational relaxation of liquid water upon nanoscale confinement. *Phys. Rev. Lett.* **94**, 178301 (2005)
36. D. Cringus, J. Lindner, M.T. Milder, M.S. Pshenichnikov, P. Vöhringer, D.A. Wiersma, Femtosecond water dynamics in reverse-micellar nanodroplets. *Chem. Phys. Lett.* **408**, 162–168 (2005)
37. D. Cringus, A. Bakulin, J. Lindner, P. Vöhringer, M.S. Pshenichnikov, D.A. Wiersma, Ultrafast energy transfer in water-AOT reverse micelles. *J. Phys. Chem. B* **111**, 14193–14207 (2007)
38. I.R. Piletic, D.E. Moilanen, D.B. Spry, N.E. Levinger, M.D. Fayer, Testing the core/shell model of nanoconfined water in reverse micelles using linear and nonlinear IR spectroscopy. *J. Phys. Chem. A* **110**, 4985–4999 (2006)
39. A.A. Bakulin, D. Cringus, M.S. Pshenichnikov, D.A. Wiersma, Frozen dynamics and insulation of water at the lipid interface, in *Ultrafast Phenomena XVI*, ed. by P. Corkum, S. Silvestri, K.A. Nelson, E. Riedle, R.W. Schoenlein (Springer, Berlin, 2009), pp. 514–516
40. E.E. Fenn, D.B. Wong, M.D. Fayer, Water dynamics in small reverse micelles in two solvents: two-dimensional infrared vibrational echoes with two-dimensional background subtraction. *J. Chem. Phys.* **134**, 054512 (2011)
41. E.E. Fenn, D.B. Wong, C.H. Giammanco, M.D. Fayer, Dynamics of water at the interface in reverse micelles: measurements of spectral diffusion with two-dimensional infrared vibrational echoes. *J. Phys. Chem. B* **115**, 11658–11670 (2011)
42. V.V. Volkov, D.J. Palmer, R. Righini, Heterogeneity of water at the phospholipid membrane interface. *J. Phys. Chem. B* **111**, 1377–1383 (2007)
43. V.V. Volkov, D.J. Palmer, R. Righini, Distinct water species confined at the interface of a phospholipid membrane. *Phys. Rev. Lett.* **99**, 078302 (2007)
44. V.V. Volkov, Y. Takaoka, R. Righini, What are the sites water occupies at the interface of a phospholipid membrane? *J. Phys. Chem. B* **113**, 4119–4124 (2009)
45. W. Zhao, D.E. Moilanen, E.E. Fenn, M.D. Fayer, Water at the surfaces of aligned phospholipid multibilayer model membranes probed with ultrafast vibrational spectroscopy. *J. Am. Chem. Soc.* **130**, 13927–13937 (2008)
46. X. Chen, W. Hua, Z. Huang, H.C. Allen, Interfacial water structure associated with phospholipid membranes studied by phase-sensitive vibrational sum frequency generation spectroscopy. *J. Am. Chem. Soc.* **132**, 11336–11342 (2010)
47. J.A. Mondal, S. Nihonyanagi, S. Yamaguchi, T. Tahara, Three distinct water structures at a zwitterionic lipid/water interface revealed by heterodyne-detected vibrational sum frequency generation. *J. Am. Chem. Soc.* **134**, 7842–7850 (2012)

48. Z. Zhang, L. Piatkowski, H.J. Bakker, M. Bonn, Communication: interfacial water structure revealed by ultrafast two-dimensional surface vibrational spectroscopy. *J. Chem. Phys.* **135**, 021101 (2011)
49. M. Yang, Ł. Szyc, T. Elsaesser, Vibrational dynamics of the water shell of DNA studied by femtosecond two-dimensional infrared spectroscopy. *J. Photochem. Photobiol. A* **234**, 49–56 (2012)
50. K.E. Furse, S.A. Corcelli, The dynamics of water at DNA interfaces: computational studies of hoechst 33258 bound to DNA. *J. Am. Chem. Soc.* **130**, 13103–13109 (2008)
51. H. Binder, Water near lipid membranes as seen by infrared spectroscopy. *Eur. Biophys. J.* **36**, 265–279 (2007)
52. D. Cringus, T.I.C. Jansen, M.S. Pshenichnikov, D.A. Wiersma, Ultrafast anisotropy dynamics of water molecules dissolved in acetonitrile. *J. Chem. Phys.* **127**, 084507 (2007)
53. T.I.C. Jansen, D. Cringus, M.S. Pshenichnikov, Dissimilar dynamics of coupled water vibrations. *J. Phys. Chem. A* **113**, 6260–6265 (2009)
54. D.S. Venables, C.A. Schmuttenmaer, Spectroscopy and dynamics of mixtures of water with acetone, acetonitrile, and methanol. *J. Chem. Phys.* **113**, 11222–11236 (2000)
55. D.S. Venables, K. Huang, C.A. Schmuttenmaer, Effect of reverse micelle size on the librational band of confined water and methanol. *J. Phys. Chem. B* **105**, 9132–9138 (2001)
56. C.C. Cooksey, B.J. Greer, E.J. Heilweil, Terahertz spectroscopy of l-proline in reverse aqueous micelles. *Chem. Phys. Lett.* **467**, 424–429 (2009)
57. D.E. Rosenfeld, C.A. Schmuttenmaer, Dynamics of water confined within reverse micelles. *J. Phys. Chem. B* **110**, 14304–14312 (2006)
58. D.E. Rosenfeld, C.A. Schmuttenmaer, Dynamics of the water hydrogen bond network at ionic, nonionic, and hydrophobic interfaces in nanopores and reverse micelles. *J. Phys. Chem. B* **115**, 1021–1031 (2011)
59. T. Yagasaki, S. Saito, Molecular dynamics simulation of nonlinear spectroscopies of intermolecular motions in liquid water. *Acc. Chem. Res.* **42**, 1250–1258 (2009)
60. S. Ashihara, S. Fujioka, K. Shibuya, Temperature dependence of vibrational relaxation of the OH bending excitation in liquid H₂O. *Chem. Phys. Lett.* **502**, 57–62 (2011)
61. H.R. Zelsmann, Temperature dependence of the optical constants for liquid H₂O and D₂O in the far IR region. *J. Mol. Struct.* **350**, 95–114 (1995)
62. T. Förster, Zwischenmolekulare Energiewanderung und Fluoreszenz. *German. Ann. Phys.* **437**, 55–75 (1948)
63. G. Seifert, T. Patzlaff, H. Graener, Size dependent ultrafast cooling of water droplets in microemulsions by picosecond infrared spectroscopy. *Phys. Rev. Lett.* **88**, 147402 (2002)
64. J.C. Deak, Y. Pang, T.D. Sechler, Z. Wang, D.D. Dlott, Vibrational energy transfer across a reverse micelle surfactant layer. *Science* **306**, 473–476 (2004)

Chapter 5

Conclusions

This thesis deals with the femto- to picosecond dynamics of phospholipid-water interfaces as seen by time-resolved vibrational spectroscopy. Phosphate-water interactions are of general importance for the structure and function of biomolecules like DNA and for the formation of lipid cell membranes. Furthermore, the transport of molecules and ions as well as cell communication are influenced by the properties of water in the vicinity of the charged phosphate groups that significantly differ from the ones of the bulk structure. In order to study phosphate-water interactions, phospholipid reverse micelles are employed as model systems. Their structure closely resembles the one of vesicles which are highly relevant for biochemical processes in the cell, allowing for the ultrafast dynamics of confined water in those systems to be deduced.

Ultrafast phosphate-water interactions are investigated in unprecedented detail by an accurate adjustment of the water content inside reverse micelles in a wide range from single water molecules interacting with a phospholipid head group to 16 water molecules per phospholipid. Microscopic information is obtained by using specific vibrational marker modes of phospholipids and its hydration-shell water as local probes that are inherently provided by the system. Phosphate (PO_2^-) vibrations of the two oxygens that form hydrogen bonds with water are direct interfacial probes for fluctuating phosphate-water hydrogen bonds whereas intramolecular OH stretching and bending vibrations of water serve as sensors for the hydration-shell dynamics.

Vibrational lifetimes and energy relaxation pathways are directly measured by single and two-color pump-probe experiments. Molecular dynamics such as fluctuating hydrogen-bond geometries or hydrogen-bond breaking cause vibrational transition frequencies to fluctuate. Two-dimensional (2D) infrared spectroscopy has the power to resolve such frequency fluctuations on ultrafast time scales. With these techniques the following results are obtained for the marker modes mentioned above:

Phosphate stretching vibrations

The lowest frequency for which 2D spectra can be measured with a 100fs time resolution was pushed to below 1000 cm^{-1} making 2D spectroscopy of phosphate vibrations feasible.

- A 2D lineshape analysis of the symmetric and antisymmetric PO_2^- -stretching vibrations reveals that the fastest structural fluctuations of phospholipid head-group orientations occur on a 300 fs time scale. The heterogeneity of hydrogen-bond geometries of the phosphate groups leads to a pronounced inhomogeneity of the phosphate-stretching absorption bands that persists up to 10 ps. This 10 ps time scale therefore sets a lower limit for the phosphate-water hydrogen-bond lifetime. That is, those hydrogen bonds are rigid in relation to water-water hydrogen bonds in neat water that continuously break and reform on a time scale of 1–2 ps.
- 300 fs vibrational lifetimes of the antisymmetric stretching vibration at all hydration levels similar to the values found for such vibrations in DNA point to energy relaxation to low-frequency modes of the phosphate groups. Anharmonic coupling to these modes leads to a transient redshift of the antisymmetric phosphate stretching vibration allowing for monitoring the subsequent energy transfer within the phospholipid and to its environment. Thereby, it is found that water pools around the phospholipids quickly accept excess energy on a sub-picosecond time scale. This process can be regarded as a protection mechanism that efficiently converts high-frequency excitations of phospholipids into heat of the surrounding water phase.
- The temperature increase inside the reverse micelles results in weakened phosphate-water hydrogen bonds which are observed by a transient blueshift of the antisymmetric phosphate stretching vibration. A similar shift is observed after excitation of water OH stretching vibrations whose decay is another mechanism for heating water pools inside reverse micelles.

OH stretching vibration

- Single water molecules bound to the phosphate groups display a static inhomogeneous 2D lineshape consistent with the long phosphate-water hydrogen-bond lifetime.
- A full hydration shell and a pool of H_2O not directly interacting with the phosphate groups are established when the water content is increased to 16 water molecules per phospholipid. In this case, fast frequency fluctuations cause spectral diffusion, i.e., a reshaping of 2D spectra on the time scale of 250 fs which is attributed to structural fluctuations of the water pool.
- In the range of 3–8 water molecules per phospholipid, the 2D spectra show a reshaping toward homogeneous lineshapes on the 400–500 fs time scale of energy relaxation. Energy redistribution to low-frequency modes such as hydrogen-bond vibrations and translations as described below result in an elevated sample temperature. The OH stretching frequency is sensitive to hydrogen-bond strengths and blue-shifts in response to the increased temperature. This response is seen as a so-called hot ground state signal that grows in during energy redistribution to the low-frequency modes. Homogeneous lineshapes indicate that the initial excitation located at a particular water molecule is homogeneously redistributed over an ensemble of water molecules. Consequently, such a redistribution points to small water pools around phospholipids that form as soon as 3 waters per phospholipid are present.

- OH stretching vibrations decay via the OH bending mode which is directly monitored with two-color experiments that show a rising OH bending response on the time scale of the OH stretching decay. This efficient energy relaxation pathway is established by a Fermi resonance of the bending overtone with oscillators in the red part of the OH stretching absorption band. Increased structural fluctuations with increasing water content cause fluctuating OH stretching transition frequencies so that this spectral diffusion accelerates vibrational relaxation by bridging the energy gap between high-frequency OH stretching oscillators and the Fermi resonance. As a result, the OH stretching lifetime decreases from 530 fs for single (static) water molecules per phospholipid to 330 fs when 16 water molecules per phospholipid are present.
- The subsequent equilibration of vibrational excess energy leads to hot ground state signals as described above. Similar signals are observed after excitation of the antisymmetric phosphate stretching vibration when 3 or more water molecules per phospholipid are present which further supports the picture of energy transfer from the phospholipid to its hydration shell.

OH bending vibration

- The decay of the bending vibration proceeds mainly via energy transfer to the librations, i.e., hindered rotations, of the same molecule and partly via intermolecular energy transfer to neighboring water molecules. Single water molecules embedded in the electrostatic potential of phospholipid head groups have a librational spectrum that is 170 cm^{-1} red-shifted compared to bulk water. Consequently, the intra- and intermolecular relaxation rates are significantly lowered compared to the bulk which is reflected in the 4–5 times longer vibrational lifetime of 800 fs.
- As the phospholipid hydration shells are enlarged, their librational spectrum approaches the bulk spectrum. Additionally, an increasing amount of neighboring H_2O molecules opens the intermolecular decay channel. However, interfacial effects are present even for large hydration shells of 16 water molecules per phospholipid that have an OH bending lifetime of 345 fs which is 2 times longer than the bulk value.
- The relaxation times mentioned above depend on the water content inside the reverse micelles due to a simultaneous change of intra- and intermolecular relaxation rates. Using non-ionic reverse micelles made of Brij-30 allows for selectively tuning the intermolecular relaxation rate due to the hydration-independent librational spectrum that resembles the one of bulk water. The short vibrational lifetimes of 400 fs and 250 fs for 2 and 8 water molecules per Brij-30 molecule, respectively, demonstrate the prominent role of librations for energy relaxation of the bending mode.
- With the results described above, the whole energy relaxation pathway of intramolecular vibrations of water in phospholipid reverse micelles is known: OH stretching excitations decay via the OH bending mode followed by vibrational energy redistribution to librations of the same molecule and to other molecules. Librational excitations quickly relax to low-frequency hydrogen-bond vibrations and translations so that the initial excitation of intramolecular water vibrations finally results

in an elevated sample temperature. The elevated temperature is directly observed by characteristic hot ground state signals of phospholipid (antisymmetric phosphate stretching) and water (OH stretching and bending) marker modes.

In summary, time-resolved vibrational spectroscopy of the reverse-micelle system has given valuable insight into the structure and structural dynamics of phospholipid-water interfaces complemented by detailed information about vibrational energy flow. The results presented here can serve as input and benchmark for molecular dynamics simulations, e.g., of processes at the surfaces of cell membranes. The experimental progress made in this thesis allows for investigating ultrafast phosphate-water interactions in a variety of other systems. Studies concerning the hydration of the DNA double-helix backbone are currently in progress.

Appendix A

Experimental Pulse Parameters

Table A.1 summarizes the IR-pulse parameters of the experiments leading to the results presented in Chaps. 3 and 4, i.e., the center frequency ν , bandwidth $\Delta\nu$ (FWHM) and pulse energy E of the pulses k_1 , k_2 and k_3 in 2D IR experiments and of pump and probe pulses in pump-probe experiments. We deduced probe-pulse energies on the order of 10 nJ by assuming that $\approx 2\%$ of the pulse energy are reflected by the BaF₂ wedge. The time resolution T_{res} was estimated from FROG traces generated in CaF₂ or ZnSe windows (2D IR) or cross-correlation traces, e.g., measured by the instantaneous response of semiconductor materials (pump probe).

The sample thickness d depends on the vibrational marker mode used and the water content (for measurements of the ultrafast dynamics of OH stretching or bending vibrations). BaF₂ windows were used for experiments of the phosphate stretching vibration due to their lower dispersion compared to CaF₂ in the frequency range of 1000–1250 cm⁻¹. The thickness of the BaF₂ and CaF₂ windows was 1 mm. For the two-color experiments of Sect. 4.1.1 we used 500 nm thick Si₃N₄ windows in order to suppress nonresonant signals from coherent pump-probe coupling in the sample windows.

Table A.1 Pulse parameters: Central frequency ν , bandwidth $\Delta\nu$ (FWHM), pulse energy E and time resolution T_{res} of the experiment. For the sake of completeness, the sample thickness d and the window material are given as well

Section	Pulse	ν (cm ⁻¹)	$\Delta\nu$ (cm ⁻¹)	E (μ J)	T_{res} (fs)	d (μ m)	Window
3.1	$k_{1,2,3}$	1090–1260	170–200	0.8	<150	25	BaF ₂
3.2	pump	1100/1260	120/180	1.4/2.4	<300/<200	25	BaF ₂
	probe	1130/1260	180/180	$\approx 10^{-2}$			
3.3	pump	1760	160	0.8	≈ 200	25	CaF ₂
	probe	1780	200	$\approx 10^{-2}$			
4.1	$k_{1,2,3}$	3400	340	≈ 0.5	<80	100 ($w_0 = 1$)	CaF ₂
	pump	3400	180	1.8	<150	25 ($w_0 = 5, 8$)	
	probe	3400	350	$\approx 10^{-2}$		6 ($w_0 = 16$)	
	pump	3410	190	2.0	130	200	Si ₃ N ₄
4.2	probe	1690	240	$\approx 10^{-2}$			
	pump	1635	100	2.5	140	200 ($w_0 = 2, 3$)	CaF ₂
	probe	1670	240	$\approx 10^{-2}$		100 ($w_0 = 8$)	
						50 ($w_0 = 16$)	
4.3	pump	3410	200	2	170	25 ($w_0 = 3$)	CaF ₂
	probe	3300	350	$\approx 10^{-2}$		6 ($w_0 = 16$)	
	pump	3420	270	2.5	≈ 250	25 ($w_0 = 16$)	BaF ₂
	probe	1270	160	$\approx 10^{-2}$			

Curriculum Vitae

Dr. Rene Costard
Max-Born-Institut für Nichtlineare Optik und Kurzzeitspektroskopie
Max-Born-Str. 2a
12489 Berlin
email: costard@mbi-berlin.de
Telefon: (+49) 30 6392 1497

Education and scientific career:

- 2014– Postdoctoral researcher at the Max-Born-Institut für Nichtlineare Optik und Kurzzeitspektroskopie (MBI): Ultrafast vibrational dynamics in biomolecules and solids
- 2010–2014 Graduate student at MBI: Ultrafast hydrogen-bond dynamics and energy dissipation in hydrated biomolecular systems using time-resolved vibrational spectroscopy, in particular two-dimensional infrared methods
- 2009–2010 Staff member at MBI: Implementation of a new laboratory for time-resolved mid-infrared spectroscopy
- 2008–2009 Master student at MBI: Shaping and characterization of ultrashort mid-infrared pulses
- 2004–2009 Studies of physics at Humboldt University (Berlin), degree: Diplom-Physiker

Publications

Peer-reviewed articles:

- R. Costard, I. A. Heisler, and T. Elsaesser. “Structural dynamics of hydrated phospholipid surfaces probed by ultrafast 2D spectroscopy of phosphate vibrations”. *J. Phys. Chem. Lett.* 5 (2014), 506–511.
- R. Costard and T. Elsaesser. “Femtosecond OH bending dynamics of water nanopools confined in reverse micelles”. *J. Phys. Chem. B* 117 (2013), 15338–15345.
- R. Costard, C. Greve, I. A. Heisler, and T. Elsaesser. “Ultrafast energy redistribution in local hydration shells of phospholipids: A two-dimensional infrared study”. *J. Phys. Chem. Lett.* 3 (2012), 3646–3651.
- R. Costard, N. E. Levinger, E. T. J. Nibbering, and T. Elsaesser. “Ultrafast vibrational dynamics of water confined in phospholipid reverse micelles”. *J. Phys. Chem. B* 116 (2012), 5752–5759.
- N. E. Levinger, R. Costard, E. T. J. Nibbering, and T. Elsaesser. “Ultrafast energy migration pathways in self-assembled phospholipids interacting with confined water”. *J. Phys. Chem. A* 115 (2011), 11952–11959.
- R. Costard, T. Tyborski, B. P. Fingerhut, and T. Elsaesser. “Ultrafast phosphate hydration dynamics in bulk H₂O”. *J. Chem. Phys.* (accepted).
- R. Costard, C. Greve, H. Fidder, and E. T. J. Nibbering. “Hydrogen bonding induced enhancement of Fermi resonances: Ultrafast vibrational energy flow dynamics in aniline-d₅”. *J. Phys. Chem. B* (in press).
- T. Tyborski, R. Costard, M. Woerner, and T. Elsaesser. “Ultrafast vibrational dynamics of BH₄⁻ ions in liquid and crystalline environments”. *J. Chem. Phys.* 141 (2014), 034506.
- C. Greve, N. K. Preketes, H. Fidder, R. Costard, B. Koeppe, I. A. Heisler, S. Mukamel, F. Temps, E. T. J. Nibbering, and T. Elsaesser. “N-H stretching excitations in adenosine-thymidine base pairs in solution: Pair geometries, infrared line shapes, and ultrafast vibrational dynamics”. *J. Phys. Chem. A* 117 (2013), 594–606.
- C. Greve, N. K. Preketes, R. Costard, B. Koeppe, H. Fidder, E. T. J. Nibbering, F. Temps, S. Mukamel, and T. Elsaesser. “N-H stretching modes of adenosine monomer in solution studied by ultrafast nonlinear infrared spectroscopy and ab initio calculations”. *J. Phys. Chem. A* 116 (2012), 7636–7644.

Conference proceedings:

- R. Costard, C. Greve, N. E. Levinger, E. T. J. Nibbering, and T. Elsaesser. “Ultrafast vibrational dynamics of water confined in phospholipid reverse micelles”. *EPJ Web Conf.* 41 (2013), 06003.
- C. Greve, N. K. Preketes, R. Costard, B. Koeppe, H. Fidder, E. T. J. Nibbering, F. Temps, S. Mukamel, and T. Elsaesser. “Ultrafast IR pump-probe and 2D-IR photon echo spectroscopy of adenosine-thymidine base pairs”. *EPJ Web Conf.* 41 (2013), 05019.

- C. Greve, R. Costard, H. Fidder, and E. T. J. Nibbering. “Hydrogen bond enhancement of Fermi resonances explored with ultrafast IR two-colour pump-probe and 2D-IR spectroscopy”. *Ultrafast Phenomena XIX*. ed. by K. Yamanouchi, S. Cundiff, R. Vivie-Riedle, M. Kuwata-Gonokami, and L. DiMauro. Vol. 162. Springer Proc. Phys. 2015, 471–474.
- R. Costard, I. A. Heisler, and T. Elsaesser. “Hydrated phospholipid surfaces probed by ultrafast 2D spectroscopy of phosphate vibrations”. *Ultrafast Phenomena XIX*. ed. by K. Yamanouchi, S. Cundiff, R. Vivie-Riedle, M. Kuwata-Gonokami, and L. DiMauro. Vol. 162. Springer Proc. Phys. 2015, 301–304.

Berlin, 10.02.2015